Lifetime measurement of the yrast 2^+ state of ^{190}W

Lebensdauermessung des Yrast-2^+-Zustands von ^{190}W
Vom Fachbereich Physik der Technischen Universität Darmstadt zur Erlangung des Grades eines Doktors der Naturwissenschaften (Dr. rer. nat.)
genehmigte Dissertation von Elif Şahin aus İzmir
Tag der Einreichung: 14.06.2023, Tag der Prüfung: 17.07.2023
Darmstadt 2023

1. Gutachter: Prof. Dr. Dr. h.c. mult. Norbert Pietralla
2. Gutachter: Prof. Dr. Thomas Aumann

TECHNISCHE UNIVERSITÄT DARMSTADT

Fachbereich Physik
Institut für Kernphysik
AG Pietralla

Lifetime measurement of the yrast 2^+ state of ^{190}W
Lebensdauermessung des Yrast-2^+-Zustands von ^{190}W

genehmigte Dissertation von Elif Şahin aus İzmir

1. Gutachter: Prof. Dr. Dr. h.c. mult. Norbert Pietralla
2. Gutachter: Prof. Dr. Thomas Aumann

Tag der Einreichung: 14.06.2023
Tag der Prüfung: 17.07.2023

Darmstadt 2023

Institut für Angewandte Physik
Technische Universität Darmstadt

Lifetime measurement of the yrast 2^+ state of ^{190}W

Vom Fachbereich Physik
der Technischen Universität Darmstadt

zur Erlangung des Grades
eines Doktors der Naturwissenschaften (Dr. rer. nat.)

genehmigte Dissertation von
M.Sc. Elif Şahin
aus İzmir

Darmstadt 2023

Abstract

Over the past decades, studies of nuclear structure have led to numerous experiments aimed at understanding the properties of the nucleus. One of the main challenges of this field is the investigation of exotic nuclei, which are characterized by a large excess of neutrons or protons, and are located far from the stability line. To carry out this investigation, experimental techniques capable of producing and detecting these exotic nuclei are required.

At the GSI Helmholtzzentrum für Schwerionenforschung in Germany, the DESPEC setup has been utilized to conduct important nuclear structure studies on exotic nuclei. This setup, in combination with the high-intensity primary beams available at GSI, has provided significant opportunities for the investigation of these exotic nuclei. In March 2021, an experiment was conducted at GSI where isotopes of interest were generated through the fragmentation of a primary ^{208}Pb beam with an energy of 1 GeV/u directed at a ^{9}Be target. The final products were then identified on an event-by-event basis in the FRS based on their proton number (Z) and mass-to-charge ratio (A/Q) and they were implanted in the DESPEC setup..

To further investigate the nuclear structure of these exotic nuclei, measuring the lifetime of excited nuclear states was performed. The measurement was carried out using 36 ultra-fast $LaBr_3$(Ce) detectors from the FATIMA setup. This setup, through a fast-timing technique, enables the hard-to-reach short-lifetime values of those excited states.

This work presents a new isomeric lifetime measurement for ^{190}W. Additionally, we obtained the lifetime of the first 2^+ state of ^{190}W for the first time using the generalized centroid difference method. In view of the systematical behaviour of the $R_{4/2}$, B_{22} and $B(E2)$ values, the known spectroscopic data on ^{190}W matches the predictions for γ-softness. These experimental results have been compared to new theoretical calculations obtained within the interacting boson model (IBM-2). Both experimental and theoretical results agree that the known spectroscopic data on ^{190}W matches the predictions for the most γ-soft, $O(6)$-like isotope in the tungsten isotopic chain, approaching the $N = 126$ shell closure.

Overall, our study provides new insights into the nuclear structure of exotic nuclei and highlights the importance of advanced experimental techniques in this field.

Zusammenfassung

In den letzten Jahrzehnten haben Studien zur Kernstruktur zu zahlreichen Experimenten geführt, die darauf abzielen, die Eigenschaften des Atomkerns zu verstehen. Eine der Hauptaufgaben dieses Bereichs ist die Untersuchung exotischer Kerne, die durch einen großen Überschuss an Neutronen oder Protonen gekennzeichnet sind und weit entfernt von der Stabilitätsgrenze liegen. Um diese Untersuchung durchzuführen, sind experimentelle Techniken erforderlich, die in der Lage sind, diese exotischen Kerne zu erzeugen und nachzuweisen.

Am GSI Helmholtzzentrum für Schwerionenforschung GmbH in Deutschland wurde das DESPEC-Setup genutzt, um wichtige Untersuchungen zur Kernstruktur exotischer Kerne durchzuführen. Dieses Setup bietet in Verbindung mit den hochintensiven Primärstrahlen, die am GSI zur Verfügung stehen, bedeutende Möglichkeiten für die Untersuchung dieser exotischen Kerne. Im März 2021 wurde an der GSI ein Experiment durchgeführt, bei dem interessierende Isotope durch die Fragmentierung eines primären ^{208}Pb-Strahls mit einer Energie von 1 GeV/u auf ein ^{9}Be-Target erzeugt wurden. Die Endprodukte wurden anschließend im FRS auf Ereignisbasis anhand ihrer Protonenzahl (Z) und ihres Massen-zu-Ladungs-Verhältnisses (A/Q) identifiziert und im DESPEC-Setup implantiert.

Um die Kernstruktur dieser exotischen Kerne weiter zu untersuchen, wurde die Messung von Lebensdauern angeregter Kernzustände durchgeführt. Die Messung erfolgte unter Verwendung von 36 ultraschnellen $LaBr_3$(Ce)-Detektoren aus dem FATIMA-Setup. Dieses Setup ermöglicht durch eine schnelle Zeitmessung die Lebensdauerbestimmung von kurzlebigen angeregten Zuständen, die sonst schwer zu erreichen sind.

Diese Arbeit präsentiert eine neue Messung der isomeren Lebensdauer von ^{190}W. Des Weiteren wurde zum ersten Mal die Lebensdauer des ersten 2^+-Zustands von ^{190}W unter Verwendung der generalisierten Methode der Schwerpunkt-Differenzen ermittelt. Angesichts des systematischen Verhaltens der $R_{4/2}$-, B_{22}- und $B(E2)$-Werte stimmen die bekannten spektroskopischen Daten von ^{190}W mit den Vorhersagen für γ-Weichheit überein. Diese experimentellen Ergebnisse wurden mit neuen theoretischen Berechnungen im Rahmen des Interacting Boson Models (IBM-2) verglichen. Sowohl die experimentellen als auch die theoretischen Ergebnisse stimmen darin überein, dass die bekannten spektroskopischen Daten von ^{190}W mit den Vorhersagen für das am stärksten γ-weiche, $O(6)$-ähnliche Isotop in der Wolfram Isotopenkette verträglich sind, bei Annäherung an den Schalenabschluss bei $N = 126$.

Insgesamt liefert unsere Studie neue Einblicke in die Kernstruktur von exotischen Kernen und betont die Bedeutung fortschrittlicher experimenteller Techniken in diesem Bereich.

Acknowledgement

The past five years of my doctoral studies at the GSI have flown by rapidly, and during this time, I have acquired a vast amount of invaluable experience. I have had the fortunate opportunity to engage in numerous experiments and attend several conferences, all of which I shall never forget.

I would firstly like to express my deepest gratitude towards my supervisors Prof. Dr. Dr. h.c. mult. Norbert Pietralla and Dr. Jürgen Gerl for giving me the opportunity to pursue my PhD in their group. Thank you for the guidance and enormous amount of help and support you have given me throughout the whole of my PhD studies.

I am also grateful to Prof. Dr. Thomas Aumann, Prof. Dr. Guy D. Moore, and Prof. Dr. Michael Vogel for agreeing to be on my examination committee, providing great suggestions, and generously sharing their valuable time.

There are many people I would like to thank and acknowledge without whom this work would not have been possible. I especially want to thank Dr. Volker Werner for his valuable support, guidance, discussions, talks, and for patiently addressing my questions. This thesis wouldn't have reached this successful end without his help.

I am immensely grateful to my two best friends who helped me throughout the completion of my thesis. Dr. Andrew Kishor Mistry, thank you for your unbelievable patience, help, and support. Dr. Matthias Rudigier, thank you for your constant support, availability day and night, for answering my questions even in the late evenings, and our regular Friday evening drinks, chats, gossip, and valuable discussions.

A special thanks go to my colleagues in the decay spectroscopy group at GSI and the IKP group at TU-Darmstadt for their incredible support over the past five years. I would also like to thank Ivan Kojouharov and Dr. Plamen Boutachkov for teaching me how to work in the lab, trusting me, guiding me, and helping me become a successful experimental physicist. Additionally, I extend my gratitude to Dr. Stephane Pietri for his assistance with my thesis and for being there for me when needed.

I would also like to thank my friends: Tuğçe İşler, Heidi Ayse Rösch, Arif Soylu, Jacob Lee, Dr. Valerii Panin, Dr. Esra Werner, Katharina Ide, Gülşah Alp, Dr. Tuğba Arıcı, Dr. George Lowani Zimba and my previous supervisor Prof. Dr. Sefa Ertürk. They have provided me with unwavering support and have made these five years enjoyable with their presence.

I would like to express my deepest gratitude to my family: my father, Akın Şahin; my mother, Ceyhan Şahin; my sister and her husband, Çağrı Ndiaye and Bassirou Ndiaye; my aunt, Mediyha Şahin and Dr. Premaditya Chhetri. Without their support and motivation, I wouldn't have made it as far in life. I could not imagine how to finish my dissertation without their love and support.

Canım ailem, her zaman benim yanımda olup beni desteklediğiniz için sizlere çok teşekkur ederim. Sizin desteğiniz ve sevginiz olmasaydı, buralara kadar gelemezdim. Sizi çok ama çok seviyorum. Bu tezimi halam Mediyha Şahine adıyorum.

Contents

List of Figures

List of Tables

1 Introduction

The atomic nucleus is a many-body quantum system where particles interact with each other through three important forces: the electromagnetic force, the strong nuclear force, and the weak nuclear force. Nuclei are made up of protons and neutrons, which are bound together by a strong force. This force is short-range and stronger than gravitation, the weak force, and the Coulomb force. Scientists have been measuring various observables, such as energies and transition strengths of excited nuclear states [1], as well as their electric and magnetic moments. These measurements aim to enhance our understanding of the nuclear structure, which plays a fundamental role in the structure and evolution of the universe. However, many of these nuclei are not found in nature and are difficult to access using conventional methods. Radioactive Ion Beam (RIB) facilities have revolutionized the study of exotic nuclei by allowing scientists to create and study these nuclei using beams of radioactive ions produced through accelerator technology.

Exotic nuclei are nuclei lying away from the line of β-stability, having an extreme neutron number to proton number (N/Z) composition and a relatively short half-life. Such nuclei exhibit unusual phenomena and provide an extreme test of models of nuclear structure. Over the years, numerous theoretical models have been developed to describe different aspects of nuclear structure. These models can be broadly categorized into three main groups: shell models, collective models, and algebraic models like the interacting boson model (IBM). In the past two decades, the establishment of new facilities for studying radioactive ion beams has provided valuable insights into nuclei that are far from the region of β stability.

To this end, the DEcay SPECtroscopy (DESPEC) setup has been developed [2], with the aim to perform measurements of the properties of exotic nuclei. This setup was used at the Gesellschaft für Schwerionenforschung (GSI) to study the decay of neutron-rich tungsten isotopes with a mass of $A \sim 190$. The DESPEC setup was placed in the final focal plane of the FRagment Separator (FRS) to measure the decay of these isotopes (see Chapter 4 for the details). Recent studies have shown that the ground states of neutron-rich nuclei in the A$\sim$190 region indicate shape evolution from a prolate to an oblate deformation [3, 4]. Measuring the energy and lifetime of the first excited 2^+ state in even-even nuclei can provide valuable insights into this shape evolution [5, 6, 7].

One experimentally accessible indicator of nuclear deformation is the ratio of the excitation energy of the first 4_1^+ state to the first 2_1^+ state, known as $R_{4/2} = E(4_1^+)/E(2_1^+)$ [8]. This

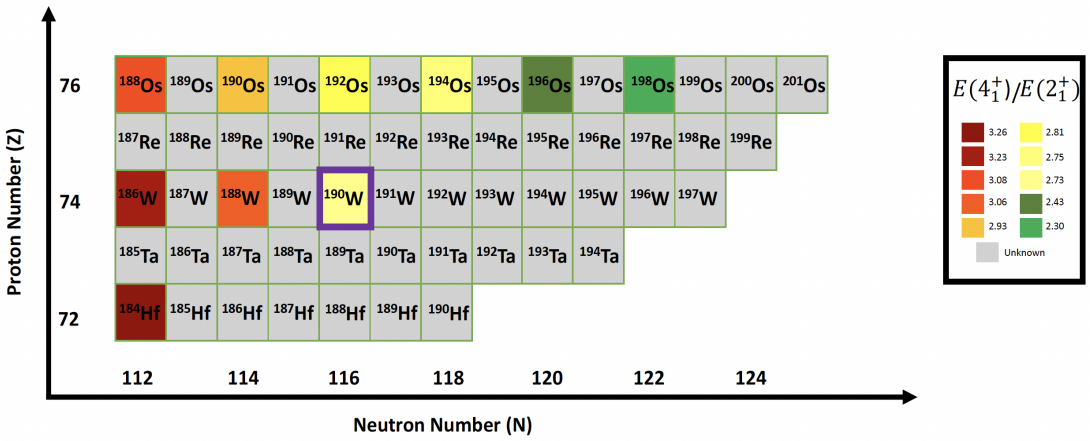

Figure 1.1: The chart of nuclei for the $A \sim 190$ mass region. The purple square represents the current work.

ratio, which is determined by the shape of the nucleus, can differentiate between an axially-symmetric deformed rotor ($R_{4/2} = 3.33$), a spherical vibrational nucleus ($R_{4/2} = 2.0$), and a triaxial rotor ($R_{4/2} = 2.5$) [9]. Figure 1.1 shows a zoomed-in region of interest in the nuclear chart, taking into consideration the $E(4_1^+)/E(2_1^+)$ ratio.

The stable even-even W isotopes with $106 \leq N \leq 112$ are close to the rigid axially deformed limit ($R_{4/2}$=3.33). However, with the addition of more neutrons, the $R_{4/2}$ ratio drops to 2.73 in ^{190}W, indicating γ softness. Figure 1.2 illustrates $E(4_1^+)/E(2_1^+)$ ratio for Hf, W, Os, Pt isotopes for $106 \leq N \leq 122$. It is clear that the experimental ratio of $E(4_1^+)$ and $E(2_1^+)$ in Fig. 1.2 for the lighter isotopes (Hf, W, Os) is close to the rotational limit. The ratio $R_{4/2}$ decreases for heavier even-even isotopes with increasing neutron number. This decrease for tungsten isotopes possibly indicates γ softness, and most likely the beginning of the shape transition towards oblate-deformed ground states [10, 11, 12].

In this study, we focus on the measurement of the half-life of the $I^\pi = 2^+$ state in the neutron-rich isotope $^{190}_{74}W_{116}$. The half-life measurement obtained from the experiment is then used to extract the $B(E2)$ value, which is the transition strength. This $B(E2)$ value is an essential quantity for understanding the nuclear structure and can be compared with theoretical predictions to test the validity of the models.

To perform this experiment, the Generalised Centroid Difference Method (GCD) [28, 29] was employed using the FATIMA[30] $LaBr_3$(Ce) scintillator array which is a high-granularity fast-timing γ-ray detection array. The GCD method is a powerful technique for measuring the half-life of excited states in nuclei within the picosecond range [29].

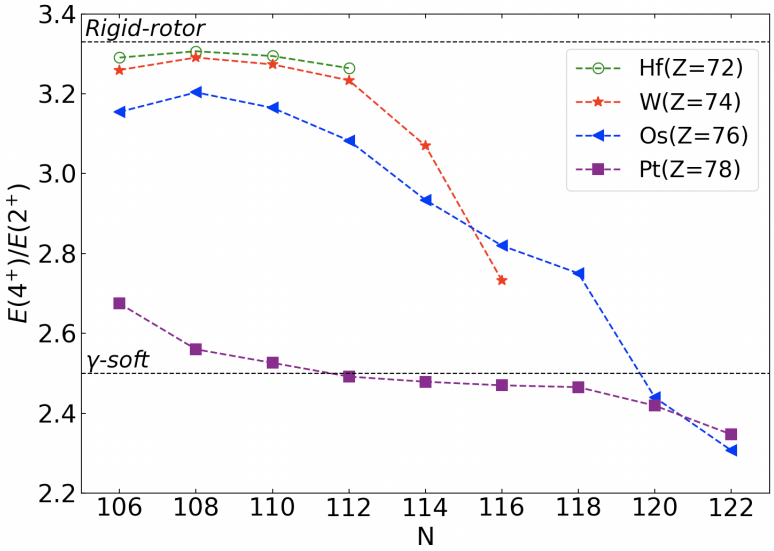

Figure 1.2: The ratio of $E(4_1^+)/E(2_1^+)$ for Hf, W, Os and Pt isotopes, the data was taken from Nuclear Data Sheets and studies Ref [13, 14, 15, 16, 17, 18, 19, 20, 21, 22, 23, 24, 25, 26, 27].

It relies on the direct measurement of the centroid time difference between two signals to determine the lifetime of a nuclear state.

The tungsten isotopes were produced by the fragmentation of a primary beam of heavy ions, and the resulting fragments were separated by the FRS before being detected by the DESPEC setup. The experimental data were then carefully analysed. This result represents an important contribution to our understanding of the nuclear structure of tungsten isotopes. The measured $B(E2)$ value can be compared with theoretical predictions to test the validity of the models, and any discrepancies can be used to refine and improve the models. In addition, the results of this experiment carry implications for astrophysics. Understanding stellar nucleosynthesis and astrophysical phenomena such as Supernovae or X-ray Bursts relies on the exploration and study of exotic nuclei [31].

In conclusion, the use of the DESPEC setup at the GSI, in conjunction with the GCD method and the FATIMA scintillator array, has enabled the precise measurement of the half-life $T_{1/2} = 190(19)$ ps of the $I^\pi = 2^+$ state in the neutron-rich isotope $^{190}_{74}W_{116}$. This result represents an important contribution to our understanding of the nuclear structure and has important implications for astrophysics. The careful and meticulous experimental techniques used in this study ensure that the results are accurate and reliable, and the comparison with theoretical predictions provides an excellent opportunity to refine and improve.

1.1 Outline of the thesis

Following the brief introduction provided in this chapter, this thesis is organized into 8 chapters.

- Chapter 2 presents the theoretical framework required to understand the results.
- Chapter 3 explains the experimental techniques used to extract the lifetimes.
- Chapter 4 provides details on the setups employed, including the development of the data acquisition system.
- Chapter 5 outlines the correction and calibration procedures for the experimental setup.
- Chapter 6 presents the data analysis for the experiment.
- Chapter 7 includes the details of the lifetime measurement in ^{190}W using the GCD method.
- Chapter 8 presents both experimental and theoretical calculations. Particularly $B(E2)$ values in tungsten isotopes are investigated in detail.
- Finally, Chapter 9 summarizes the results and provides an outlook for future spectroscopic investigations on tungsten isotopes.

2 Theoretical background

The atomic nucleus provides a prime setting for examining three of nature's interactions: electromagnetic, strong nuclear, and weak nuclear forces. Numerous phenomena take place in the nucleus, such as the release of particles and radiation, collective excitations, and deformation, among others. Despite the fact that nuclei were discovered over a century ago and numerous experimental and theoretical efforts have been made to fathom their characteristics, there is currently no single, comprehensive nuclear theory in existence, and the underlying interaction between their constituents remains incompletely understood.

The aim of this chapter is to provide a brief overview of the nuclear models used to interpret the experimental results presented in this work. These models are essential for understanding the underlying physics principles and describing the behaviour of atomic nuclei. This chapter only provides a concise summary, and more in-depth information can be found in the references cited at the start of each section or throughout the text. The nuclear shell model and the collective model for vibrations and rotations are presented briefly and the experimental outcomes obtained from this research will be compared to calculations from Interacting Boson Model-2 (IBM-2) [32].

2.1 The shell model

One of the first remarkable theoretical models to describe the nuclei is the shell model, which describes the nuclear shell structure. The shell model provides an explanation for the increased nuclear stability observed at certain proton and neutron numbers, referred to as *magic numbers* [33] and measured to be 2, 8, 20, 28, 50, 82 and 126. The concept behind the nuclear shell model is that a single nucleon experiences a mean-field potential created by the other nucleons. To comprehend the shell model and predict the correct sequence of magic numbers, the initial stage involves selecting an appropriate mean-field potential $V(r)$. The force between nucleons is assumed to be of a 2-body nature for simplicity. The system comprises of A nucleons having masses m_i and momentum $\mathbf{p}_i$, subjected to the nucleon-nucleon interaction which generates a two-body potential $V_{i,j}$ that affects the A-th nucleon is produced by the remaining A-1 nucleons. The Hamiltonian H can be expressed as follows:

$$H = T + V = \sum_{i=1}^{A} \frac{\mathbf{p_i}^2}{2m_i} + \sum_{i>j=1}^{A} V_{ij}(\mathbf{r_i}, \mathbf{r_j}) \tag{2.1}$$

Equation 2.1 is modified by adding and subtracting a central potential $U(r)$, and thus can be separated into a central component and a residual component.

$$H = \underbrace{\left[\sum_{i=1}^{A} T_i(r_i) + U(r_i)\right]}_{\equiv H_0} + \sum_{i>j=1}^{A} V_{ij}(\mathbf{r_i}, \mathbf{r_j}) - \sum_{i=1}^{A} U(r_i) = H_0 + H_{residual}. \tag{2.2}$$

The dominance of the central interaction over residual interactions is reflected in the shell model assumption that $H_{residual}$ is negligible. The Wood-Saxon potential [34] is considered the most realistic potential for describing the interaction between nucleons in a nucleus. It takes into account the contributions of all other nucleons in the nucleus [35, 36]

$$V_{WS}(r) = -\frac{V_0}{1 + \exp(\frac{r-R}{a})}, \tag{2.3}$$

where $R = 1.25\ A^{1/3}$ fm, $a = 0.524$ fm and V_0 is the depth of the potential well, which is around 50 MeV [36]. If the Pauli principle is considered when filling energy levels, these states can be described by three quantum numbers: the principal quantum number n (with values 1, 2, 3, ...), the orbital angular momentum quantum number l (with values 0, 1, ..., n-1), and the spin quantum number $s = 1/2$. This results in the formation of a shell structure, but it only explains the 2, 8, and 20 magic numbers. To account for the remaining observed magic numbers, two additional terms are required. The first is the spin-orbit term, proportional to $\hat{l}.\hat{s}$, where $\hat{l}.\hat{s} = \frac{1}{2}(\hat{j}^2 - \hat{l}^2 - \hat{s}^2)$ and $\hat{j} = \hat{l} + \hat{s}$ and the second is a term proportional to $\hat{l}^2$ (to correct for the overestimation of the energy of levels with large l). Therefore, the magic numbers are reproduced [37, 38] using the following the total potential

$$V(r) = V_{WS}(r) + A\hat{l}^2 + B\hat{l}.\hat{s}. \tag{2.4}$$

The strengths of the spin-orbit and angular momentum self-interaction are denoted by A and B, respectively and they play a crucial role in the rearrangement of energy levels. In particular, these additional terms modify the degeneracy of the energy levels from $2(2l+1)$ to $2j+1$, where j is the total angular momentum obtained from the coupling between the

orbital and spin angular momentum vectors, and can take on values $j = \left|l \pm \frac{1}{2}\right|$. Figure 2.1 illustrates the effect of the spin-orbit interaction by comparing the shell structures obtained using the Woods-Saxon potential with and without the spin-orbit component, as shown on the right and left sides of the figure, respectively. The introduction of the spin-orbit interaction, described by Equation (2.4), leads to a reproduction of the observed magic numbers. In general, a slight deviation in the shell structure between protons and neutrons can be noticed for nuclei with nucleon numbers greater than 82. This difference can be explained by incorporating a Coulomb term in Equation (2.4).

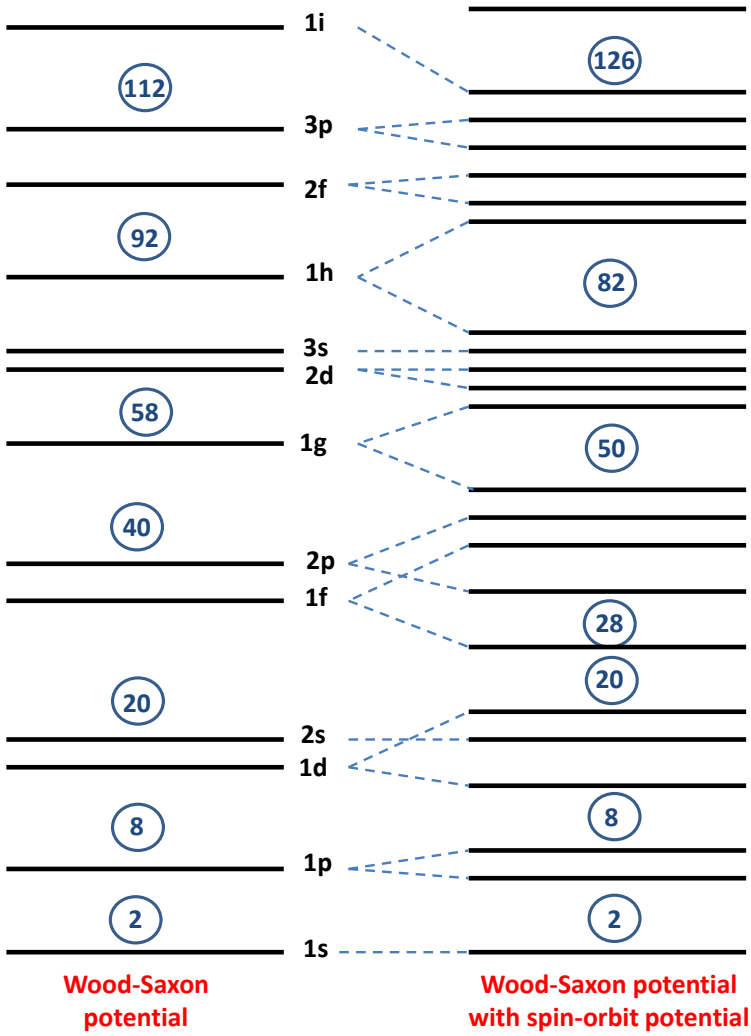

Figure 2.1: The energy levels of the shell model. Left side: Calculated from the Wood-Saxon potential. Right side: Including the spin-orbit coupling. The spin-orbit splitting is most noticeable for the p, d, and f orbitals, which are the ones with the highest angular momentum [35].

Overall, the inclusion of spin-orbit coupling in the shell model provides a more accurate description of the behaviour of atomic nuclei and is an important factor in understanding nuclear structure and stability.

2.2 The Collective Model

The shell model is effective at predicting the properties of nuclei near shell closures. However, it becomes less precise for nuclei far from these closures due to the difficulty in predicting the behaviour of the valence nucleons. Hence the shell model is less effective in describing the nucleus's properties when the number of valence nucleons is sufficiently large. As nuclear deformations become significant, deviations from the spherical shape and axial symmetry need to be taken into account. In order to solve this problem, the Bohr-Mottelson collective model was introduced [39]. This model considers the nucleus as a liquid droplet, resulting in a description of nuclear excitation through fundamental collective modes of surface rotations and vibrations.

A nuclear collective model is a theoretical approach employed to explain the behaviour of atomic nuclei in relation to collective motion. In this model, the nucleons (protons and neutrons) within the nucleus move together in a coordinated manner, rather than acting independently. The model's foundation is built on the understanding that the mean-field potential provides a description of the average interaction experienced by nucleons, shaping the collective behaviour, and determining the energy landscape of the nucleus. The Hamiltonian of the collective model is expressed as:

$$H_{coll} = T_{vib} + T_{rot} + V(\beta, \gamma), \tag{2.5}$$

where T_{vib} represents the vibrational kinetic energy, T_{rot} denotes the rotational kinetic energy, and $V(\beta, \gamma)$ represents the potential energy as a function of β and γ, which correspond to nuclear deformation and angle symmetry, respectively. The corresponding Hamiltonian is given by [8, 39]

$$H = -\frac{\hbar^2}{2D}\left[\frac{1}{\beta^4}\frac{\partial}{\partial\beta}\left[\beta^4\frac{\partial}{\partial\beta} + \frac{1}{\beta^2}\frac{1}{\sin(3\gamma)}\frac{\partial}{\partial\gamma}\left[\sin(3\gamma)\frac{\partial}{\partial\gamma}\right]\right]\right] + \frac{1}{2}\sum_{i=1}^{3}\frac{I_i^2}{\Im_i} + V, \tag{2.6}$$

with the contribution of;

$$T_{vib} = -\frac{\hbar^2}{2D}\left[\frac{1}{\beta^4}\frac{\partial}{\partial\beta}\beta^4\frac{\partial}{\partial\beta} + \frac{1}{\beta^2}\frac{1}{\sin(3\gamma)}\frac{\partial}{\partial\gamma}\sin(3\gamma)\frac{\partial}{\partial\gamma}\right] \tag{2.7}$$

$$T_{rot} = \frac{1}{2}\sum_{i=1}^{3}\frac{\hat{I}_i^2}{\Im_i} \tag{2.8}$$

$$V = V(\beta,\gamma), \tag{2.9}$$

where D is a single mass parameter, $\Im$ is the moment of inertia, i is the coordinates (x, y, z) and $\hat{I}$ is the rotational angular momentum. The deformation parameters β and γ will be discussed in the following sections.

2.2.1 Nuclear Vibrations

Most of the "magic nuclei" are closest to having a spherical shape due to their increased stability. However, as nuclei move away from closed shells, they behave more collectively and exhibit vibrational behaviour due to the small residual interaction of the few valence nucleons. A liquid drop approach to describe deformations and vibrations of the nuclear surface involves an expression using polar coordinates (θ,ϕ) [39] at time t,

$$R(\theta,\phi,t) = R_0\left[1 + \sum_{l=0}\sum_{m=-l}^{l}\alpha(t)_{lm}Y_l^m(\theta,\phi)\right], \tag{2.10}$$

where $R_0 = 1.2A^{1/3}$ fm is the radius of the nucleus and $Y_l^m(\theta,\phi)$ are the spherical harmonic functions of degree l and order m, and α_{lm} gives the amplitude of each vibrational mode, which measure the deformation. The monopole vibration mode $l = 0$ [40, 41], also known as "Breathing Mode", is a type of nuclear vibration that involves the compression and expansion of the entire nucleus, with no deformation of the nuclear surface. In dipole vibration where $l = 1$ [42], the atomic nucleus undergoes an oscillation with a displacement along a specific direction perpendicular to the symmetry axis of the nucleus, where no change occurs within the nucleus. It is purely a translational change and does not affect the energy levels within the nucleus [35]. The first vibration that affects the nucleus is the quadrupole vibration $l = 2$ [43]. The values of lambda that are higher than the fundamental mode ($l = 2$), such as $l = 3$, 4, and so on, correspond to different types of surface vibrations in the atomic nucleus, such as octupole vibrations and hexadecupole vibrations, respectively.

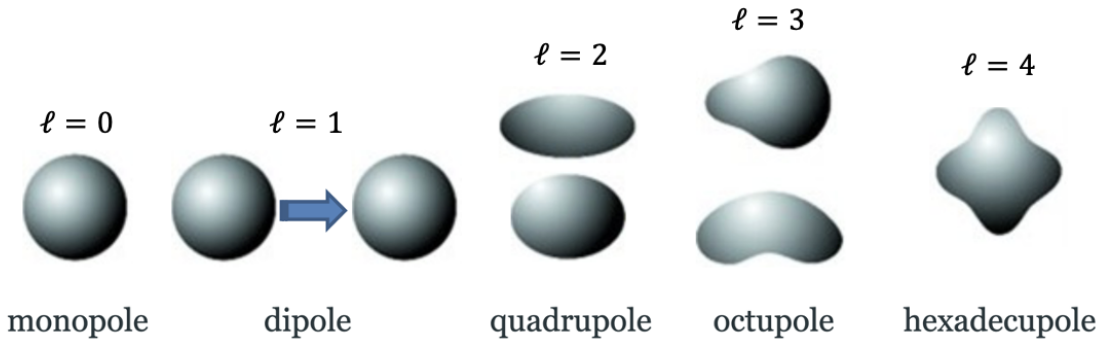

Figure 2.2: Representation of different vibrations, $l = 0$ monopole, $l = 1$ dipole, $l = 2$ quadrupole, $l = 3$ octupole, $l = 4$ hexadecupole oscillations between protons and neutrons.

Phonons are collective excitations of the nuclear system that arise from quantised vibrational modes of the nuclear shape. Similarly to the excitations found in solid-state physics, the excitations of a vibrating nucleus can also be envisioned as phonons with both angular momentum and parity $(-1)^l$. In the case of quadrupole excitations with $l = 2$, these phonons would have a positive parity $J^\pi = 2^+$. The collective Hamiltonian for these oscillations can be expressed in a quantized form as:

$$H_{\text{vib}} = \sum_{lm} \hbar\omega_l \left(b^\dagger_{lm} b_{lm} + \frac{1}{2} \right); \quad \left[\mathbf{b}^\dagger_{lm} \mathbf{b}_{lm} \right] = \mathbb{I} \tag{2.11}$$

where $\mathbb{I}$ is the identity operator, ω is the oscillation frequency, $\mathbf{b}^\dagger_{lm}$ and $\mathbf{b}^\dagger_{lm}$ are vibration creation and annihilation operators, defined as follow;

$$\mathbf{b}_{lm}|n\rangle = \sqrt{n}|n-1\rangle \tag{2.12}$$

$$\mathbf{b}^\dagger_{lm}|n\rangle = \sqrt{n+1}|n+1\rangle \tag{2.13}$$

where $|n\rangle$ is an eigenstate of $\mathbf{b}^\dagger_{lm}\mathbf{b}_{lm}$ belonging to the eigenvalue n. The eigenvalue n of the operator $\hat{N}$ determines the number of vibrational quanta. Therefore the Hamiltonian becomes for the multipole deformations with $l = 2$

$$H_{\text{vib}} = \sum_{m=2}^{-2} \hbar\omega \left(b^\dagger_{2m} b_{2m} + \frac{1}{2} \right); \quad \hat{N} = \sum_{m=2}^{-2} \mathbf{b}^\dagger_{lm} \mathbf{b}_{lm}. \tag{2.14}$$

The given expression represents five harmonic oscillators, all of which have a value of m. The energy levels for different quanta (phonons) of a vibrational mode given by [44]

$$E = \hbar\omega\left(n + \frac{5}{2}\right). \tag{2.15}$$

It is clear from Equation (2.15) that the energy levels are separated by $\hbar\omega$. The allowed spin states for the excited levels depend on the multipolarity of the phonons. For instance, for the quadrupole phonons, the ground state $n = 0$ where there are zero phonons with angular momentum $l = 0$ and its projection $m = 0$, the energy of the ground state is $\frac{5}{2}\hbar\omega$. For the first excited state, $l = 2$ means the one-phonon state is a 2^+ spin is allowed. The energy of the first excited state is $\frac{7}{2}\hbar\omega$. The second excited state means two-phonon state $0^+, 2^+, 4^+$ spins are allowed. The energy of the second excited state is $\frac{9}{2}\hbar\omega$. Therefore, the energy ratio between the two lowest transitions with 2^+ and 4^+ spins is expected to be proportional to the number of phonons and is given by:

$$R_{4/2} = \frac{E(4_1^+)}{E(2_1^+)} = \frac{(9-5)\hbar\omega/2}{(7-5)\hbar\omega/2} = 2. \tag{2.16}$$

Although the model predicts the ratio of $R_{4/2} = 2$, experimental evidence suggests that the ratio is approximately 2.2 [8], indicating that the model is only an approximation.

2.2.2 Nuclear Rotations

Nuclear rotations occur only in non-spherical nuclei, known as deformed nuclei. These nuclei are typically observed in the mass range $150 < A < 190$ and in rare earth and actinide nuclei with masses $A > 220$ [35]. The shape of deformed nuclei can be represented by an ellipsoid of revolution. The most common type of deformation is that of the second multipole order ($l = 2$), specifically the quadrupole deformation. Thus, for $l = 2$, Equation (2.10) becomes:

$$R(\theta,\phi) = R_0\left[1 + \sum_{m=-2}^{2} \alpha_{2m} Y_2^m(\theta,\phi)\right]. \tag{2.17}$$

In principle, there are five expansion coefficients for quadrupole deformations, denoted by α_{2m}, where $-2 < m < 2$. However, due to the constraints that $\alpha_{2-1} = \alpha_{21} = 0$, and $\alpha_{2-2} = \alpha_{22}$, the number of expansion coefficients is reduced to just two: α_{20} and α_{22}. The

Hill-Wheeler polar coordinates β and γ are related to the quadrupole deformation parameters given by [45];

$$a_{20} = \beta \cos\gamma, \tag{2.18}$$

$$a_{22} = \frac{1}{\sqrt{2}}\beta \sin\gamma, \tag{2.19}$$

where β and γ correspond to quadrupole deformation and the degree of axial symmetry, respectively. The shape deformation can be characterised by the intrinsic symmetry axes ($i = 1,2,3$, x, y, z, respectively) of the surface vibration

$$\delta R_i = \sqrt{\frac{5}{4\pi}}\beta R_0 \cos\left(\gamma - \frac{2\pi}{3}i\right) \quad i = 1,2,3. \tag{2.20}$$

In the axially symmetric case, the value of β can be derived from Equation (2.20), which relates the shape and axes of an ellipsoid. Specifically, β corresponds to the difference in length between the major and minor axes of the ellipsoid, with δR representing the change in the ellipsoid's radii due to the deformation.

$$\beta = \frac{4}{3}\sqrt{\frac{\pi}{5}}\frac{\delta R}{R_0}. \tag{2.21}$$

The degree of deformation $\beta = 0$ represents a spherical shape, with no deformation while $\beta \neq 0$ is an ellipsoid. As β increases, the surface becomes more deformed. The deviations from rotational symmetry are described by the parameter γ. The degree of axial asymmetry γ ranges from 0° to 60° to describe the triaxiality. In the case of $\beta > 0$, $\gamma = 0^\circ$ represents an axially symmetric prolate deformation, while $\gamma = 60^\circ$ is an axially symmetric oblate deformation. Moreover, $\gamma = 30^\circ$ reflects the maximum of triaxiality.

The quantized Hamiltonian of a rotating body with a fixed axis, which can be obtained from Equation (2.5) when $T_{vib} = 0$, can be used to represent the rotation. In this case, the Hamiltonian is simplified to a form where the values of $J_3 = 0$, $J_1 = J_2 = J$, resulting in a more straightforward calculation

$$H_{rot} = \frac{\hat{J}^2}{2\Im}; \quad E_{rot}(J) = \frac{\hbar^2}{2\Im}J(J+1), \tag{2.22}$$

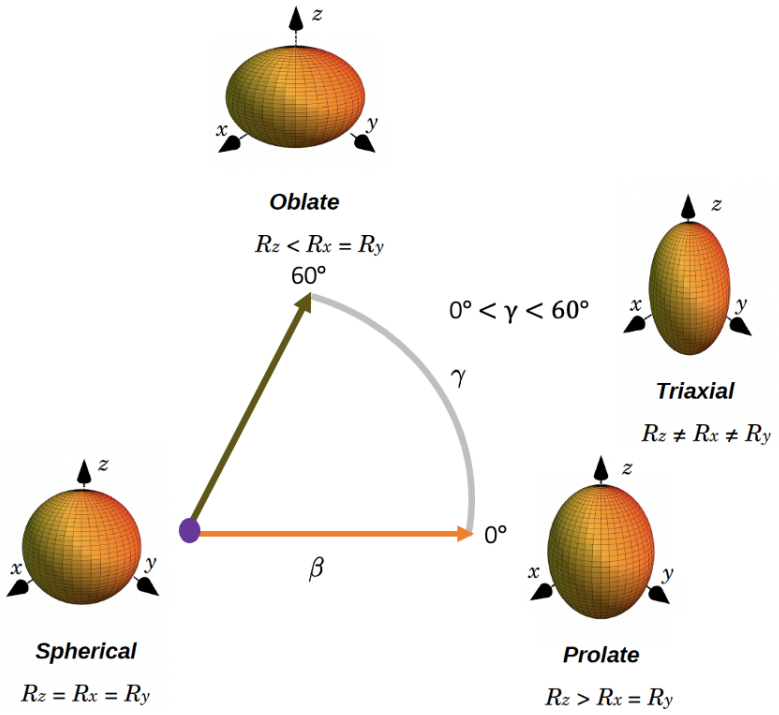

Figure 2.3: Quadrupole deformation ($l = 2$) parameters (β, γ) deformation plane. Representation of three of a nuclear shapes, $\beta = 0$ spherical , for the case of $\beta > 0$ with $\gamma = 0°$ prolate, $\gamma = 60°$ oblate, $0° < \gamma < 60°$ triaxial. $R_{x,y,z}$ represent the radii of the ellipsoid on different axes.

where the moment of inertia of the nucleus is represented by $\Im$, and the rotational angular momentum is represented by J. The nucleus gains additional rotational energy as the quantum number J increases. This results in specific rotational energy values for the rotational levels of an idealized axially symmetric deformed even-even nucleus [8, 35]:

$$\begin{aligned} E(0^+) &= 0 \\ E(2^+) &= 6(\hbar^2/2\Im) \\ E(4^+) &= 20(\hbar^2/2\Im) \\ E(6^+) &= 42(\hbar^2/2\Im) \end{aligned} \tag{2.23}$$

For the constant $\Im$, then the energy ratio between the $E(4_1^+)$ and $E(2_1^+)$ states can be given;

$$R_{4/2} = \frac{E(4_1^+)}{E(2_1^+)} = \frac{4(4+1)}{2(2+1)} = \frac{20}{6} = 3.33. \tag{2.24}$$

The $R_{4/2}$ value is a significant indicator to identify rigid axially symmetric deformed states of even-even nuclei. However, the simplifications made in this approach may not be applicable in several practical scenarios. The deformation of the shape may contain minor non-axially symmetric contributions, resulting in a soft deformation instead of a rigid one, which leads to lower $R_{4/2}$ values.

For an ellipsoid, the moment of inertia can be calculated using the formula $I = 2/5Mr^2$, where M represents the mass and r is a solid sphere of radius rotating around an axis through the center. The radius needs to be integrated over the nuclear surface, and this integration requires the utilization of the first-order deformation parameter β.

$$I = \frac{2}{5}MR_0^2(1+0.31\beta). \tag{2.25}$$

Due to a non-spherical charge distribution within the nucleus, it can be inferred that a deformed nucleus possesses a static quadrupole moment Q which is given by the β deformation parameter. This suggests that the nucleus is not symmetric and the distribution of its charge is distorted. The intrinsic quadrupole moment Q_0 can be only observed in a frame of reference in which the nucleus were at rest [35].

$$Q_0 = \frac{3}{\sqrt{5\pi}}ZR_0^2\beta(1+0.16\beta), \tag{2.26}$$

where $R_0 \propto A^{1/3}$. A positive value for the intrinsic quadrupole moment Q_0 is assigned to a prolate nucleus and a negative value to an oblate nucleus. As the nucleus is rotating, for the experimentally observable spectroscopic quadrupole moment Q is measured differently, which relates to Q_0 by

$$Q = \frac{3K^2 - J(J+1)}{(J+1)(2J+3)}Q_0. \tag{2.27}$$

The spectroscopic quadrupole moment of a nucleus depends on the K-quantum number, which is defined as the projection of the angular momentum J onto the intrinsic symmetry axis of the nucleus ($K \leq J$). In the case of the yrast 2^+ state, which has $K = 0$, the quadrupole moment $Q = -2/7Q_0$. The intrinsic quadrupole moment Q_0 has a relation to the transition strength from the ground state by

$$B(E2;0_1^+ \to 2_1^+) = \frac{5}{16\pi}e^2Q_0(2_1^+)^2. \tag{2.28}$$

In addition to rotational motion, deformed nuclei can also exhibit vibrational excitations. These excitations appear in the level scheme as band heads of rotational bands that correspond to a mixture of vibrational and rotational excitations. Unlike rotational excitations, vibrational excitations do not necessarily have $J = 0$. As a result, equation (2.22) needs to be extended to a more general form.

$$E_{rot} = \frac{\hbar^2}{2\Im}[J(J+1) - K(K+1)]. \tag{2.29}$$

This results in the formation of rotational bands similar to the ground state $(K = 0)$ band. However, for rotational bands based on states where K is not equal to 0, both even and odd angular momenta, such as $J = K, K+1, K+2$, etc., are allowed. This is described in detail in Ref [8]. In the low-lying level schemes of many nuclei, two rotational bands based on a 0^+ and a 2^+ state are frequently observed. The band above the 2^+ state is associated with the vibrational excitation of the nucleus in terms of the deformation parameter γ and is commonly referred to as the γ band. The rotational band above the 0^+ state was initially assigned in a similar manner, i.e., as the vibration in terms of the deformation parameter β, and is commonly referred to as the β band.

2.3 The Wilets-Jean Model

The $\gamma-$soft nuclei, proposed by Wilets and Jean in 1956 [46], describe the collective motion of atomic nuclei and those that have rigid triaxial shapes. According to this model, the potential energy surface of the atomic nucleus has a minimum for non-zero values of the deformation parameter $\beta \neq 0$, but it is free to vibrate in the γ degree of freedom (smoothly $0^\circ < \gamma < 60^\circ$). The level scheme of a $\gamma-$soft nucleus exhibits distinct characteristic features. A schematic representation of the level scheme of such a nucleus is depicted in Figure 2.4(a), where the quantum number Λ is used to label the energy levels. The rotational energies follow is given by $E(\Lambda) \propto \Lambda(\Lambda+3)$, and for states with $J = 2\Lambda$, it can be inferred that

$$E(J) \propto J(J+6). \tag{2.30}$$

As a result, the energies $E(J)$ of the Yrast states in $\gamma-$soft nuclei do not increase with angular momentum J as rapidly as in the case of rotational motion but faster than in the case of vibrational nuclei, as shown in Figure 2.4(b). This implies that the $R_{4/2}$ ratio for gamma-soft nuclei, which is equal to $R_{4/2} = 2.5$, is greater than that of vibrational nuclei. When

$\Lambda = 2$, there exist two degenerate states with angular momentum 2^+ and 4^+ in $\gamma-$soft nuclei. However, unlike in the vibrational case, there is no 0^+ state present.

The $E2$ selection rule observed in the Wilets-Jean model corresponds to the selection rule in the phonon vibration model, where allowed transitions follow the rule of $\Delta\Lambda = \pm 1$. For instance, the transition $2_2^+ \rightarrow 2_1^+$ is allowed ($\Delta = 1$), while the transition $2_2^+ \rightarrow 0_1^+$ is prohibited since the value of Δ is equal to 2.

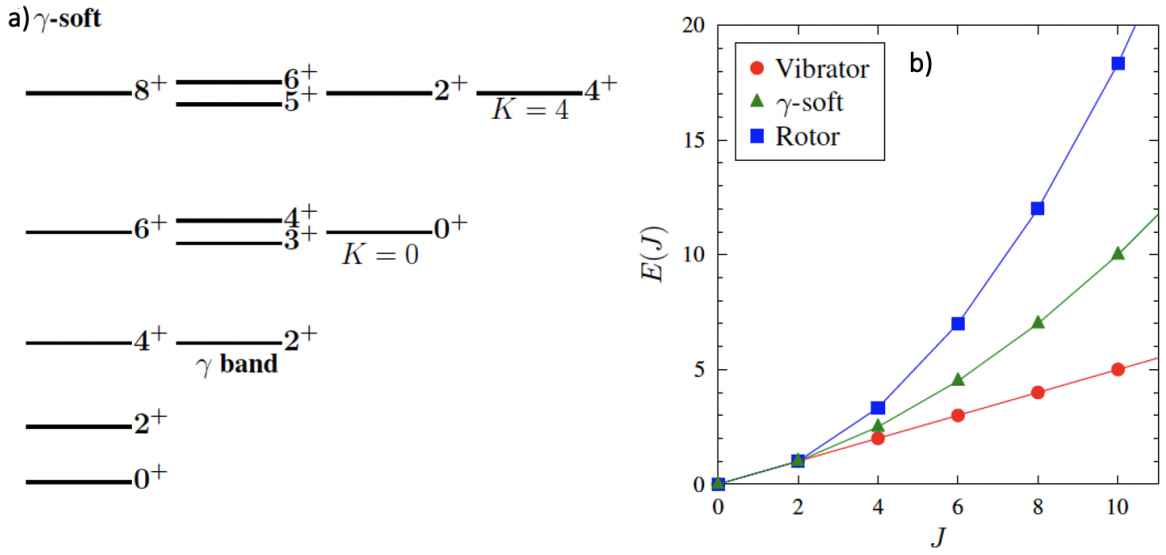

Figure 2.4: (a) a level scheme of a $\gamma-$soft nucleus, (b) the relative energies of the levels in the ground state band of vibrators, rotors, and $\gamma-$soft nuclei. The picture is taken from [47]

2.4 The Interacting Boson Model

The Interacting Boson Model (IBM), also known as the Interacting Boson Approximation (IBA), is a third alternative approach to nuclear structure following the Shell and Collective (geometrical) models. Its development is credited to A. Arima and F. Iachello in 1974 [48, 32], with the aim of explaining the properties of intermediate and heavy atomic nuclei. The IBM model is an algebraic approach used to explain the collective excitation of even-even nuclei. It considers only the valence nucleons are responsible for the properties of the collective low-lying states. The model assumes that protons and neutrons (fermions), are organized in pairs of bosons with an angular momentum of either $L = 0$ (s-bosons) or $L = 2$ (d-bosons). Thus, it describes the excitation of medium and heavy nuclei through the interaction of these bosons. Therefore, the IBM is essentially a shell model that is limited to the neutron and proton valence shells, but without taking into account the Pauli exclusion

principle. The IBM consists of two sub-models, IBM-1 and IBM-2. IBM-1 does not differentiate between protons and neutrons, while IBM-2 treats these two particles separately. In the following sections, IBM-1 and IBM-2 will be discussed separately. Additionally, as a result of IBM symmetry calculations, the extended Casten triangle will be introduced.

2.4.1 IBM-1

Due to the fact that the total number of valence nucleons is a conserved quantity, the total number of bosons in the IBM-1 remains constant. The number of bosons is given by the number of valance protons N_π and neutrons N_ν. Thus, the total number of bosons is $N = (N_\pi + N_\nu)/2$. The bosons can mathematically be treated in terms of creation and annihilation operators for the s and d bosons can be written as $s^\dagger, s$ and $d^\dagger_\mu, \tilde{d}_\mu$ with $\mu \in \{\pm 2, \pm 1, 0\}$, respectively. The operator $\tilde{d}_\mu$ is defined in order to possess the characteristics of a spherical tensor as follows

$$\tilde{d}_\mu = (-1)^\mu d_{-\mu}. \tag{2.31}$$

Additionally, the commutation relations must hold for these operators.

$$\begin{aligned}
\left[s, s^\dagger\right] &= 1, \\
\left[d_\mu, d^\dagger_{\mu'}\right] &= \delta_{\mu\mu'}, \\
\left[s, s\right] = \left[s, s^\dagger\right] &= 0, \\
\left[d_\mu, d_{\mu'}\right] = \left[d^\dagger_\mu, d^\dagger_{\mu'}\right] &= 0, \\
\left[s, d^\dagger_\mu\right] = \left[s, d_\mu\right] = \left[s^\dagger, d^\dagger_\mu\right] = \left[s^\dagger, d_\mu\right] &= 0,
\end{aligned} \tag{2.32}$$

The combination of those operators yields 36 elements. In the context of group theory, these elements generate the Lie Algebra U(6) [48]. The six dimensions originate from the J value, which is 0 for s bosons and 2 for d bosons, resulting in a total of 6 sub-states. Within the subgroups of U(6), there are three analytical solutions of the IBM-1: the anharmonic vibrator U(5) [49], the symmetric rotor SU(3) [50], and the γ-soft rotor O(6) [51]. Each subgroup leads to different dynamical symmetries. The three dynamical symmetries of the IBM, and

Table 2.1: Operators of multipole expansions

Property	Operators
Number of bosons	$\hat{n}_d \equiv d^\dagger \cdot d$
Angular momentum operator	$\hat{L}_\mu \equiv \sqrt{10}\left[d^\dagger \times d\right]^{(1)}_\mu$
Octupole boson operator	$\hat{T}_{3,\mu} \equiv \sqrt{10}\left[d^\dagger \times d\right]^{(3)}_\mu$
Hexadecapole boson operator	$\hat{T}_{4,\mu} \equiv \left[d^\dagger \times d\right]^{(4)}_\mu$
Quadrupole operator	$\hat{Q}^\chi \equiv \left[d^\dagger \times s + s^\dagger \times d\right]^{(2)}_\mu + \chi\left[d^\dagger \times d\right]^{(2)}$
Pairing operator	$\hat{P}_- \equiv (\hat{P}_+)^\dagger, \hat{P}_+ \equiv \left[s^\dagger \times s^\dagger + \sqrt{5} d^\dagger \times d^\dagger\right]^{(0)}_0$

additionally the $\overline{SU(3)}$ symmetry that describes oblate rotors (deformations), are specified by the group chains in Table 2.2. The Hamiltonians for the three subgroups are given by;

$$\begin{aligned} U(5) &: \hat{H} = \varepsilon \hat{n}_d + \kappa' \hat{L} \cdot \hat{L} + c_3 \hat{T}_3 \cdot \hat{T}_3 + c_4 \hat{T}_4 \cdot \hat{T}_4, \\ SU(3) &: \hat{H} = \kappa \hat{Q}^\chi \cdot \hat{Q}^\chi + \kappa' \hat{L} \cdot \hat{L}, \\ O(6) &: \hat{H} = \kappa \hat{L} \cdot \hat{L} + \kappa'' \hat{P}^\dagger \cdot \hat{P} + c_3 \hat{T}_3 \cdot \hat{T}_3, \end{aligned} \tag{2.33}$$

where ε, κ, κ', κ'', χ, c_3 and c_4 are free parameters and $\hat{n}_d$, $\hat{L}$, $\hat{T}_3$, $\hat{T}_4$, $\hat{Q}^\chi$ and $\hat{P}$ are the operators defined in Table 2.1. Another equivalent form of the IBM Hamiltonian is obtained by combining the Hamiltonians of all three subgroups.

$$\hat{H} = \varepsilon \hat{n}_d + \kappa \hat{Q}^\chi \cdot \hat{Q}^\chi + \kappa' \hat{L} \cdot \hat{L} + \kappa'' \hat{P} \cdot \hat{P} + c_3 \hat{T}_3 \cdot \hat{T}_3 + c_4 \hat{T}_4 \cdot \hat{T}_4. \tag{2.34}$$

Table 2.2: The solvable dynamical symmetries corresponding to sub-symmetry of U(6) in the IBM [52]

Symmetry	Symmetry chain	Collective Shape Described	γ
U(5)	U(6)$\supset$ U(5)$\supset$ O(5)$\supset$ SO(3)	Spherical	0°
O(6)	U(6) $\supset$ O(6)$\supset$ O(5)$\supset$ SO(3)	γ-soft rotor	30°
SU(3)	U(6) $\supset$ SU(3)$\supset$ SO(3)	Prolate symmetric rotor	0°
$\overline{SU(3)}$	U(6) $\supset$ $\overline{SU(3)}$ $\supset$ SO(3)	Oblate symmetric rotor	60°

It has been demonstrated in previous studies [54, 55, 56] that for a large boson number N_B, a first-order phase transition occurs between U(5) and SU(3), a second-order phase transition

takes place between U(5) and O(6), while no transition occurs between SU(3) and O(6). The difference between the first-order phase transition X(5) [57] model and the second-order phase transition E(5) [58] model lies in γ dependence used in the Hamiltonian. Specifically, the E(5) model describes the critical point between spherical and γ-soft structures, utilizing a potential that is independent of γ. On the other hand, the X(5) model describes the critical point between spherical and axially symmetric deformed structures, employing a potential of the form $u(\beta)+v(\gamma)$, where $v(\gamma)$ represents a steep harmonic oscillator centered around γ= 0. Of course, when studying nuclei, these theoretical concepts are replaced by observable quantities such as energy ratio for $E(4^+)/E(2^+)$. The collective behaviour of the nucleus with respect to the three symmetry limits (shapes) can be represented by the IBM symmetry triangle known as *Casten's triangle* [53]. This triangular diagram shows how the behaviour of atomic nuclei changes from the spherical limit to the axially-deformed (prolate and oblate) limits. The vertices of the triangle represent the three symmetry limits U(5), SU(3), and O(6). To illustrate such phase-transitional behaviour, distinctive features are associated with each of these symmetries. One such example is the value of $R_{4^+/2^+}$, which equals 2.0 for a harmonic vibrator, 2.5 for a γ-soft rotor, and 3.33 for a deformed axial rotor. This can be achieved using the simple IBA Hamiltonian in the standard notation of the *consistent Q formalism* [59, 60].

$$H = \varepsilon \hat{n}_d - \kappa \hat{Q}^{\chi} \cdot \hat{Q}^{\chi}, \tag{2.35}$$

$$H = c\left[(1-\zeta)\hat{n}_d - \frac{\zeta}{4N_B}\hat{Q}^{\chi} \cdot \hat{Q}^{\chi}\right], \tag{2.36}$$

$$\hat{T}(E2) = e_b \hat{Q}^{\chi}, \tag{2.37}$$

where

$$\hat{Q}^{\chi} = d^{\dagger}s + s^{\dagger}\tilde{d} + \chi\left[d^{\dagger}\tilde{d}\right]^{(2)} \quad and \quad \zeta = \frac{4N_B}{(4N_B + \varepsilon/\kappa)}, \tag{2.38}$$

where c is a normalization constant, e_b is the effective boson chaarge, $\varepsilon = c(1-\zeta)$ and $\kappa = -\frac{c\zeta}{4N_B}$. $\hat{T}(E2)$ represents the operator for the electric quadrupole transition.

In IBM, competition arises between the spherical mean field, characterized by low-lying vibrational excitations, and the quadrupole forces that may induce a deformed mean field (known as intrinsic structure). This competition is quantified in the IBM by the ratio κ/ε, which is replaced by the bounded parameter vary between $\zeta = 0$ spherical and $\zeta = 1$ (where

$\zeta \in [0,1]$) in equation (2.36). Additionally, the degree of γ-softness is controlled by a second parameter, χ (where $\chi \in [-\frac{\sqrt{7}}{2}, 0]$) determines the degree of γ-sofness, which appears in the quadrupole operator. These parameters give rise to three distinct dynamical symmetries in the *Casten's triangle*. As can be seen in Figure 2.5, ζ and χ for U(5) are $\zeta = 0$, for SU(3) are $\zeta = 1$ and $\chi = -\frac{\sqrt{7}}{2}$, and for O(6) are $\zeta = 1$ and $\chi = 0$.

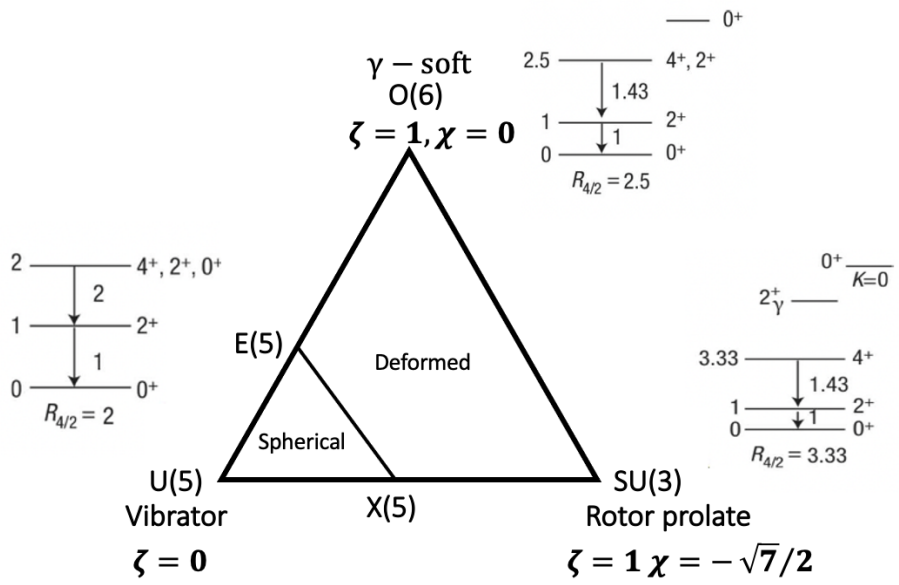

Figure 2.5: The Casten triangle represents the IBM symmetry triangle, which highlights its corners. It can be mapped using ζ (0 for spherical or 1 deformed) and χ. Two critical points, X(5) [57] and E(5) [58], are identified and used to describe the transition of nuclei during the shape-phase. Both points have analytical solutions for the Bohr Hamiltonian and are associated with a subgroup of IBM models. Specifically, E(5) describes the transition from a vibrator to γ-soft rotor, while X(5) represents the transition from a vibrator to a rotor during the shape-phase.

2.4.2 IBM-2

IBM-1 is unable to describe the $J^{\pi}_{K} = 1^{+}_{1}$ state that carries the total $M1$ strength, known as the scissors mode in deformed nuclei [61, 62]. Therefore, to obtain a more realistic description of nuclei, an extended version of IBM-1 was introduced as the *Interacting Boson Model-2* (IBM-2) [63, 64], which distinguishes between protons (π) and neutrons (ν) and considers the proton-neutron interaction. IBM-2 has the capability to describe the excitations of proton-neutron mixed-symmetry, which are referred to as *Mixed-Symmetry States* (MSS). A notable advancement in the model is the introduction of distinct creation and annihilation

operators for proton and neutron bosons. This leads to an extended Hamiltonian that provides a more comprehensive understanding of the behaviour of proton-neutron systems. The extended Hamiltonian for IBM-2 is given by[65]:

$$\hat{H} = \hat{H}_\pi + \hat{H}_\nu + \hat{H}_{\pi\nu}, \tag{2.39}$$

$$H = \varepsilon_\pi \hat{n}_{d_\pi} + \varepsilon_\nu \hat{n}_{d_\nu} + \kappa_{\pi\pi} Q_\pi^{\chi\pi} \cdot Q_\pi^{\chi\pi} + 2\kappa_{\pi\nu} Q_\pi^{\chi\pi} \cdot Q_\nu^{\chi\nu} + \kappa_{\nu\nu} Q_\nu^{\chi\nu} \cdot Q_\nu^{\chi\nu} + \hat{M}(\xi_1, \xi_2, \xi_3), \tag{2.40}$$

where ε_π and ε_ν are single d boson energies, $Q_\pi^{\chi\pi}$ and $Q_\nu^{\chi\nu}$ are the quadruopole operators defined in Equation (2.38). $\hat{M}$ is the *Majorana operator* [66], a neutron-proton symmetry interaction to push up these non-symmetric states.

To differentiate between proton and neutron bosons, the concept of F-spin quantum number is introduced [64]. This quantum number indicates the degree of symmetry between neutrons and protons. Similar to the isospin quantum number, the F-spin has a value of $F = 1/2$, with F_z defined as $+1/2$ for protons and $-1/2$ for neutrons [67].

Boson type	b_π	b_ν
F	1/2	1/2
F_z	+1/2	-1/2

The IBM-1 and IBM-2 models yield almost identical results for collective states in the low-energy region where neutron-proton symmetry is assumed. This means that the states with $F = F_{max}$ in the IBM-2 correspond to states in the IBM-1 on a one-to-one basis. The total projection F_z and the maximum F-spin are given by

$$F_z = \frac{1}{2}(N_\pi - N_\nu), \tag{2.41}$$

$$F_{max} = \frac{1}{2}(N_\pi + N_\nu), \tag{2.42}$$

Fully-symmetric states (FSS) correspond to specific states that arise in the IBM-1. On the other hand, states that exhibit $F < F_{max}$ are called MMS. The wave function of MSS is only partially antisymmetric when proton and neutron boson labels are exchanged. Currently, only MSS with $F = F_{max} - 1$ have been discovered, such as the 1^+ scissors mode [61] and the lowest lying MSS is the one quadrupole phonon MSS labelled as $2^+_{1,ms}$ observed in vibrational nuclei [65].

The third term which is proton-neutron interaction contribution in Equation (2.39) is given using multipoles

$$\hat{H}_{\pi\nu} = \sum_{\lambda} \kappa_{\lambda} \hat{T}_{\lambda,\pi} \hat{T}_{\lambda,\nu}, \tag{2.43}$$

where λ is the multipole order. The operator T(E2) provided by IBM-2 is used to calculate the transition probability in the IBM-2 approximation.

$$\hat{T}(E2) = e_{\pi}\hat{Q}_{\pi}^{\chi} + e_{\nu}\hat{Q}_{\nu}^{\chi}. \tag{2.44}$$

The coupling between FSSs and FSSs or MSSs and MSSs is facilitated by the effective quadrupole boson charges, e_{π} and e_{ν}, but it is prohibited for transitions between MSSs and FSSs. Although the transition is not completely prohibited, it is typically suppressed in practice. To account for 3^{-} states, the sd-IBM-2 model requires expansion by incorporating octupole f bosons. As a result, the improved model is named the sdf-IBM-2 [68].

2.4.3 The Extended Casten Triangle

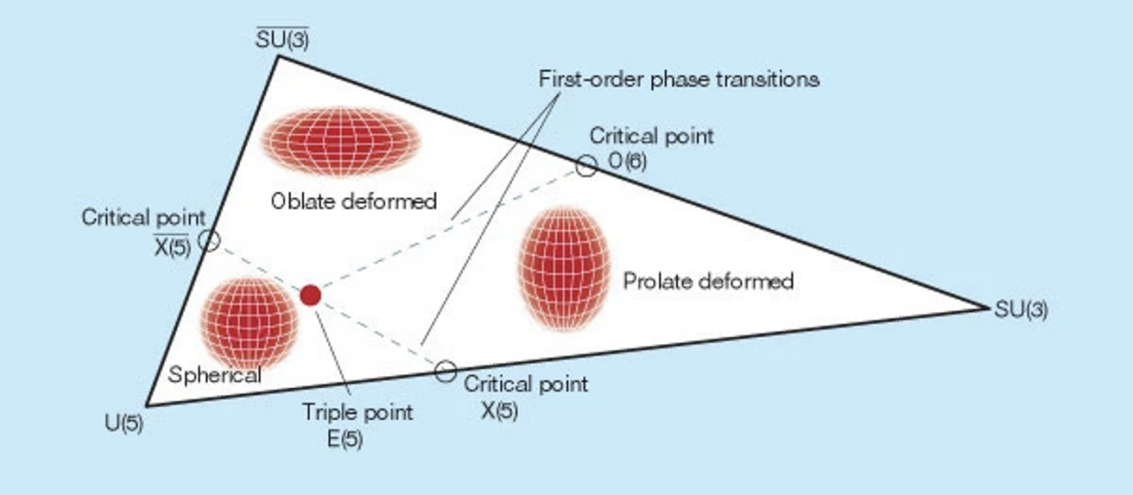

Figure 2.6: The extended Casten triangle. The picture is taken from Ref [69]

In the previous section, it was mentioned that the Interacting Boson Model (IBM) has three distinct limiting cases that correspond to different nuclear shapes: spherical [vibrational, U(5)], axially deformed [SU(3)], and γ-soft [O(6)]. These shapes are often represented by the Casten triangle. However, the picture was not complete. Therefore, the extended Casten

triangle provides the new nuclear phase diagram [69, 70]. For instance, the phase transition from spherical to axially deformed shape is denoted as the U(5)-SU(3) transition, while the U(5)-O(6) transition describes from spherical to γ-unstable motion phase transition. The SU(3)-O(6)-$\overline{SU(3)}$ transition [70, 71, 72], on the other hand, describes the phase transition from a prolate to an oblate shape. It is noteworthy that the prolate phase and the oblate phase are represented by the SU(3) and the $\overline{SU(3)}$ symmetry, respectively. The O(6) limit is attained precisely at the critical point. It should be noted that the dynamical structures in the two limiting cases are similar, except for the sign change in the quadrupole operator (χ=-$\frac{\sqrt{7}}{2}$ and χ=$\frac{\sqrt{7}}{2}$ for SU(3) and $\overline{SU(3)}$, respectively). This is because the $\overline{SU(3)}$ generators can be derived from the corresponding SU(3) generators by introducing a phase change in the s-boson operators in the IBM [73, 74].

2.5 Fundamentals of γ-ray spectroscopy

Gamma-ray spectroscopy studies provide extensive information on nuclear structure. When nuclei are in the excited state, they decay, and during their de-excitation, γ rays are emitted. The energy difference between the initial and final states of the γ-ray emission is referred to as γ-decay.

As discussed earlier, the energy ratio $R_{4_1^+/2_1^+}$ can indicate whether a nucleus behaves collectively as rotational, vibrational, or γ-soft. Measuring the lifetime of excited levels can provide more detailed information on these behaviours. The lifetime of an excited state is linked to its transition probability and associated matrix element, allowing for precise comparisons between experimental measurements and theoretical models.

This section will introduce the basic concepts of selection rules of electromagnetic transitions, transition probabilities, and their typical units.

2.5.1 Selection rules

Assuming that a nucleus decaying from an initial state with energy E_i, angular momentum I_i, and parity π_i to a final state with energy E_f, angular momentum I_f, and parity π_f via the emission of a γ-ray with energy (Figure 2.7)

$$E_\gamma = E_i - E_f. \tag{2.45}$$

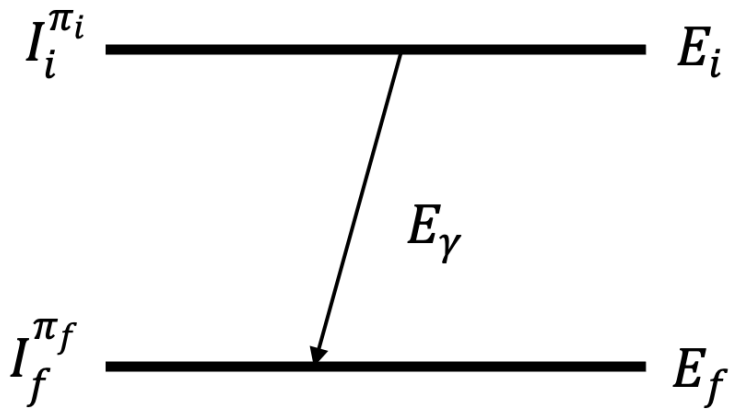

Figure 2.7: Example of level scheme for initial and final states and the γ-ray transition connecting these two states

The conservation of energy, spin, and momentum leads to the establishment of selection rules governing the values of energy (E), angular momentum (L), and parity (π) for electromagnetic (EM) transitions.

$$|I_i - I_f| \leq L \leq I_i + I_f \quad and \quad L > 0. \tag{2.46}$$

As a result, the emitted radiations possess only positive angular momentum values of $L > 0$ (such as 1, 2, 3, and so on). The monopole term, where $L = 0$, is not permitted since γ rays have a spin of $1\hbar$ implies that a 0^+ to 0^+ transition (i.e., $L = 0$) cannot occur with γ emission. The higher angular momentum values, such as L = 1 (dipole term), L = 2 (quadrupole term), and so on, could occur. The type of emitted radiation, whether it is electric (E) or magnetic (M) in nature, is determined by parity.

$$\pi_\gamma = \pi_i \cdot \pi_f = \begin{cases} (-1)^L & \text{for electric character,} \\ (-1)^{(L+1)} & \text{for magnetic character.} \end{cases} \tag{2.47}$$

Table 2.3 displays the lower multipole orders along with their corresponding parity selection rule.

Radiation Type	Name	L	$\Delta\pi_{if}$
E1	Electric Dipolar	1	$\pi_i = -\pi_f$
M1	Magnetic Dipolar	1	$\pi_i = +\pi_f$
E2	Electric Quadrupolar	2	$\pi_i = +\pi_f$
M2	Magnetic Quadrupolar	2	$\pi_i = -\pi_f$
E3	Electric Octupolar	3	$\pi_i = -\pi_f$
M3	Magnetic Octupolar	3	$\pi_i = +\pi_f$

Table 2.3: The even parity radiation field consists of M1, E2 and M3, while the odd parity radiation field includes E1, M2 and E3.

2.5.2 Transition probabilities

The total decay rate of the transition from an initial state to a final state can be expressed as [39]

$$T(\sigma L)_{i\to f} = \frac{8\pi(L+1)}{L[(2L+1)!!]^2}\frac{1}{\hbar}\left(\frac{E_\gamma}{\hbar c}\right)^{2L+1} B(\sigma L; I_i \to I_f), \quad (s^{-1}) \tag{2.48}$$

The reduced transition strength denoted as $B(\sigma L)$, is used to express the electric and magnetic transition probabilities. Specifically, the electric transition probability can be expressed using the electric operator $\hat{Q}$, while the magnetic transition probability can be expressed using the magnetic operator $\hat{M}$.

$$B(EL; I_i \to I_f) = \frac{1}{2I_i+1}|\langle f||\hat{Q}||i\rangle|^2, \tag{2.49}$$

$$B(ML; I_i \to I_f) = \frac{1}{2I_i+1}|\langle f||\hat{M}||i\rangle|^2. \tag{2.50}$$

The units for the transition strengths $B(\sigma L)$ used to express the electric and magnetic transition probabilities are

$$[B(EL)] = e^2 fm^{2L}, \quad [B(ML)] = \mu_N^2 fm^{2L-2}, \tag{2.51}$$

In the literature, the unit commonly used to express the electric transition matrix elements is the *barn* (b), instead of *femtometer* (fm^2). The conversion between b and fm^2 is $1b = 100fm^2$. The units for magnetic transition matrix elements are $\mu_N^2 fm^{2L-2}$, where μ_N is the

nuclear magneton equal to 0.105 efm and is derived from $\mu_N = e\hbar/2m_pc$. The direction of the transition, such as $B(\sigma L)$, is dependent on its orientation.

$$B(\sigma L\downarrow) = \frac{2L_f+1}{2L_i+1}B(\sigma L\uparrow) \tag{2.52}$$

The "↓" symbolizes the transition from the initial state to the final state (from a higher to a lower spin) ($i \to f$) , while "↑" symbolizes the transition from the final state to the initial state ($f \to i$) (from a lower to a higher spin). Therefore, for the electric quadrupole transition $B(E2; 2_1^+ \to 0_{gs}^+)$, the relation becomes:

$$B(E2\downarrow) = \frac{1}{5}B(E2\uparrow) \tag{2.53}$$

Table 2.4 provides the transition rates for lower multipole orders, where E_γ is expressed in units of MeV.

σL	$\mathrm{T}(\sigma L)_{i\to f}\ (s^{-1})$	σL	$\mathrm{T}(\sigma L)_{i\to f}\ (s^{-1})$
E1	$1.59\times10^{15}E_\gamma^3\mathrm{B(E1)}$	M1	$1.76\times10^{13}E_\gamma^3\mathrm{B(M1)}$
E2	$1.22\times10^{9}E_\gamma^5\mathrm{B(E2)}$	M2	$1.35\times10^{7}E_\gamma^5\mathrm{B(M2)}$
E3	$5.67\times10^{2}E_\gamma^7\mathrm{B(E3)}$	M3	$6.28\times10^{1}E_\gamma^7\mathrm{B(M3)}$
E4	$1.69\times10^{-4}E_\gamma^9\mathrm{B(E4)}$	M4	$1.87\times10^{-6}E_\gamma^9\mathrm{B(M4)}$

Table 2.4: Transition rates for some low multipole orders [39]

The transition probability per unit time T_{if} is inversely proportional to the lifetime τ of the transition. Comparing experimental observations with model predictions can be best achieved by examining the lifetime of an excited state, which serves as an ideal observable.

$$T_{if} = \frac{1}{\tau}. \tag{2.54}$$

2.5.3 Weisskopf estimates

When a single particle causes a transition by moving from one spherical shell-model state to another, the transition probability can be estimated using the *Weisskopf estimate* or single

particle estimate. These probabilities can be calculated analytically with a nuclear radius of $R_o = 1.23A^{1/3}$ fm.

$$B_W(EL;I_i \rightarrow I_f) = \frac{(1.2)^{2L}}{4\pi}\left(\frac{3}{L+3}\right)^2 A^{\frac{2L}{3}} \quad e^2 fm^{2L} \tag{2.55}$$

$$B_W(ML;I_i \rightarrow I_f) = \frac{10\times(1.2)^{2L-2}}{\pi}\left(\frac{3}{L+3}\right)^2 A^{\frac{2L-2}{3}} \quad \mu_N^2 fm^{2L-2}. \tag{2.56}$$

These equations depend on the atomic mass A and the multipolarity of the transition. Therefore, it is practical to provide Table 2.5 which includes the single-particle Weisskopf estimates for the transition rates $T_{sp}(\sigma L)$ and the reduced transition probability $B_W(\sigma L)$ for different multipolarities.

σL	$B_W(\sigma L)$	$T_{sp}\sigma L$ (1/s)
E1	$6.45\times10^{-2}A^{2/3}$	$1.02\times10^{14}A^{2/3}E_\gamma^3$
E2	$5.94\times10^{-2}A^{4/3}$	$7.23\times10^{7}A^{4/3}E_\gamma^5$
E3	$5.94\times10^{-2}A^{2}$	$3.37\times10^{1}A^{2}E_\gamma^7$
E4	$6.29\times10^{-2}A^{8/3}$	$1.06\times10^{-5}A^{8/3}E_\gamma^9$
M1	1.79	$3.12\times10^{13}E_\gamma^3$
M2	$1.65\times A^{2/3}$	$2.21\times10^{7}A^{2/3}E_\gamma^5$
M3	$1.65\times A^{4/3}$	$1.03\times10^{1}A^{4/3}E_\gamma^7$
M4	$1.75\times A^{2}$	$3.25\times10^{-6}A^{2}E_\gamma^9$

Table 2.5: Single-particle Weisskopf transition probability estimates $T_{sp}(\sigma L)$ and reduced transition probability $B_W(\sigma L)$ as a function of the atomic mass A and γ-ray energy E_γ [39]. The units of $B_W(EL)$ is e^2fm^{2L}, $B_W(ML)$ is $\mu_N^2 fm^{2L-2}$, $T_{sp}\sigma L$ is sec^-1 and E_γ is MeV.

2.5.4 Internal Conversion

Internal conversion is a process when an excited atomic nucleus transfers its energy to one of its own atomic electrons instead of emitting a gamma ray. This energy transfer results in the ejection of the electron from the atom, which causes the emission of a characteristic X-ray or Auger electron. The kinetic energy of the ejected electron, denoted as E_e, is determined by the difference between the transition energy (E_γ) and the binding energy of the electron ($E_{B\ell}$) which differs for each atomic-shell.

$$E_e = E_\gamma - E_{B\ell}, \tag{2.57}$$

where ℓ is the atomic shell (ℓ=K, L, M etc.). The total decay probability λ_t is given by

$$\lambda_t = \lambda_\gamma + \lambda_e. \tag{2.58}$$

The internal conversion coefficient (IC or α) can be characterised by the ratio of rate of internal conversion decay to rate of $\gamma-$ray decay.

$$\alpha = \frac{\lambda_e}{\lambda_\gamma}. \tag{2.59}$$

The total decay probability using the total internal conversion coefficient α becomes

$$\lambda_t = \lambda_\gamma(1+\alpha). \tag{2.60}$$

By definition, the total internal conversion coefficient α is the summation of all the individual coefficients of every atomic shell.

$$\alpha = \alpha_K + \alpha_L + \alpha_M + ... \tag{2.61}$$

It is possible to calculate the internal conversion coefficient for electric (E) and magnetic (M) multipole transitions in a non-relativistic calculation using the following method [35]:

$$\alpha(EL) \cong \frac{Z^3}{n^3}\left(\frac{L}{L+1}\right)\left(\frac{e^2}{4\pi\varepsilon_0\hbar c}\right)^4\left(\frac{2m_ec^2}{E_\gamma}\right)^{L+\frac{5}{2}}, \tag{2.62}$$

$$\alpha(ML) \cong \frac{Z^3}{n^3}\left(\frac{e^2}{4\pi\varepsilon_0\hbar c}\right)^4\left(\frac{2m_ec^2}{E_\gamma}\right)^{L+\frac{3}{2}}. \tag{2.63}$$

The determination of the multipolarities of a nuclear transition can be achieved by comparing the total or relative conversion coefficients measured with the calculated ones. The conversion coefficients depend on the atomic number of the atom (Z), the principal quantum number of the ejected electron (n), the electron mass (m_e), the multipolarity of the transition (L), the transition energy (E_γ), and the fine structure constant $([e^2 4\pi\varepsilon_0\hbar c] \approx 1/137)$. At high multipole orders or low transition energies, internal conversion competes strongly with γ-ray

emission, and its contribution to the conversion coefficients is proportional to Z^3, becoming important for heavier nuclei.

2.5.5 Nuclear level lifetime

As shown in Equation (2.54), the transition probability T_{if} has an inverse proportional relation to the lifetime τ of a radioactive nucleus from a higher excited state or ground state to a lower excited state.

$$\tau = \frac{1}{T_{total}} = \frac{1}{T_{if}(1+\alpha)} = \frac{t_{1/2}}{ln2}. \tag{2.64}$$

The half-life of a radioactive nucleus, denoted as $t_{1/2}$, is a representation of its decay constant and is defined as the time required for the activity to decrease to half of its initial value.

If an excited state can decay to multiple final states through different decay paths, then the total transition probability is the sum of all the individual transition probabilities. The transition probability of the i^{th}decay path is denoted by $T(i)$, and the total transition probability can be expressed as the sum of all the $T(i)$ values. Moreover, the actual half-life of the given excited state will be the sum of all partial half-life.

$$T_{total} = \sum_i T(i), \tag{2.65}$$

$$t_{1/2} = \sum_i t_{1/2}(i), \tag{2.66}$$

$$t_{1/2}(i) = \frac{ln2}{T(i)}. \tag{2.67}$$

Therefore, the half-life can be calculated with the transition probability and the internal conversion coefficient as a unit of second

$$T_{if} = \frac{ln2}{t_{1/2}(1+\alpha)}. \tag{2.68}$$

The experimentally measured half-life, $t_{1/2}$, of a state provides a value for the transition probability T_{if}. Using Equation (2.48) for the transition probability of a single particle provides information on the reduced transition probability, $B_w(\sigma L)$, as given in Equation (2.55).

3 Experimental Techniques

It is essential to choose the appropriate experimental method when measuring nuclear-level lifetimes as different techniques are suitable for different ranges of lifetimes. Nuclear level lifetimes can vary greatly, from femtoseconds for short-lived levels to years for long-lived isomeric states, and transition energies can range from a few eV to several MeV.
This section will provide an overview of the various techniques used to determine the lifetimes of excited states in nuclei produced in fragmentation of a ^{208}Pb primary beam, with lifetimes ranging from few picoseconds to nanoseconds. The main features of experimental electronic fast-timing and its associated analysis methods, such as the slope method, the deconvolution method, and the recently developed Generalized Centroid Difference Method, which extended to a setup of N detectors, will be introduced. The following will provide a brief introduction to the analysis of time spectra, with the primary aim of introducing key concepts and definitions.

3.1 Techniques for the electronic fast timing

Electronic fast timing is an experimental technique used in nuclear physics to measure the lifetimes of excited states in nuclei. It involves the detection of the decay products of these states, typically gamma rays or electrons, and measuring the time of arrival of these particles with high precision. This information can then be used to determine the lifetime of the excited state. Electronic fast timing can be performed using various techniques such as the slope method, the deconvolution method, and the Generalized Centroid Difference Method. A summary of these methods, their applicable range, the precision of timing, and measuring methods are provided in Figure 3.1.

The basic principle behind electronic fast timing in nuclear physics is the direct measurement of the time difference between two signals (start and stop) to determine the lifetime of a nuclear state. The first signal marks the moment of a population of the state of interest, while the second signal marks its decay. Any measurable event that can accurately determine the population and decay can be used. For lifetime measurements of nuclear excited states, the time reference for a population is usually provided by direct reaction or decay products such as scattered particles, implanted ions, or radiation. As a reference for the decay of a

nuclear excited state, radiation from directly depopulating transitions is used. This technique is also known as the delayed coincidence method, which refers to the requirement for a clear correlation between the two signals to be assigned to the same de-excitation process (see Figure 3.2). This is also the reason why the upper limit of measurable lifetimes is typically on the order of 10^{-6} seconds. To determine lifetimes in the milliseconds and above, the time-dependent activity of a nucleus in a certain state can be measured instead of the time difference between population and decay of this excited state via delayed coincidence measurements. Both methods measure the change of $N(t)$ which is the number of excited states at a time t, governed by the radioactive decay law, but they are applicable to different lifetime regimes.

<table>
<tr><th colspan="2">Methods</th><th>Timing region (sec)</th><th>Timing accuracies</th><th>Procedure of measurement</th><th>Condition on level lifetime</th></tr>
<tr><td rowspan="3">Electronic fast timing techniques</td><td>Slope method</td><td rowspan="2">$10^{-10} < \tau < 10^{-6}$</td><td rowspan="3">~ 1%</td><td rowspan="3">Directly measured from time distribution spectrum</td><td>Lifetime larger than Full Width at Half Maximum (FWHM) of Prompt Response Function (PRF) by at least 30%</td></tr>
<tr><td>Deconvolution method</td><td>Lifetime larger than FWHM of PRF</td></tr>
<tr><td>Centroid shift method</td><td>$10^{-12} < \tau < 10^{-9}$</td><td>Lifetime comparable or below the FWHM of PRF</td></tr>
</table>

Figure 3.1: Techniques for the electronic fast timing and their applicability and precision

In the fast-timing technique, the time resolution of the experimental setup is an important factor. The time resolution can be measured using prompt events or by measuring a lifetime that is short compared to the time resolution of the setup [75]. For the fast timing detector setups, such as $LaBr_3(Ce)$ detectors, the two γ-rays connecting a nuclear state with a lifetime of $\tau \leq 1$ ps can be considered as prompt events [76]. The time difference distribution between these two gamma detection events is known as the Prompt Response Function (PRF), which describes the timing characteristics of the setup. The shape of the PRF is a

Gaussian distribution, where its Full Width at Half Maximum (FWHM) contains all timing uncertainties derived from the scintillator and photomultiplier, electronics, and setup geometry [76]. If the time response of the two detectors is similar, then the obtained PRF will be a symmetric Gaussian Distribution. However, if the time responses of the two detectors are not similar, then an asymmetric Gaussian Distribution will be observed. The Full Width of Maximum (FWHM) of the time distribution peak of the PRF provides an estimate of the Time Resolution of the setup. The time distribution $D(t)$ provided by the TAC can be expressed mathematically as equation (3.1), which represents the convolution of a prompt time distribution $P(t')$ and an exponential decay $e^{-\lambda(t-t')}$.

$$D(t) = \lambda N_0 \int_{-\infty}^{t} P(t') e^{-\lambda(t-t')} dt', \quad \lambda = \frac{1}{\tau}, \tag{3.1}$$

where t' is the centroid of the $P(t')$, N_0 is the total number of detected γ-γ events and λ is the inverse of the mean lifetime τ.

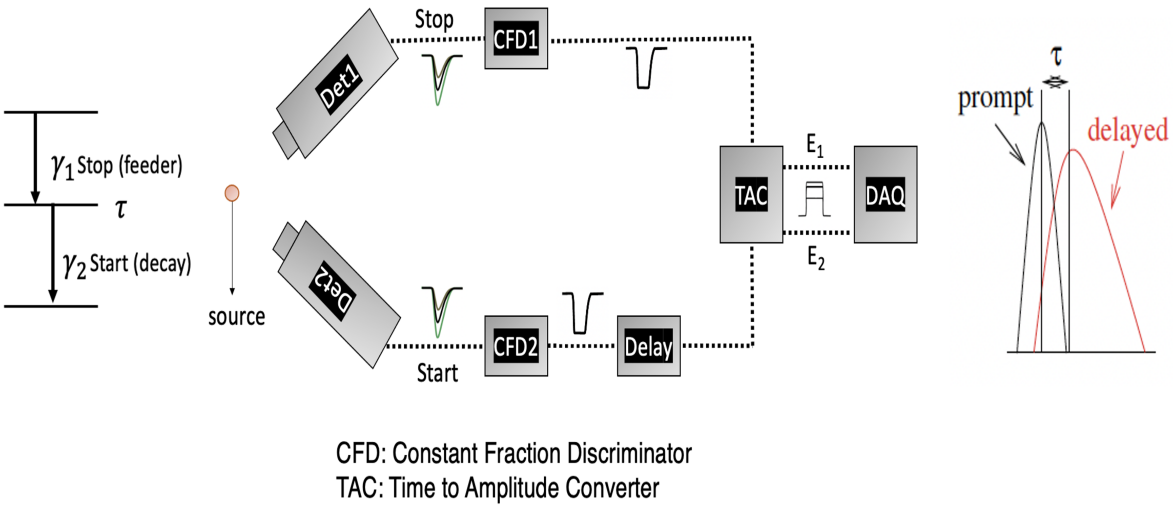

Figure 3.2: A simple fast timing setup for two detectors to illustrate delayed time distribution with prompt response function to measure τ.

3.1.1 Slope Method

The slope method [75] is a straightforward technique used to determine the lifetime of a state in a nuclear decay process by fitting the delayed slope of the time difference distribution to an exponential function $e^{-\lambda t}$. The selected portion of the fitting is crucial and must be chosen carefully as it can affect the accuracy of the results. The method is more accurate for longer lifetime states, as the delayed slope is larger and less sensitive to the prompt contribution. The method is only applicable when the lifetime of the state is longer than the Full Width at Half Maximum (FWHM) of the Prompt Response Fraction (PRF), which is a measure of the time resolution of the experimental setup. The slope method is relatively simple and straightforward to implement, but it requires a relatively reasonable number of counts to obtain accurate results and is sensitive to background noise. The delayed time distribution $D(t)$ is given by;

$$\ln[D(t)] \sim -\lambda t, \tag{3.2}$$

where λ is the decay constant ($\lambda = 1/\tau$).

3.1.2 Convolution Method

The convolution method is an indirect measurement technique used in nuclear lifetime analysis to determine the lifetime of a nucleus. It is based on the convolution of the decay curve of the nucleus with a known function. This method is particularly useful when the lifetime of the radiation is comparable to the time resolution of the system, but not much longer. The convolution fit method differs from the fit slope method in that it fits the entire time distribution, not just the slope. This allows for a more thorough reconstruction of the mean lifetime, which is based on the deconvolution of the prompt response function and exponential decay part as described in equation (3.1) [77, 78, 79]. When the prompt response function is assumed to be approximately Gaussian in shape, the convolution is described by equation (3.3).

$$D(t) = \frac{N_0}{2\lambda} e^{\frac{\sigma^2}{2\tau^2} - \frac{(t-t_0)}{\tau}} erfc\left(\frac{\sigma}{\sqrt{2}\tau} - \frac{(t-t_0)}{\sqrt{2}\sigma}\right), \tag{3.3}$$

where t_0 is the position of the PRF, σ and $erfc()$ are the standard deviation and the Gauss complementary error function respectively. This method provides more accurate results compared to the slope fit method, as reported in several studies [77, 78, 79]. However, it requires

the fitting of 4 parameters, which increases the risk of misinterpretation. If the calculated prompt curve does not accurately reflect the resolution of the experimental setup, due to the presence of background noise or unwanted coincident events, the resulting lifetime calculated using this method could be overestimated, as described by the equation (3.3)

3.1.3 The Centroid Shift Method

Z. Bay proposed the use of coincidence techniques for measuring decay times in 1950 [28]. This technique disregards the prompt curve and focuses on the two transitions time delay curve obtained from coincidence measurements. The Centroid Shift method [77, 80] is employed when the level's decay time is shorter than the FWHM time resolution of the quasi-Gaussian component of the prompt time distribution. This situation occurs when there is no or little visible slope in the delayed part of the spectrum, which is approximately one-third the width of the peak, given as the FWHM. However, the method is limited by the statistics available in the time spectrum. The centroid of time distribution $C(D(t))$ for lifetime determination given by the following equation;

$$C(D(t)) = \frac{\int tD(t)\,dt}{\int D(t)\,dt}. \tag{3.4}$$

The lifetime of interest is determined by the relative shift in the measured centroid of the delayed time spectrum $C(D)$ compared to the prompt response of the same energy $C(P)$. The prompt curve, which describes the system response as a function of energy, provides the relationship, as described in Equation 3.5

$$\tau = C(D) - C(P), \tag{3.5}$$

The generalization of this method which is called the Generalised Centroid Difference Method (GCD) makes lifetime measurements with multiple timing detectors more accurate and efficient [29, 81, 82]. The details of the generalized centroid difference method will be discussed in the following section.

3.1.4 The Generalised Centroid Shift Method

The $\gamma-\gamma$ timing correlation approach measures the duration of a specific state in a nuclear decay by measuring the time between two gamma rays: one to populate the state and another to de-populate it. By analysing these time differences, the lifetime of the state is determined.

We first examine the conventional $\gamma-\gamma$ fast-timing setup that includes two detectors, labelled as start and stop, as depicted in Figure 3.2. When both start and stop detectors are exposed to the same γ-ray source, two-time distributions are generated. This is accomplished by setting a narrow energy window around the full energy peak of the γ decay transition, which results from a specific $\gamma_{feeder}-\gamma_{decay}$ cascade. One time distribution is obtained by using the start detector (delayed), while the other is obtained using the stop detector (anti-delayed). The feeding γ-ray is detected by the opposite detector. Therefore, the lifetime of the state of interest can be measured from the centroid shift between delayed $C_d(D)$ and the corresponding prompt time distributions [28] $C_d(P)$ using

$$\tau = C_d(D) - C_d(P), \tag{3.6}$$

and for the anti-delayed $C_a(D)$ and the corresponding prompt distribution $C_a(P)$ cases:

$$\tau = C_a(P) - C_a(D). \tag{3.7}$$

If no background interference is present, the difference between the centroids of the delayed and anti-delayed ΔC time spectra, as calculated from Equations (3.6) and (3.7), corresponds to:

$$\begin{aligned} \Delta C &= C_d(D) - C_a(D), \\ &= C_d(P) + \tau - \big(C_a(P) - \tau\big), \\ &= PRD(E_f, E_d) + 2\tau, \end{aligned} \tag{3.8}$$

where the Prompt Response Difference, $PRD(E_{feeder}, E_{decay}) = PRD(E_{feeder}) - PRD(E_{decay})$, and τ represents the lifetime to be measured. The PRD function describes the time-walk behavior of the two-timing branches in the detector setup. As a result, the centroid shift difference between the delayed and anti-delayed time distributions is shifted by $+2\tau$ from the corresponding PRD curve. Hence, lifetime τ is given by the equation (3.9):

$$\tau = \frac{1}{2}(\Delta C - PRD(E_{feeder}, E_{decay})). \tag{3.9}$$

To obtain a walk-free reference timing signal, an energy-dependent PRD curve is fit to γ-ray coincidence data from a known radioactive source. The experimental setup must use reference timing signals to calculate the prompt curve in the $\gamma-\gamma$ fast-timing experiment.

The setup is calibrated using a radioactive source, in this case ^{152}Eu, which provides a variety of transition combinations in the picosecond regime. The PRD data points obtained from two decaying branches of ^{152}Eu were fitted using the equation (3.10) as described by Ref. [83]. Further details on time-walk correction are covered in Chapter 5.

$$PRD(E_\gamma) = \frac{a}{\sqrt{E_\gamma + b}} + cE_\gamma + d, \tag{3.10}$$

where a, b, c, and d are free fit parameters obtained from a chi-squared minimisation fit.

4 Experimental Setup

The investigation of exotic nuclei is one of the key goals of the GSI facility in Darmstadt, Germany. *The DEcay SPECtroscopy* (DESPEC) [2] experiment *"The Prolate-Oblate Shape Transition around A∼190"*, labelled with experiment number 'S452' was performed at GSI, with 8 days of beam time in the period 6^{th}-14^{th} of March 2021. Isotopes of interest were produced by the fragmentation of a ^{208}Pb primary beam at an energy of 1 GeV/u and a nominal intensity of 10^9 particles per second (pps), impinging on a ^{9}Be target of 2.7 g/cm^2 thickness. The ions of interest were separated and selected from the produced cocktail of fragments and primary beam by the fragment separator FRS [84]. The beam had a macrostructure of 0.9-second spill-on and 1.7-second spill-off.

This chapter describes the experimental setup of the FRS and the DESPEC detector system developed for the investigation of exotic nuclei at GSI, Darmstadt. Furthermore, the data acquisition and processing of the setup will be discussed.

4.1 Accelerator Facility at GSI

The experiment was performed with a primary beam of ^{208}Pb. The ^{208}Pb was produced by the *Electron Cyclotron Resonance* (ECR) ion source providing highly charged ions, and accelerated by the *Universal Linear Accelerator* (UNILAC) [85]. UNILAC is a 120 m long particle accelerator which accelerates ions up to 20 percent of the speed of light and is able to accelerate any ion species from hydrogen to uranium (Z=92), with energies up to 11.4 MeV/u. The pre-accelerated beam from UNILAC is delivered via a transfer channel to the heavy-ion synchrotron (*SchwerIonen-Synchrotron*) SIS-18 [86], which accelerates the ions to relativistic energies. The SIS-18 synchrotron has a circumference of 216 m (radius of 34.5 m) and has 24 dipole magnets, which act to bend the ions with a maximum rigidity of $B\rho$ = 18 Tm [84, 87], permitting to accelerate ions up to about 90% of the speed of light. Figure 4.1 shows the schematic layout of the GSI facility.

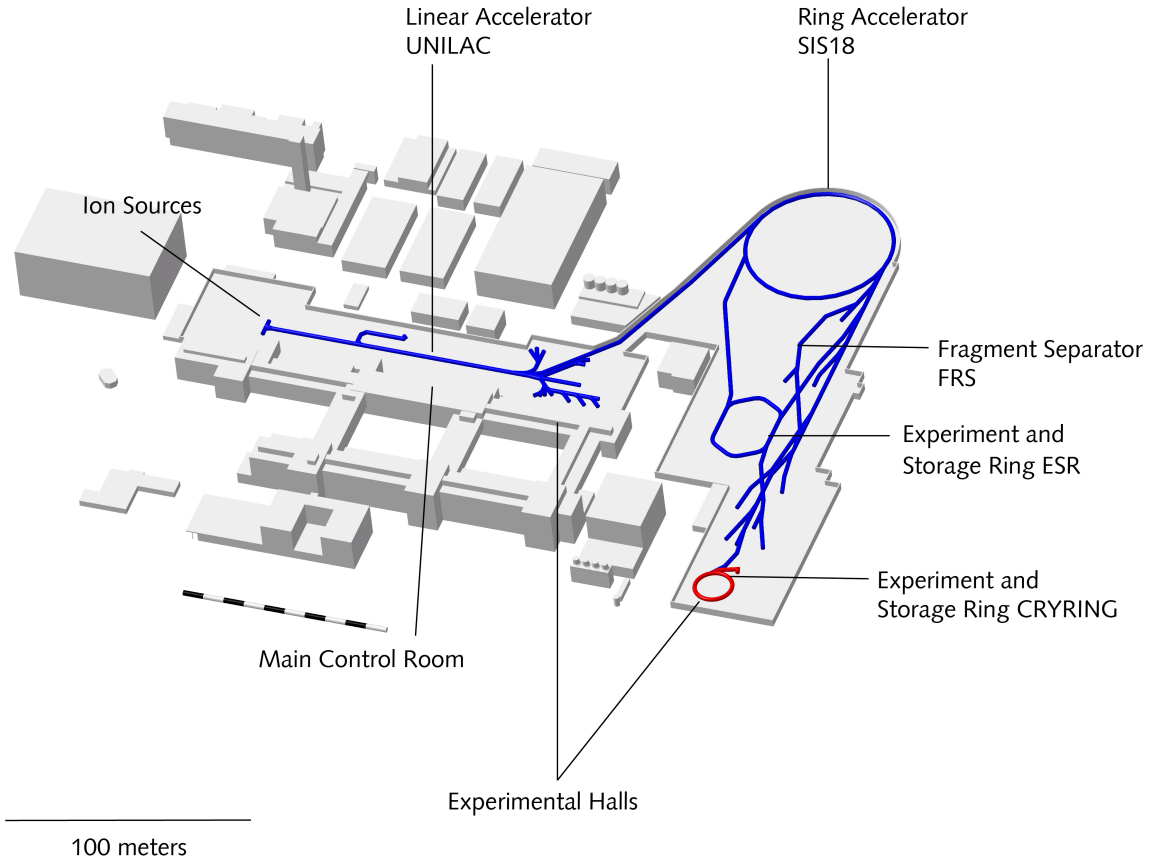

Figure 4.1: Schematic layout of the GSI facility. The UNILAC linear accelerator accelerates the stable primary beam. UNILAC injects the ion beam for further acceleration into the heavy ion synchrotron SIS-18. High-energy stable beams extracted from SIS-18 are transported to the fragment separator FRS. The FRS separates in-flight the radioactive isotopes produced in the target in-flight. The ions are then transported to the final focal planes of the FRS, to the experimental storage ring (ESR), or to the Target Hall.

4.2 The FRagment Separator FRS

The accelerated stable beam from the SIS-18 is delivered to the production target placed at the entrance to the spectrometer FRagment Separator (FRS). The FRS is designed in a way that it allows in-flight separation and selection of the fragments (produced in the production target) allowing for event-by-event identification. FRS has four focal planes, denoted as S1, S2, S3, and S4 (see Figure 4.2), which are used to identify particles by their position, angle, velocity and energy loss. The four sections of the FRS are composed of large dipole magnets at 30 degrees to separate the ions. It consists of sets of quadruple magnets before and after the magnetic dipoles to focus the beam. In addition, sextupole magnets enable for second-order ion-optical corrections in the focal planes. The FRS can operate in different ion-optical modes, depending on the desired goal of the individual experiment conducted. Two of these modes are the achromatic and the monoenergetic mode of operation. In the achromatic setting, ions with the same mass-over-charge A/Q ratio are focused at one single point in the final focal plane, therefore one can identify different nuclei according to their position in S4 focal plane. In the monoenergetic setting, the fragments have a certain energy in the final focal plane after the second $B\rho$ selection. This setting is suitable for β^- decay experiments, in which the maximum number of fragments are required to stop in a thin detector [88].

4.2.1 The Separation Method

The ions of interest are produced in the primary target and separated in-flight. The dipole magnets have an essential role in selecting the nuclei to be studied from the strongly populated contaminants. The first two dipoles apply the first separation acting as the momentum filter for the secondary cocktail beam, which has a large number of species, to the central dispersive focal plane S2. The heavy ions of interest are selected with the last two dipoles. Figure 4.3 shows the FRS setup in detail.

All of the separation of the isotopes of interest are performed by using the $B\rho$ - ΔE - $B\rho$ technique [84]. This technique is based on Lorentz Force Law. Magnetic fields (in this case provided by dipole magnets) apply force on a moving charged ion. The force $\vec{F}$ felt by a particle of charge q moving in the presence of a magnetic field $\vec{B}$ with velocity $\vec{v}$ is given by the Lorentz force law:

$$\vec{F}_{Lorentz} = q(\vec{v} \times \vec{B}), \tag{4.1}$$

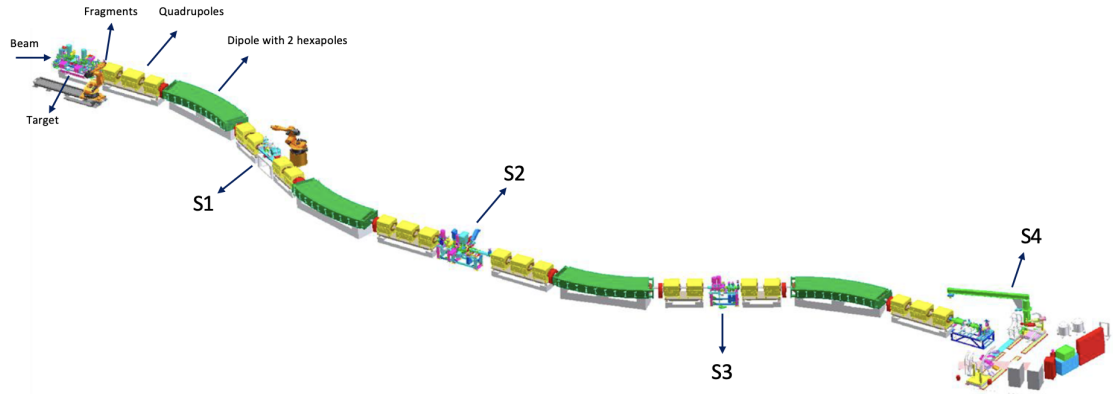

Figure 4.2: Schematic view of the fragment separator FRS with the main focal planes. The beam direction is from left to right. The production target is located before the first focal plane S1 to obtain the radioactive secondary beam of reaction fragments. The FRS has four large bending dipole magnets shown in green, quadrupole and sextupole magnets are shown in yellow.

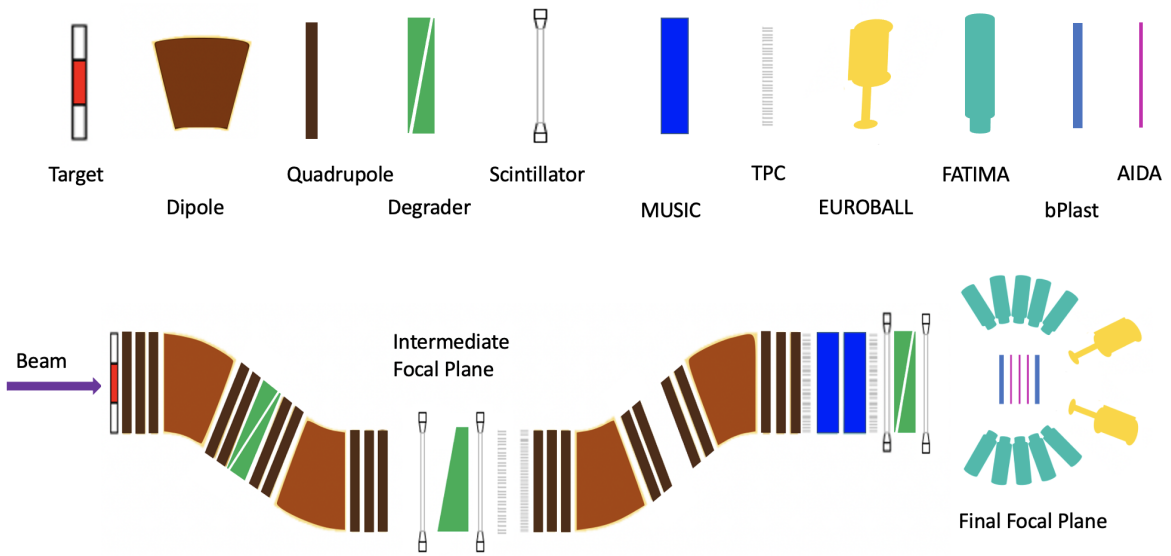

Figure 4.3: Schematic view of the FRagment Separator (FRS) setup showing the positions of the detectors along the beam line that provide unambiguous identification of new isotopes. The DESPEC setup is located at the final focal plane.

$\vec{B}$ and $\vec{v}$ are perpendicular to each other in the FRS setup and therefore the ion moves on a circular path. Hence, the Lorentz Force acts like a centrifugal force due to the circular motion of the ions.

$$F_{Lorentz} = \frac{mv^2}{\rho}, \tag{4.2}$$

where m is the mass of the particle, and ρ is the radius of the circular path. Combining Eq. (4.1) and Eq. (4.2), and solving for the magnetic rigidity, $B\rho$ is:

$$B\rho = \frac{p}{q} = \frac{\gamma m v}{q}, \tag{4.3}$$

where p is the momentum of relativistic particle and γ is the relativistic factor:

$$\gamma = \frac{1}{\sqrt{1-\frac{v^2}{c^2}}} = \sqrt{1/(1-\beta^2)}, \tag{4.4}$$

c is the speed of light. The relation of the velocity of the ion β and the relativistic factor γ is given by $\beta = v/c$. Therefore, $B\rho$ magnetic rigidity relation between A/Q becomes as:

$$B\rho = \frac{A}{Q}\left(\frac{uc\beta\gamma}{e}\right), \tag{4.5}$$

where A is the atomic mass number of the ions, u is the atomic mass unit, Q is the ionic charge and e is the electron charge. The bending radius of the circular path ρ is fixed to ρ_0 = 11.2641 m by the dipoles of the FRS. By changing the magnetic field value, A/Q mass over charge selection is made. The selected A/Q is physically centered, hence the contaminant ions will have a horizontal offset. Those contaminant ions can be stopped via slits inserted perpendicular to the beam direction, therefore they reduce the range of accepted $B\rho$. The FRS has five sets of slits along the beam line.

In order to separate the selected A/Q precisely, multiple degraders are placed in the focal planes to slow down the fragments and to separate the fragments with same A/Q ratio (i.e. according to their atomic number Z) (Figure 4.4). The energy loss ΔE in the degrader depends on the proton and mass number of the ions. A wedge-shaped degrader in S2 allows ions with different energies to pass through the non-uniform thick material and minimise the momentum spread. Multiple sets of quadrupole magnets provide horizontal and vertical

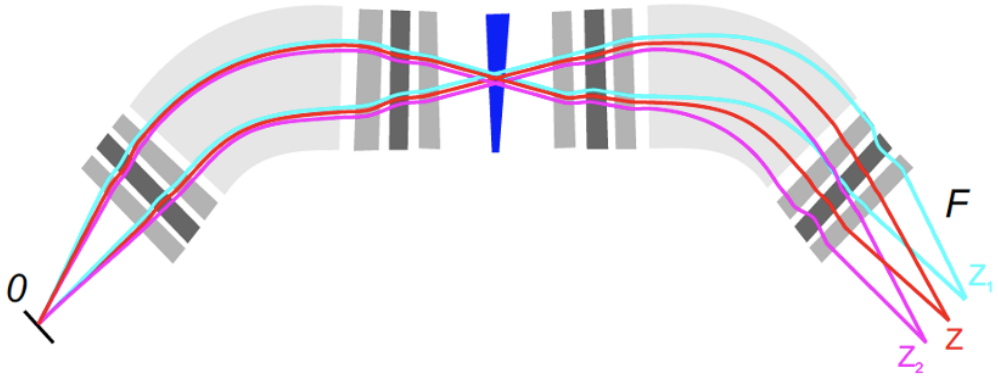

Figure 4.4: Schematic view of the selection mechanism of FRS with $B\rho$ - ΔE - $B\rho$ technique. O is the target, and F is the final focal plane. The wedge-shaped degrader in the intermediate focal plane shown in blue enables the separation of fragments with the same A/Q ratio according to their charge.

focusing of the ions at each focal plane of the FRS.

4.2.2 Particle identification detectors of the FRS

The FRS is capable of providing the mass and charge number of the nuclei in order to perform a *Particle IDentification* (PID) of the fragments in the last focal plane on an event-by-event basis. This requires different FRS detector systems to achieve the final particle identification by using the determination of the energy loss, time of flight and position of the ion. Therefore, it leads to the necessity of having different types of detectors for a multitude of measurements in the focal planes. Figure 4.5 shows the FRS detectors in the S2 and S4 areas, respectively.

Plastic Scintillator SCI

The plastic scintillators of the FRS provide *Time of Flight* (ToF) information of the ion between the intermediate (S2), and final focal (S4) planes to determine the A/Q of the ions. The S2 focal plane has two plastic scintillators (labelled in this work SCI21 and SCI22) placed upstream and downstream one after the other in the direction of the beam, respectively,

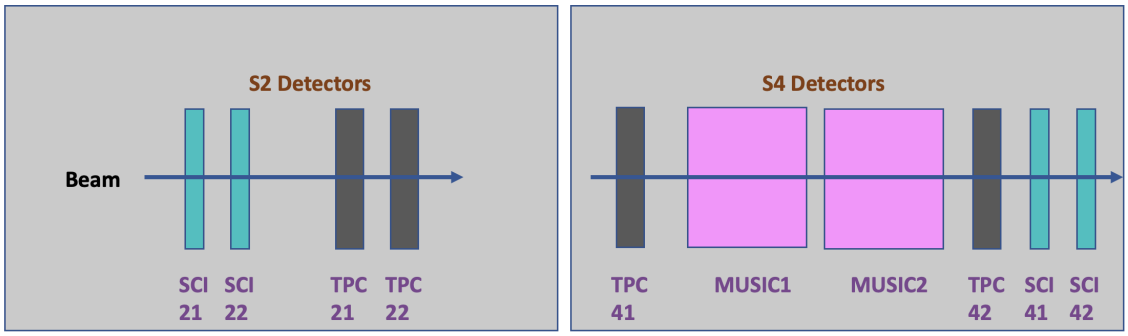

Figure 4.5: Schematic view of the FRS detector setup at the intermediate focal plane S2 and the final focal plane S4. The beam direction is from left to right. Two scintillator detector (SCI21, SCI22) and two Time Projection Chambers (TPC21, TPC22) are located at S2. Two scintillator detectors (SCI41, SCI42), two Time projection chambers (TPC41, TPC42) and an additional two multiple sampling ionization chambers (MUSIC1, MUSIC2) are located at S4. The identification of the isotopes is performed using the time of flight of the fragments measured with the scintillator detectors at S2 and S4, the energy deposition information from the MUSIC detectors to obtain the charge of the ions, and spatial position tracking from the TPCs.

separated by a wedge-shaped Al degrader. The S4 focal plane has two plastic scintillators labelled SCI41 and SCI42 (again upstream and downstream of one another) separated by an Al degrader with a thickness of 4.5 g/cm^2. Figure 4.6 shows one of the plastic scintillator detectors, FRS SCI42. The scintillators are composed of BC420 plastic material for use in ultra-fast timing and ultra-high counting applications with a size of 200x100 mm^2 for each of them. The thickness is around 1.04 mm for the S2 scintillators in the intermediate focal plane, and S4 scintillators were used around 1.0 mm at the focal plane. The sides of the scintillator detectors are coupled to HAMAMATSU H10580 *PhotoMultiplier Tubes* (PMTs) [89], where the light is converted to an electronic signal. The output of each PMT is split and sent to various electronic systems. The signals are sent to a *Constant-Fraction Discriminator* (CFD) and subsequently a *Time-to-Amplitude Converter* (TAC). Furthermore, they are sent to a *MultiHit Time to Digital Converter* (MHTDC). The final split signal is sent to a fast-timing module VFTX. Out of these three electronic options, the MHTDC was found to provide optimal results due to its ability to handle a higher number of counts.
A calibration of the ToF is required to determine the A/Q. The ToF calibration was performed by using the three different FRS degrader settings for the primary beam. This is discussed in Chapter 5.

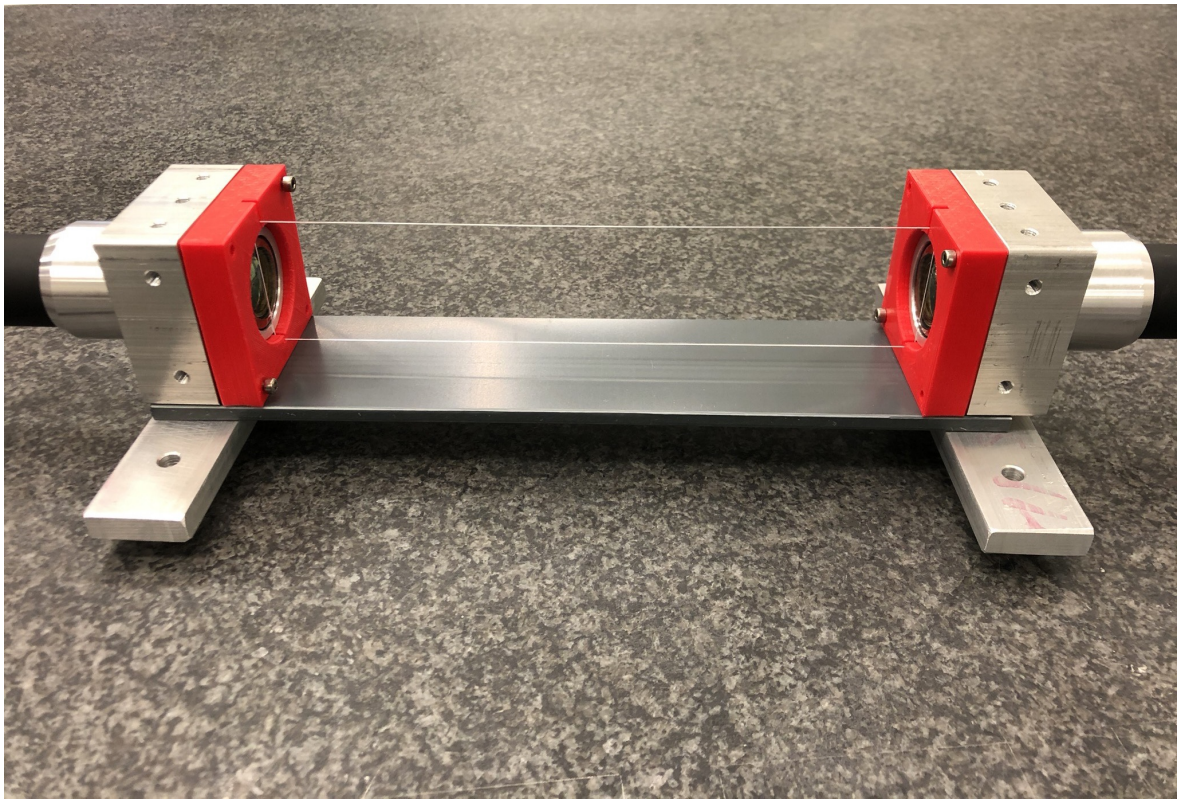

Figure 4.6: The FRS scintillator detector SCI42 used at S4. Picture taken from Ref. [89]

For this work, the time-of-flight was determined using SCI41 as the start time signal and SCI21 as the stop time signal (see Chapter 5 for the details). Equation (4.6) is the time difference between the start and stop signals used to calculate the ToF.

$$T_{TOF} = \frac{1}{2}\big((SCI21L + SCI21R) - (SCI41L + SCI41R)\big). \tag{4.6}$$

where L and R in this context refer to the left and right sides of the PMTs used for the scintillators.

β determination

The time of flight measurement between S2 and S4 using the scintillator detectors provides the velocity of the fragments. The distance between SCI21 and SCI41 is $x_0 \approx 36.77\ m$. The time of flight is given by Eq (4.7)

$$T_{TOF} = \frac{x_0}{v}, \tag{4.7}$$

where v is the velocity of the traveling ions and $\beta = v/c$, where c is the speed of light. The β is then related to the ToF through

$$\beta = \frac{1}{c}\frac{x_0}{T_{TOF}}. \tag{4.8}$$

The experimental ToF value is obtained by using Equation (4.6). Therefore, the A/Q can be obtained by combining Equation (4.5) and Equation (4.8):

$$\frac{A}{Q} = \frac{1}{f}\frac{B\rho}{\gamma\beta c}, \tag{4.9}$$

where f is the conversion factor between atomic mass unit and MeV c^{-2}.

MUltiple Sampling Ionization Chamber MUSIC

As mentioned in the previous section, ions with different atomic numbers Z can have the same A/Q ratio. In order to eliminate undesirable isotopes after the dipoles at S2, a wedge-shaped degrader helps to separate isotopes. It is crucial to determine the atomic number of the nuclei in order to be able to finalise the particle identification at the last focal plane S4. Hence, the *MUltiple Sampling Ionization Chambers* (MUSICs) [90] provide the Z value based on the energy loss of the ions in S4. The MUSIC detector consists of a gas cell filled with 90% Ar + 10% CH_4 (P10) operated at room temperature and atmospheric pressure. The active area of MUSIC is 200 mm x 80 mm and the active length is 400 mm. The working principle of MUSIC is to apply an electric field between the cathode plate and eight anode strips (each of which has a 50 mm active length). The electrons inside the detector are collected by the eight anode strips. A schematic layout of MUSIC is shown in Figure 4.7.

The distribution of the energy loss in the MUSIC detector is related to the Z of the ion passing through the gas since the gas cell becomes ionised by the particle passing through the detector. The relation between the energy deposition in the MUSIC detector and the Z of the ion is given by the Bethe-Bloch equation [91]:

$$-\frac{dE}{dx} = Z^2 f(\beta), \tag{4.10}$$

where $f(\beta)$ is a function of the speed of the ion, which can be calculated by using the primary beam. In this way, the Z of the ion can be obtained by getting ΔE and $f(\beta)$ in the material. Due to the fact that MUSIC has eight anode strips, the energy deposition of the fragments in

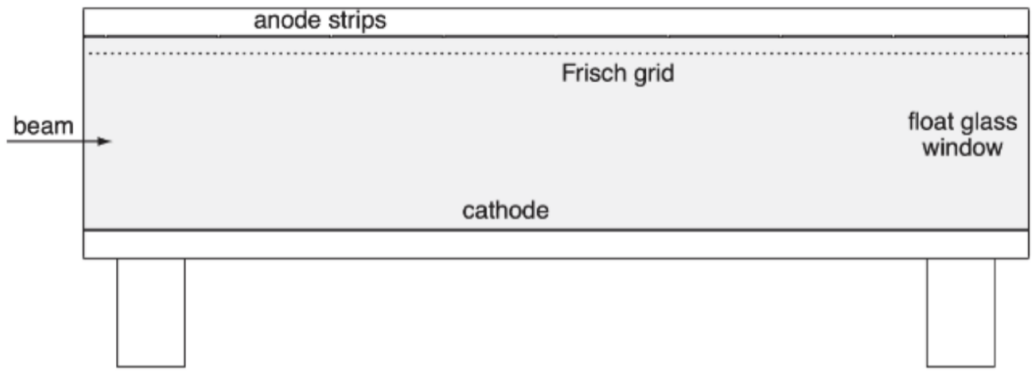

Figure 4.7: FRS MUltiple Sampling Ionization Chamber detector. Picture taken from Ref. [90]

the ionisation chamber MUSIC is derived as the geometric mean value of the anode signals given by equation (4.11)

$$\Delta E = \sqrt[8]{\prod_{i=1}^{8} \Delta E_i}. \tag{4.11}$$

Time projection chamber detector (TPC)

Time projection chamber (TPC) detectors [92] are position-sensitive detectors and serve as a high-resolution ion tracker along the beam line. They consist of a drift chamber with the drift volume of the detector vertical with respect to the beam direction. The space between a cathode plate and a shielding grid (Frisch grid) is filled with Ar + %10 CH_4 (P10) at room temperature and normal pressure. Four proportional anode wires, 20 μm diameter each, are connected to C-pad cathodes which are placed underneath the grid, as shown in Figure 4.8. Each C-pad is connected to two independent integrated delay line chips. A uniform high voltage of 400 Vcm^{-1} is applied across the detector. The fragments enter this drift volume and ionise the gas mixture inside the TPC. The ionised electrons are collected by the anode and the positive charges are deposited onto the cathode. The drift time of these produced electrons to each anode, inside the TPC, provides four measurements of the vertical position. The signals of the anodes are split into two parts: left and right. A comparison of the signals of two delay lines connected to the cathodes provides information

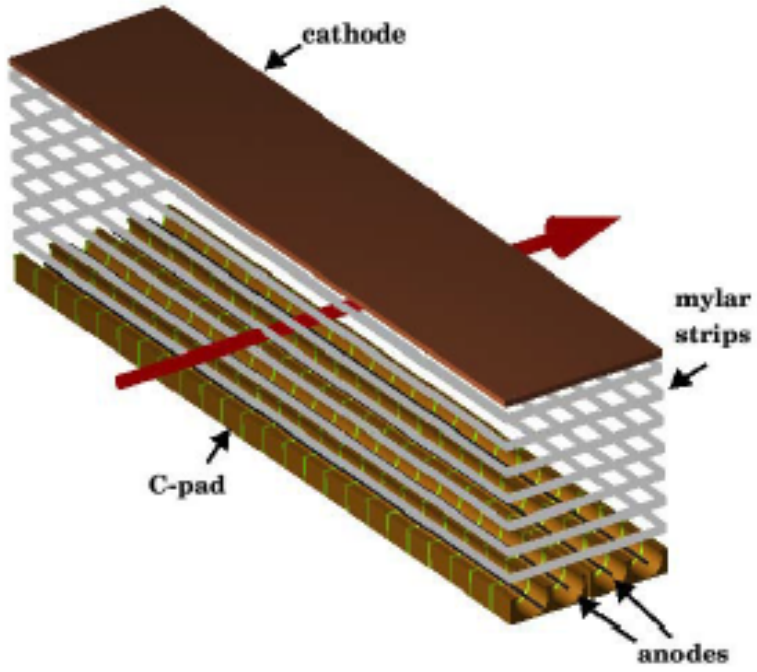

Figure 4.8: Schematic view of a time projection chamber (TPC) in the FRS.

on two independent horizontal positions. An accurate position determination is obtained by the presence of precise delay lines. The horizontal position resolution is around 0.1 mm, whereas the vertical position resolution is around 0.05 mm.

4.3 DESPEC detector setup

The fundamental properties of exotic nuclei such as decay half-lives, isomerism and branching ratios can ultimately shed light on long-standing questions in nuclear physics. The *DEcay SPECtroscopy* (DESPEC) [2] project has been developed as part of an international effort, to perform β, α, γ, neutron and proton spectroscopy of exotic nuclei. These measurements utilise a combination of γ-ray spectrometers for fast-timing (FATIMA) [30] in conjunction with HPGe detectors (EUROBALL) [93] for high-resolution energy measurements, highly-pixilated silicon detectors (AIDA) [94, 95, 96] for ion implantation and subsequent nuclear decays, coupled with scintillator detectors for β-decay measurements (βPlastic) [2].

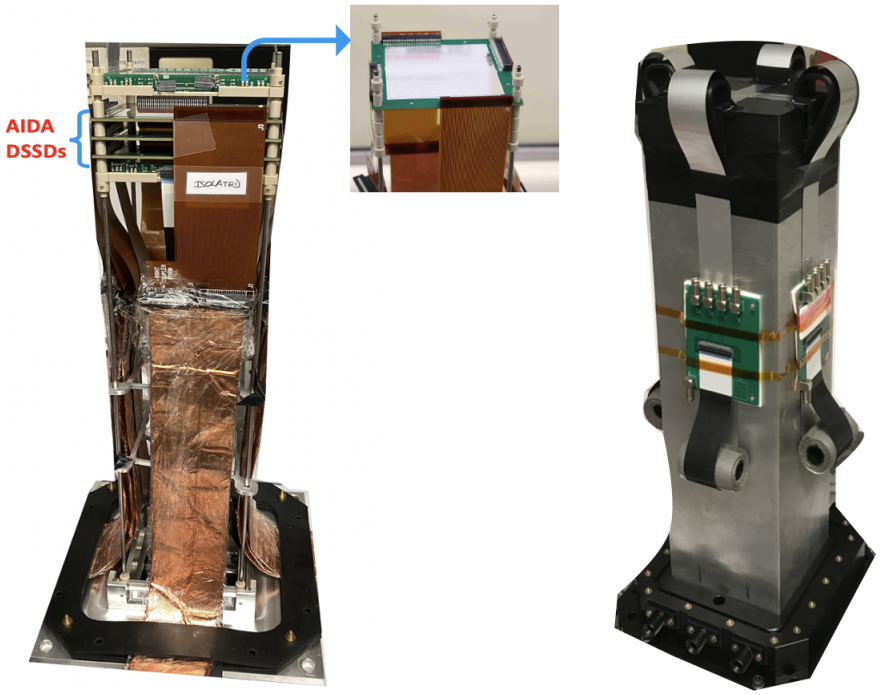

Figure 4.9: Schematic view of AIDA used in the experiment. The left photograph is the arrangement of three units of AIDA DSSD stack coupled to two of the βPlastic detectors. The middle photograph is one of the DSSD layers of AIDA. The right photograph is the snout that houses AIDA DSSDs as well as the βPlastic detectors.

4.3.1 AIDA

The detection of charged particles and their subsequent decay can unlock a wealth of information when performing decay spectroscopy studies on neutron-rich nuclei. The *Advanced Implantation Detector Array* (AIDA) [94, 95, 96] is one of the latest generations of multiple high-degree pixelation *Double Sided Silicon-Strip Detector* (DSSD) that used in the DESPEC campaign to measure implant-decay correlations. The detector is located at the final focal plane (S4) of the FRS to determine the implanted ions and their subsequent charged particle decays ($\beta^{\pm}$, α, proton, and internal conversion electrons). DSSDs offer precise and imperceptible detection capabilities, providing detailed spatial information in terms of horizontal (X) and vertical (Y) positioning, as well as time resolution.

AIDA can have two configurations. The first (employed in this study) is composed of a single stack of three DSSD units, each with an active area of 8×8 cm^2. The second configuration has six DSSDs stacked in two layers for a total active area of 24×8 cm^2.

The DSSDs are placed in a snout structure which is covered and located within a light-tight aluminium box acting as a Faraday shield for electromagnetic noise. Each DSSD has a thickness of 1 mm per detector. Figure 6.5 shows the single stack configuration of AIDA and Figure 6.5 shows the snout that was used in the experiment. The exotic ions reach AIDA with energies of several GeV. If a radioactive ion is stopped in a DSSD, the radiation emitted in its subsequent decay deposits energy in the range from tens of keV to a couple of MeV into AIDA in order to be able to process signals across this large energy range, AIDA a dedicated electronic unit. The detector uses an *Application Specific Integrated Circuit* (ASIC) [97] chip, which serves the purpose of having a switchable gain range, measuring high and low energy ranges of the charged particles and autonomously switching between them with the fast recovery time and generate low of background data.

The AIDA hardware comprises a number of 64-channel *Front-End Electronics* (FEE64) modules to support a precise correlation between high-rate implantation events and their subsequent decays via 64 channels of instrumentation. Four FEE64 modules are needed to read out one single-wafer DSSD. AIDA runs under a triggerless system based on the *Multi Instance Data Acquisition System* (MIDAS) DAQ [98] for total data readout.

The front-end electronics cards of the detector support precise correlations between high-rate implantation events and their subsequent decay via 64 channels of instrumentation. The FEE64 cards have Analogue to Digital Converters (ADCs) to provide the signal processing, as well as a Field Programmable Gate Array (FPGA) for control, signal processing and data management.

4.3.2 FAst TIMing Array (FATIMA)

The FAst TIMing Array (FATIMA) [30] is a high-granularity fast-timing γ-ray detection array developed for the DESPEC experiment. FATIMA is devoted to perform direct determination of nuclear-excited states lifetimes and provides excellent intrinsic time resolution on the order of 200 ps [30]. The determination of lifetimes down to the order of tens of picoseconds is possible in delayed γ-γ coincidence measurements with FATIMA. Thus, FATIMA can be used as an essential tool used to study the lifetimes of excited nuclear states in neuron-rich nuclei, performing fast-timing experiments in radioactive beam facilities such as GSI and FAIR.

FATIMA has been used at DESPEC for the study discussed here. The FATIMA detector surrounded AIDA and the βPlastic detector in close configuration to achieve optimal efficiency. The system comprised 36 cerium-doped lanthanum tri-bromide ($LaBr_3$(Ce)) scintillator crystals coupled to photomultiplier tubes. Cerium doped lanthanum tri-bromide is

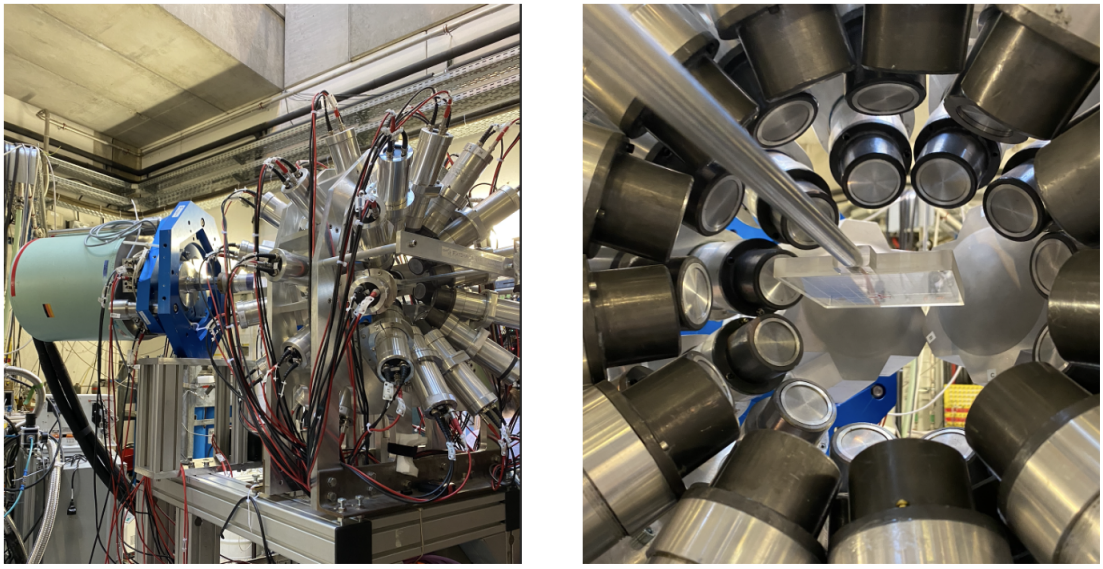

Figure 4.10: Left: Photograph of the FATIMA array and EUROBALL germanium clusters that were used in the experiment at S4. Right: Photograph of the centre of the FATIMA array, with the $LaBr_3(Ce)$ detectors coupled to PMTs. In the centre, a plastic tray holding the γ-ray sources is shown.

an inorganic, scintillating crystal developed for the application of γ-ray spectroscopy. The $LaBr_3(Ce)$ scintillator crystal is composed of cerium (5%), lanthanum (23.75%) and bromine (71.25%). The working principle of scintillator detectors is based on converting the wavelength of energetic particles such as γ rays or α particles, into a significant number of photons with longer wavelength (or smaller energy). The $LaBr_3(Ce)$ detectors are $\varnothing$ 1.5" x 2", each coupled to a Hamamatsu photomultiplier tube R9779. Each crystal is surrounded by 5 mm thick removable lead shielding to reduce scattering between neighbouring crystals, in particular Compton scattering. The front face of the $LaBr_3(Ce)$ cylindrical crystal is packed inside an aluminium housing for protection. The geometry of the FATIMA array can be changed from experiment to experiment depending upon the measurement of interest. For the DESPEC campaign, the core system geometry is arranged in a way that provides both a good time and energy resolution and is able to measure γ-ray energies up to 4 MeV [99]. The FATIMA detectors were placed in three rings. Each ring accommodated 12 $LaBr_3(Ce)$ detectors. Figure 4.10 left shows the FATIMA array in the experiment. Figure 4.10 right shows the detector crystals with a plastic tray for holding γ-ray sources located at the centre of the array.

The PMTs of the detectors are biased with a negative voltage by using three CAEN SY4527 units coupled with three A1535D *High Voltage* (HV) supply cards. The detectors were op-

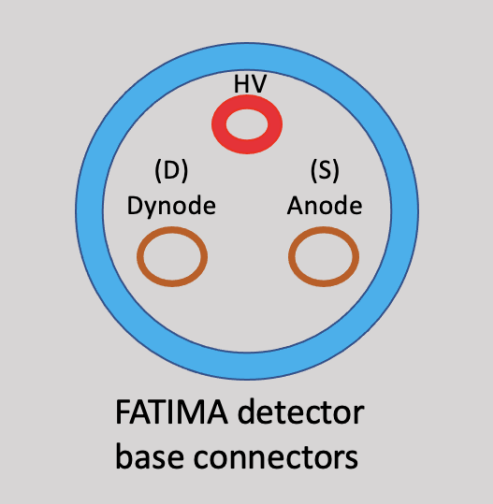

Figure 4.11: Signal connections for a FATIMA showing the positions of the high voltage power output, the dynode signal output and the anode signal output.

erated at around -1200 V during the experiment. The PMTs feature two outputs to extract the energy and time independently. While the anode is responsible for the time information, the dynode is responsible for the energy information. The anode signals were split into two using a passive splitter and fed to the two different electronic configurations for data acquisition, readout, and processing. The two configurations used were the so-called VME branch and the TAMEX4 branch. A detailed description can be found below. For the VME system, the energy signal was taken from the last dynode of the 8-stage PMT and read out by CAEN V1751 digitisers. The digitiser is able to perform the Digital Pulse Processing-Pulse Shape Discrimination (DPP-PSD) by offering a sampling rate of 1 GS/s. A signal integration via charge-to-digital conversion (QDC) provides energy information. The time signal from the anode is passed to CAEN V812 constant fraction discriminator (CFD) modules and then fed into CAEN V1290 time to digital converters (TDC) modules. The second electronics configuration, TAMEX4, is a new multichannel front-end electronics card that has been developed by the department of experimental electronics at GSI. It is an FPGA-based multi-hit TDC with a high-precision measurement of leading and trailing edge times. The *TwinPeaks* (TP) charge to time amplifier front-end board is connected to TAMEX4 for the $LaBr_3$(Ce) detectors. TP contains 16 analog inputs, each input is split into two branches providing 'fast' and 'slow' information. The slow branch is responsible for the linearised charge-to-time output, therefore the energy information from the detector can be directly converted into a pulse width spectrum. The fast branch has a logarithmic energy dependence and is used to obtain the time information. Slow and fast branch of the TP display for the energy measurement via a charge measurement through the *Time-over-Threshold* (ToT) method [100], which relates

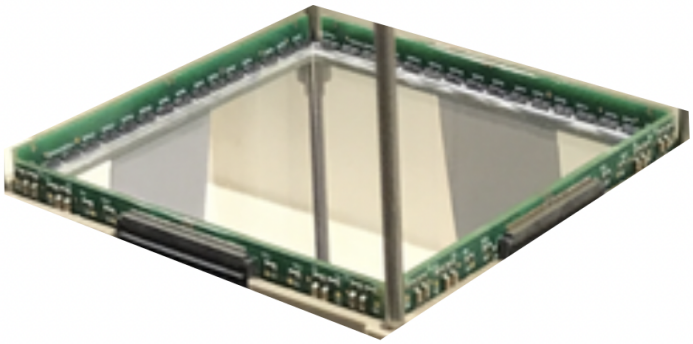

Figure 4.12: βPlastic detector used for the experiment.

to the widths of the pulses. The *Gigabit Optical Serial Interface Protocol* (GOSIP) provides communication via optical fibres between multiple front-end electronics in the readout host PC [101].

4.3.3 βPlastic

Plastic scintillator detectors are used in decay spectroscopy experiments requiring fast (i.e. ps) timing, due to their excellent time response and low-stopping power [77]. βPlastic is a fast-timing plastic scintillator detector largely used for β particles with an energy range of $\sim$80 keV to 8 MeV [2]. It allows for precise timing between β-particles and γ-rays detected in FATIMA. The βPlastic can further be used as a veto detector during the experiment to confirm implantation. The detector was constructed in-house by the γ-spectroscopy group at GSI. βPlastic detectors have the same size as the AIDA DSSDs, with an 8x8 cm^2 cuboid with a thickness of 3 mm. Two βPlastic detectors were placed in the DESPEC setup, located in the upstream and the downstream positions relative to the direction of the incoming ions, sandwiching the AIDA DSSDs in a close configuration.

Each of the four edges of a scintillator pane is equipped with 16 silicon photomultipliers (SiPMs) from SensL (C-Series [102]). The SiPMs have an active area of 3$\times$3 mm^2 and are operated with a bias voltage of less than 30 V.

The detector dimensions as well as the number of SiPMs can be customised for different experiments. 16 SiPMs along each side were arranged in a way that a group of 4 SiPMs are

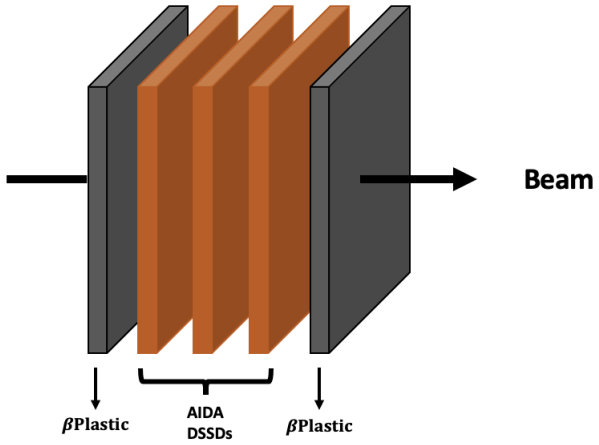

Figure 4.13: Schematic view of the AIDA DSSD stack sandwiched in between two βPlastic detectors downstream and upstream, respectively.

coupled to a readout. A total of 16 read-out channels of a βPlastic detector were connected to the TAMEX4 data acquisition. The TAMEX4 electronics card is capable of determining both the leading and the trailing edges of each threshold discriminator signal (Time-over-Threshold, ToT). The ToT technique is based on time-tagging of the leading and trailing edge of the SiPM signal above at a certain threshold. The time width of the signal provides the proportional information of light collected by the SiPMs. The βPlastic detector can achieve a time resolution of the order of a few hundred of ps, which is superior to the time response of the DSSDs. The implanted fragment and the subsequent β decay in AIDA are time stamped and AIDA additionally provides information on the implant position with mm precision. By correlating decay events in AIDA and βPlastic, one can combine the power of both instruments. AIDA, by implant-decay correlation, can determine the energy, position and time of the decaying ion. The βPlastic detector then provides high precision time information for the decay. In combination with FATIMA, sub-nanosecond beta-gamma timing is feasible with a radioactive ion beam.

4.3.4 EUROBALL Cluster

High-purity germanium detectors (HPGe detectors) are semiconductor devices which provide efficient and precise γ-ray spectroscopy. Coaxial n-type germanium EUROBALL [93] cluster detectors which were employed in the RISING (Rare ISotope INvestigations at GSI) campaign, were used in this study. Each cluster detector houses seven closely packed tapered

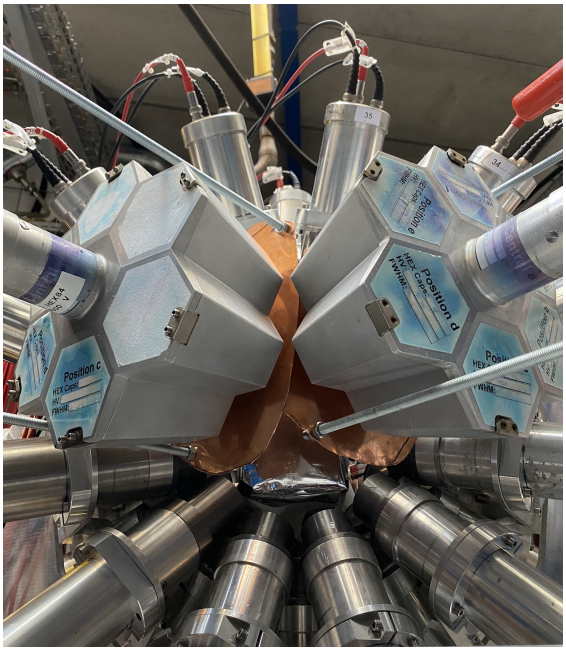

Figure 4.14: Two EUROBALL HPGe cluster detectors and FATIMA were used in the experiment. Each EUROBALL cluster consists of seven Ge crystals inside a single cryostat.

hexagonal Ge crystals inside a common cryostat. Each of the Ge crystals is 70 mm diameter and 78 mm long and is tapered at the front. Due to the possibility to sum (add-back) the energies measured in neighbouring crystals after Compton scattering, the EUROBALL crystals are encapsulated in a permanently sealed aluminium can ("crystal capsule").

In this experiment, two EUROBALL cluster detectors, each equipped with seven large-volume crystals, were positioned downstream at an angle relative to the beam axis and 15 cm away from the center of AIDA. The add-back efficiency is around 3% at 1 MeV [2]. The EUROBALL array was combined with the FATIMA array to detect γ rays. Although FATIMA has superior time resolution, the HPGe offers excellent energy resolution. The use of the HPGe detector for monitoring purposes allowed us to check the experimental conditions (i.e. ions with an isomer implanting correctly). Figure 4.10 shows the EUROBALL combined with FATIMA and Figure 4.14 shows the EUROBALL clusters during the experiment. The data acquisition of the EUROBALL clusters used the *Front End Board with optical link Extension* (FEBEX) [103] modules which were developed by the Experiment Electronics Department of GSI. The FEBEX boards host a 14-bit pipelining ADC with 16 channels and up to 100 MHz sampling frequency. An FPGA contains the General Optical Signal Interface Protocol (GOSIP) data transfer and provides a programmable fast trapezoidal filter for hit finding, and a slower trapezoidal filter to extract the energy measurement of each detected

hit. FEBEX can be applied for data acquisition with a local "self-triggered" readout. Different addon-boards are available to suit FEBEX for multiple numbers of experimental use cases [101].

4.3.5 The Data Acquisition System

Each individual subsystem of the DESPEC setup requires a complex data acquisition framework. The data acquisition must handle synchronisation between the various components. The DESPEC subsystems for the experiment (excluding AIDA) use the GSI-developed *Multi-Branch-System* (MBS) [104] DAQ framework. The aim of the MBS DAQ is to establish memory mappings to access the DAQ modules and to process trigger synchronisation between various subsystems. Each subsystem of DESPEC has its own MBS DAQ. The individual DAQ systems are then merged (including AIDA) using a timesorter event builder from where the data is stored to both the lustre file server and the GSI tape robot. *White Rabbit* (WR) [105] is the general machine timing system used at GSI. Timestamp synchronisation of several MBS DAQs at GSI is derived from the WR timing. It enables synchronization of globally triggered readout branches, as well as locally triggered systems.

The *"Unpack and check every single bit"* (Ucesb) [108] program is a tool that reads and unpacks the time-sorted data. Ucesb is employed after the MBS stage, in order to build AIDA events and to combine the data into a time-stitched format via WR. In this process, temporally close events from different subsystems are combined by time-stitching into an MBS. This can be seen as an example in Figure 4.16. Data recorded by a data acquisition system must be unpacked and sorted into a readable format for analysis. For this we used custom wrote C++ code, based on the GSI Go4 analysis software with the underlying architecture in ROOT [109] to process the large volumes of data (on the order of 10 TB). By using the GSI computing cluster Virgo, data processing times were on the order of two to three hours for the full experimental data set. After the creation of ROOT histograms, these could be analysed using custom-written scripts. More details on the analysis processes can be found in the Experimental Results chapter.

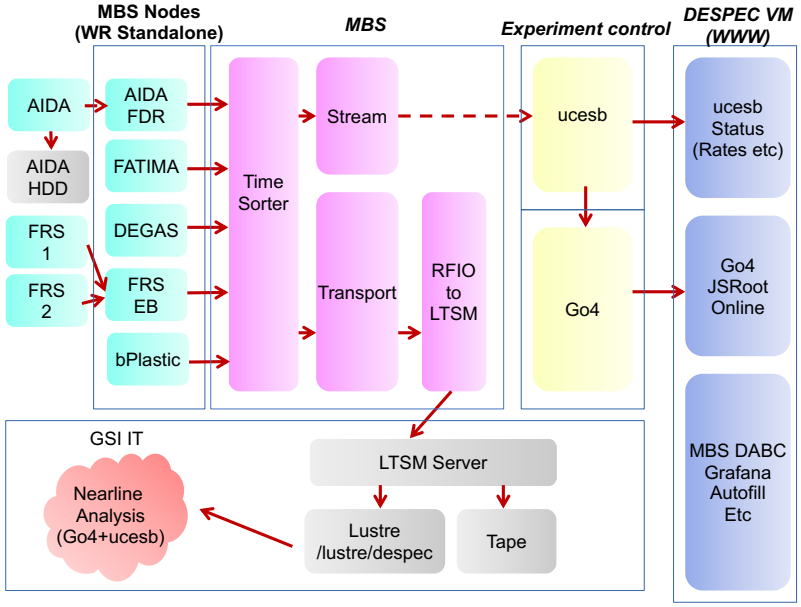

Figure 4.15: Schematic of the DAQ architecture used in this experiment. Data from the individual subsystems (orange squares) are fed into a timesorter for event building. From the stream server branch, they are sent to the ucesb timesticher which serves to stitch subevents based on the White Rabbit common clock. The data are streamed to the Go4 online analysis, with both ucesb and Go4 linked to the World Wide Web via the Apache fastCGI webserver [106]. From the transport server, they are stored to magnetic tape and to the Lustre file server, in parallel, via Lightweight Tivoli Storage Manager (LTSM) [107]. The data can be accessed for near-line analysis on the GSI cluster computing service.

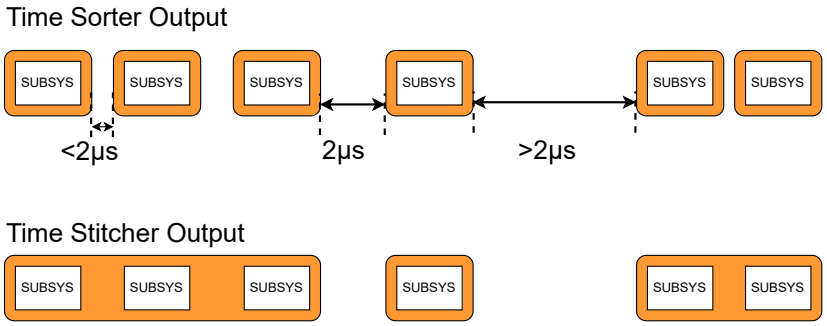

Figure 4.16: Schematic of the ucesb time-stitching algorithm used in this study. Events from subsystems occurring less than 2 μs from the previous event are grouped together.

5 Corrections and Calibrations

The current chapter is dedicated to providing a comprehensive overview of the calibration and correction procedures that are crucial for obtaining optimal results from the FRS. The procedures outlined in this chapter are intended to guide the reader through each step of the process and ensure that the analysis is as accurate as possible. Additionally, this chapter also delves into the details of the data preparation, calibration, and analysis procedure of the DESPEC setup. The aim is to provide a clear and thorough understanding of the techniques used to obtain reliable and high-quality data from the FRS and the DESPEC setup.

5.1 Calibrations and corrections of the FRS experimental setup

In order to obtain the final particle identification plot that includes the calibrated Z and A/Q ratio, it was necessary to carry out a calibration of the FRS detectors. This calibration process ensures that the detectors are able to accurately measure and identify the particles that pass through them. It is an essential step in obtaining accurate and reliable data from the FRS, and it plays a critical role in the overall analysis process.

5.1.1 Calibration of MUSIC

As previously discussed in Chapter 4, the energy loss of an ion passing through a material can be used to obtain information about the atomic number Z of ion. As stated in Equation (4.10), the energy loss depends on both atomic number Z and velocity of the ion. Therefore, in order to obtain the final atomic number of the ions of interest, a calibration of the MUSIC detector was carried out. This calibration was performed by varying the primary beam energies with three different degrader settings *i*) no degrader, *ii*) degrader at S1 and *iii*) degraders at S1 and S2. By assuming that the ions are fully stripped ($q = Z$), the calibration was done using Equation 5.1. This calibration process allowed us to accurately determine the atomic number of the ions passing through the MUSIC detector, which is vital for obtaining accurate and reliable results from the FRS. The calibration process also plays an essential role in the overall analysis of the data collected by the FRS.

$$Z_f = Z_p \sqrt{\frac{\Delta E_f}{a_0 + a_1\beta + a_2\beta^2}}. \tag{5.1}$$

In this equation, Z_f represents the proton number of the fragments, Z_p represents the known proton number of the primary beam, and ΔE_f represents the fragments energy loss. The energy loss of the fragment in the gas is determined by collecting, on the anodes, the charge coming from the ionisation in the gas of the MUSIC detectors. A preamplifier and amplifier are used to convert the collected charge into an amplitude signal, which is then sent to an Analog to Digital Converter (ADC). The value of the energy loss shown in Figure 5.1 is the centroid of the pulse height distribution recorded in the ADC channel. In this thesis, the atomic number determined from MUSIC1 is referred to as $Z1$, and the atomic number determined from MUSIC2 is referred to as $Z2$. The free parameters a_0, a_1 and a_2 are also present in this equation. The fitting parameters for the calibration are presented in Table 5.1. These parameters are critical for the calibration process and allow us to accurately determine the atomic number of the ions passing through the MUSIC detector.

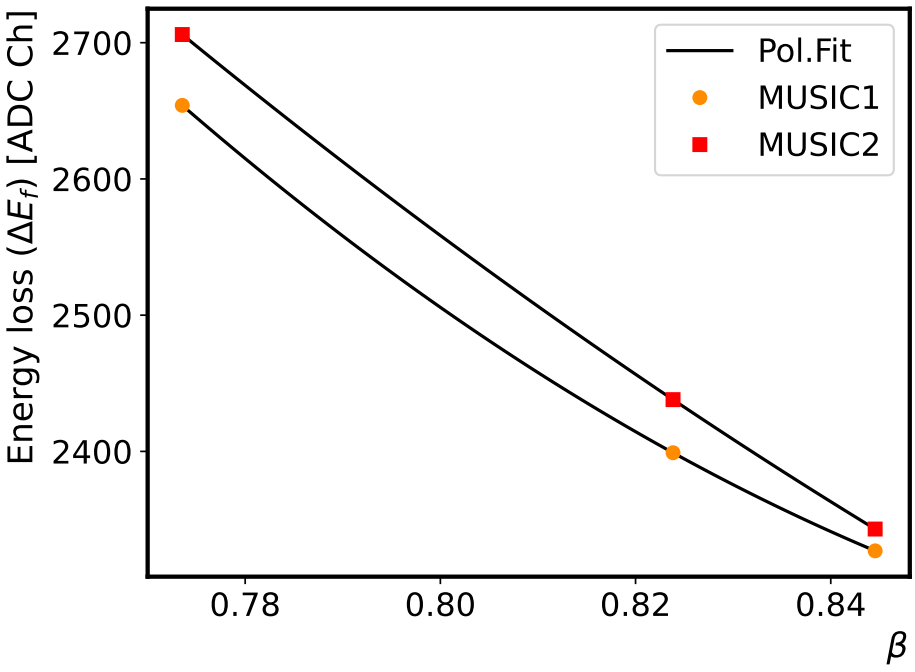

Figure 5.1: The energy loss in MUSIC1 and MUSIC2 versus three different β values of ^{208}Pb primary beam obtained by inserting different degrader settings at S1 and at S2 focal planes. The data are fitted with a third-order of polynomial function (Pol. Fit)

The MUSIC detectors are known to be sensitive to changes in atmospheric pressure and temperature. As the ambient conditions change, the Z values obtained from the MUSIC

Table 5.1: Fitting parameters for the MUSIC calibration.

Parameter	MUSIC1	MUSIC2
a_0	20888	13490
a_1	-40943	-22027
a_2	22456	10453

detectors can also change, leading to drifts in the data. In order to correct these drifts, a correction procedure needs to be applied. The drift correction was performed with the alignment of $Z1$ and $Z2$ on a run-by-run basis and adding the determined offset values to obtain the final corrected Z values for both detectors. Figure 5.2 illustrates these drifts for the $Z1$ values and the corrected $Z1$ values from the MUSIC1 detector for the data across the entire experiment. The same correction procedure was also applied to the $Z2$ values from the MUSIC2 detector. Once the calibration and correction procedures were completed for both MUSIC detectors, the final Z value for the experimental data was obtained, as shown in figure 5.3. This final Z value represents a much more accurate and reliable representation of the atomic numbers of the ions.

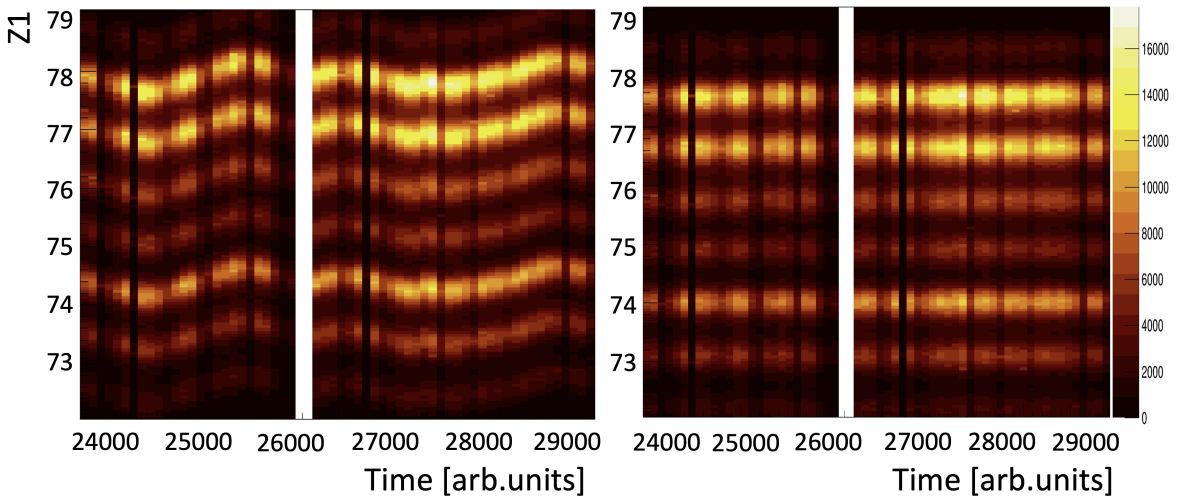

Figure 5.2: Left: uncorrected $Z1$ drift in time for the full range of time for the experiment. Right: corrected $Z1$ drift in time.

5.1.2 Calibration of ToF

In Chapter 4, the method for determining the Time of Flight (ToF) of the fragments in the FRS is explained. This is accomplished by measuring the time difference between the signals received from the scintillators SCI21/SCI22 and SCI41, which allows for the calculation of

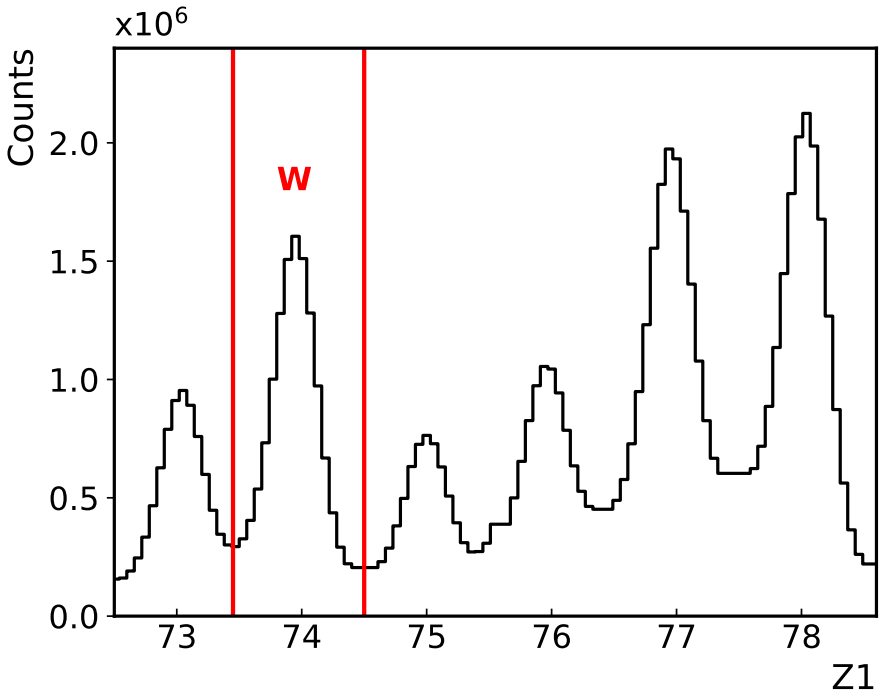

Figure 5.3: $Z1$ obtained from the energy loss information in MUSIC1 and calibrated using the primary beam. The Z value between red lines represents tungsten isotopes.

the velocity, or beta (β), of the beam particles. To achieve this, the signal from detector S4 is used as the start point in the Time to Amplitude Converter (TAC), while the signal from detector S2 serves as the stop point. This is done because the count rate at S2 is much higher than at S4, therefore SCI41 was used as a trigger in the experiment and SCI21 signal was received after the delay module. The relationship between β and ToF is described by equation (4.8). However, due to variations in signal transmission time between the scintillators caused by the delay due to the different lengths of the cables, an offset related to the β value may occur. To correct for this, the path of the particle (x_0) and the ToF offset (ToF_{offset}) are determined through the use of the primary beam as a calibration tool. By adjusting the energy (and thus velocity) of the primary beam through the use of different degrader thicknesses, the relationship between ToF and β from the following equation can be accurately determined.

$$ToF = \frac{b_0}{\beta} + b_1, \tag{5.2}$$

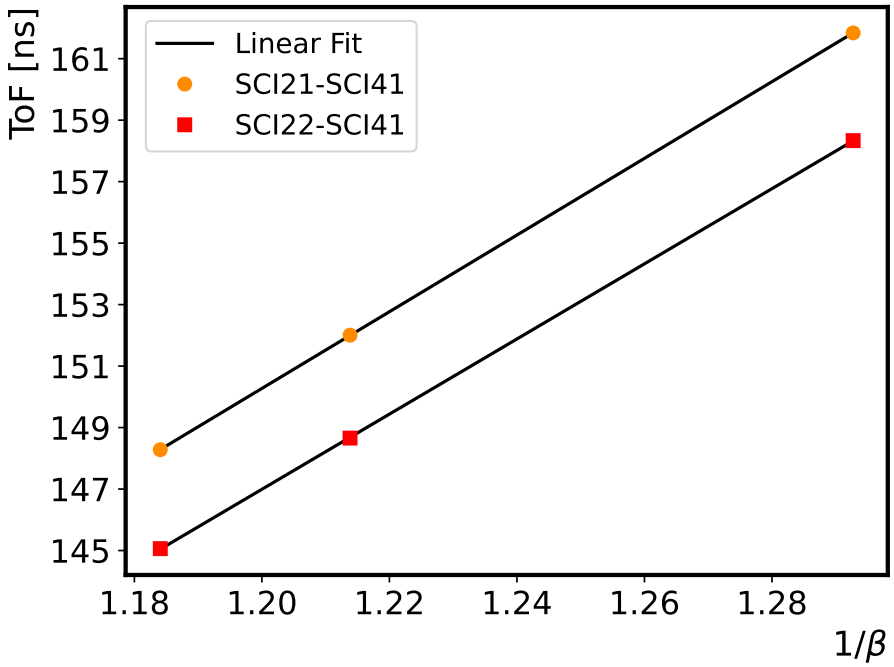

Figure 5.4: ToF calibration for SCI21-SCI41 and SCI22-SCI41 with the three known velocities (β) of the primary beam.

two parameters b_0 and b_1, where b_0 represents the value of x_0/c and b_1 represents the ToF_{offset}. To correct for any offset that may occur due to variations in signal transmission time between the scintillators, a first-order polynomial is used for ToF calibration.

Figure 5.4 illustrates the ToF calibration for SCI41-SCI21 and SCI41-SCI22 and Table 5.2 presents the calibration parameters obtained from the fit. The offset for this experiment was measured to be $ToF_{offset} = 173.82$ ns and $x_0 = 36.7760$ m.

Furthermore, Figure 5.5 shows the ToF measurement between SCI21 and SCI41, which is obtained by using the calibrated parameters and provides an accurate representation of the velocity of the beam particles. Overall, this process is a crucial aspect of the experiment, as it ensures that the results obtained are accurate and reliable.

Table 5.2: Fitting parameters for the ToF calibration.

Parameter	SCI21-SCI41	SCI22-SCI41
b_0	0.5896	0.3092
b_1	124.74	122.24

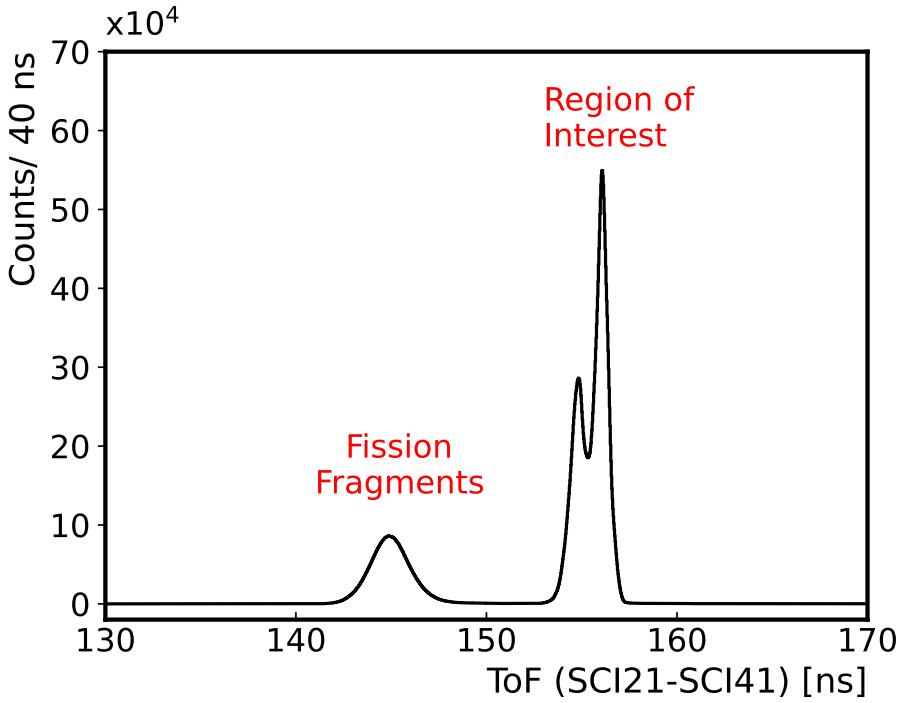

Figure 5.5: ToF measurement between SCI21-SCI41. Simulation show that fragments from the fission of the primary beam ^{208}Pb are transmitted, this happens because, despite the $B\rho$ selection of the spectrometer, the fission fragment velocity distribution is very broad and some of them will be transmitted.

5.1.3 Angle and drift correction of A/Q

In Chapter 4 equation (4.9) shows the calculation of the A/Q ratio. Due to the angle spread of each ion at the final focal plane, the angle correction is essential to improve the separation of the isotopes in the identification plots presented in the following section. The angle of the incoming ion at S4 was measured with the two Time Projection Chambers (TPC). The plot on the left of figure 5.6 shows A/Q from Multi-Hit Time-to-Digital Converter (MHTDC) versus uncorrected angle at S4, on the right side of figure 5.6 shows A/Q versus corrected angle at S4. It was noticed that during the course of the experiment that the mass-to-charge

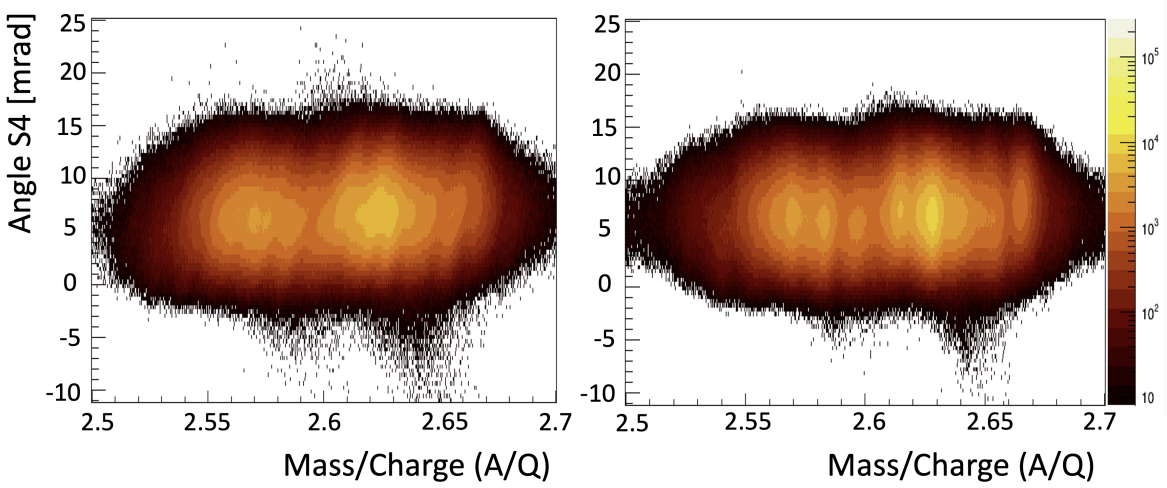

Figure 5.6: Left: uncorrected angle versus A/Q at S4. Right: corrected angle versus A/Q at S4.

value drifted. A final correction of this drift was implemented run by run. Figure 5.7 shows the drift corrected A/Q ratio in time.

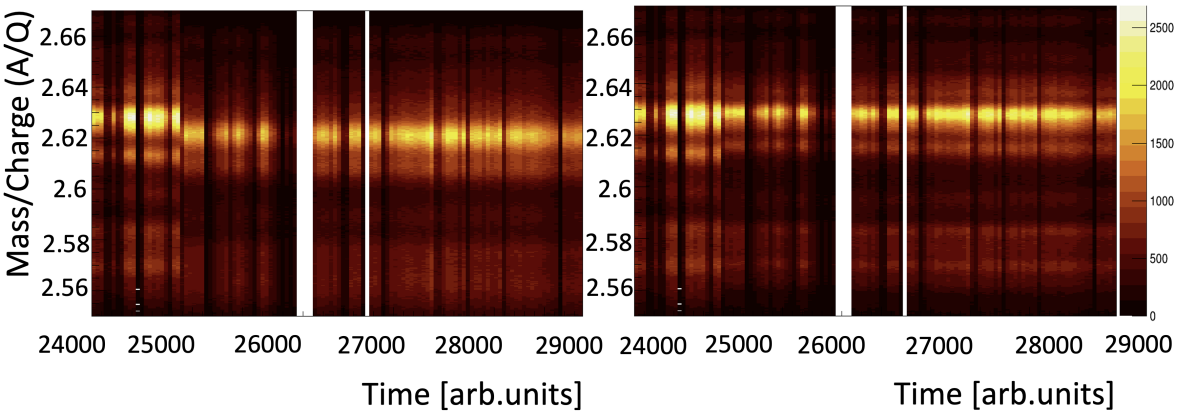

Figure 5.7: Mass-to-charge ratio drift correction in time. Left: Before drift correction, Right: After drift correction

5.1.4 Isotope Selection

The calibration of the ToF and MUSIC detector, and also angle correction in the focal planes, A/Q drift correction, and $Z1$-$Z2$ drift correction provide the final Particle IDentification (PID) plot from the FRS. The PID plot was generated by calculating the atomic number, Z, and the mass-to-charge ratio, A/Q, of each fragment from the measured ToF (velocity), energy loss (ΔE) and $B\rho$ values. The Z value determination and A/Q measurement are explained in detail in Chapter 4.

Figure 5.8 shows the final $Z1$ value from MUSIC1 as a function of the $Z2$ value from MUSIC2. The histogram was obtained after MUSIC calibration and drift correction for both detectors at S4. The boomerang shapes seen in Figure 5.8 are explained by the ionisation of the incoming ion in the gas. Indeed for those elements at the energy of the experiment, the ions have roughly 10 to 15% probability to capture an electron while passing through the gas of the MUSIC [111, 112]. A Nobium stripper is present between both MUSICs to fully ionize the ion.

Figure 5.9 represents the final two-dimensional PID plot of $Z1$ versus A/Q plot for fully stripped ($Z = Qe$) ions after calibration and correction processes were performed. The small tail towards the lower Z present in the spectrum comes from some of the ions capturing an electron during their passage through the MUSICs (see the explanation of Figure 5.8). The PID was confirmed by detecting γ rays emitted following isomeric decay in ^{188}Ta [2] (see Chapter 6). Isotopes that are mainly implanted are selected by choosing the corresponding A/Q. The black circle represents ^{190}W, which will be presented in the lifetime analysis in Chapter 7.

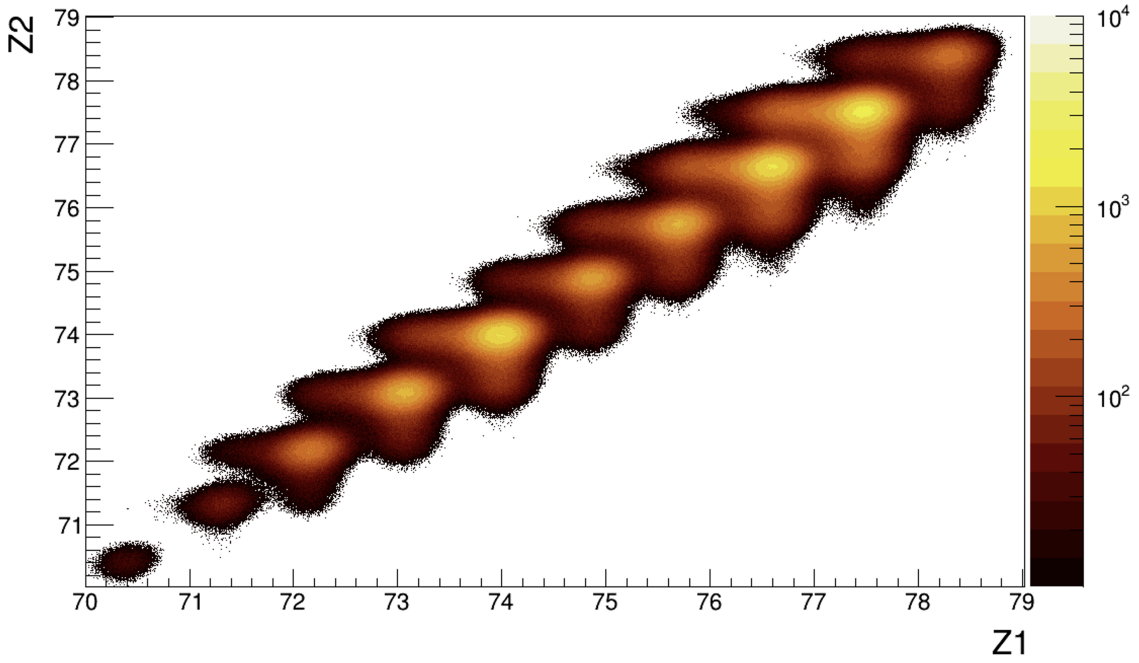

Figure 5.8: The $Z1$ and $Z2$ information extracted from the two ionisation chambers placed at S4.

Figure 5.10 shows the correlation of fragments between their position at S2 and their corresponding Z value. The TPC detectors provide position information at both S2 and S4. Figure 5.11 displays the position of X4 at S4 versus A/Q for the W isotopes observed in the experiment. As previously mentioned, ions have the potential to capture an electron while passing through matter and this can happen with the matter at S2 (plastics, degrader...). In this case a $^{190}W^{73+}_{116}$ would be transmitted between S2 and S4 instead of $^{190}W^{74+}_{116}$, this means the mass to charge ration would be different (2.603 in-lieu of 2.568) and the position would be slightly different. The W isotopes would still, due to electron stripping in the vacuum windows or Nobium foils, be identified as W isotopes in the MUSICs. The shadow blobs in Figure 5.11 are then W^{73+} transmitted in the second part of the FRS, the main blobs being W^{74+}.

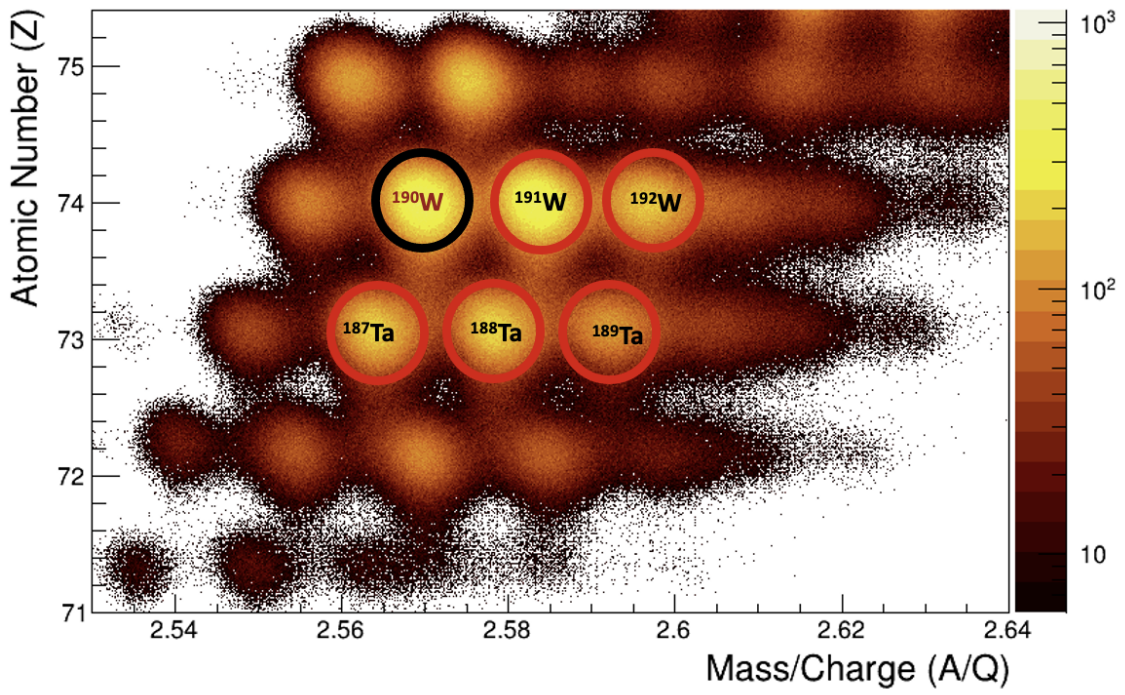

Figure 5.9: Particle Identification plot (atomic number Z versus mass-to-charge ratio) for the FRS setting centered on ^{188}Ta. Nuclei are highlighted with circles to provide a reference.

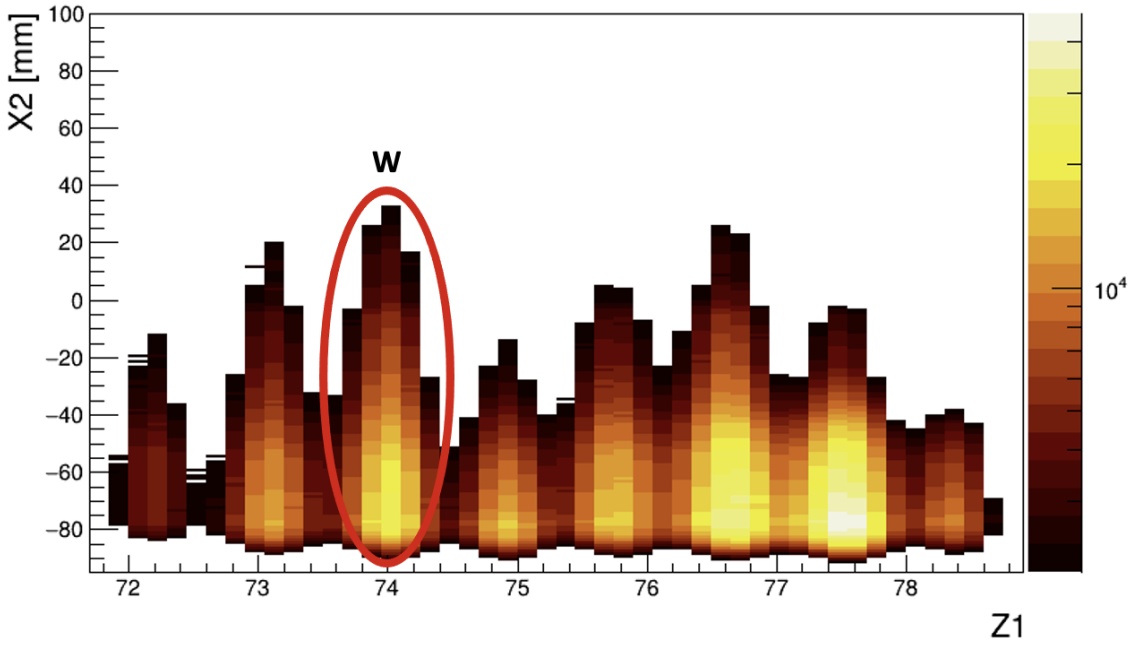

Figure 5.10: X2 position information of fragments from the S2 focal plane versus $Z1$ value from the ionisation chamber. The condition shown in red selects W isotopes with $Z = 74$.

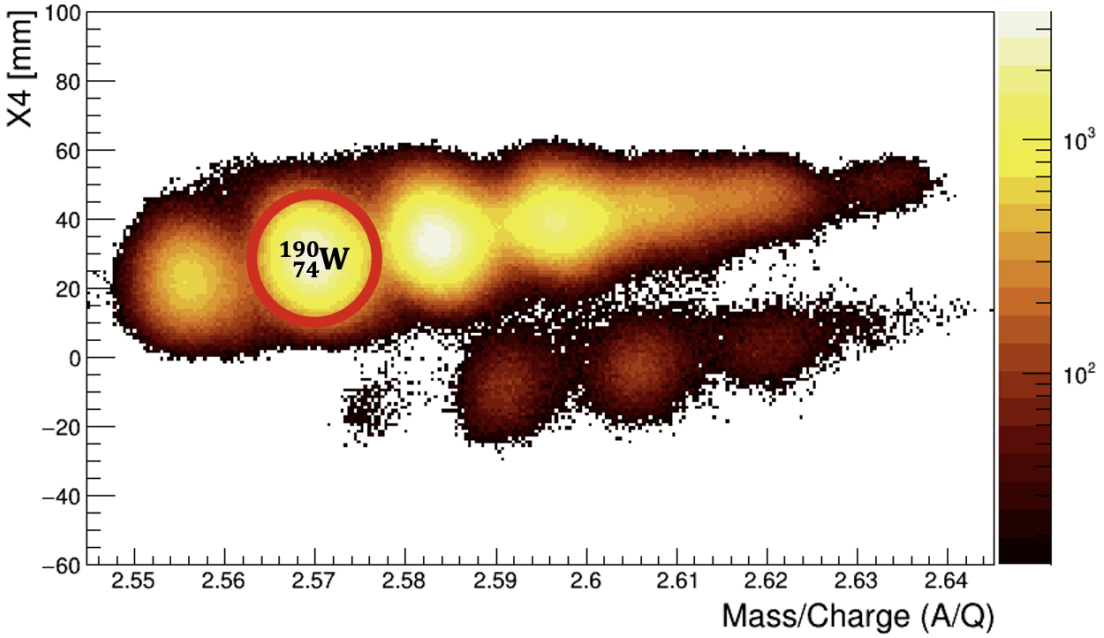

Figure 5.11: $Z1 - Z2$ tungsten isotopes gated, X4 position at S4 with respect to A/Q ratio. The red circle represents $^{190}_{74}W_{116}$ isotope for the further analysis procedure. Please refer to the text for more details)

.

5.2 Calibrations and corrections of the DESPEC experimental setup

In order to perform decay spectroscopy, calibrations and corrections were applied to the DESPEC experimental setup for the detection of γ rays. Therefore, both ^{152}Eu and ^{60}Co source data were recorded before and after the experiment to perform the necessary steps for the calibration and correction of the detectors at S4.

5.2.1 EUROBALL Cluster Energy Calibration

A calibration is needed to determine the energy of the γ-ray emissions in the spectrum. The energy calibration for the EUROBALL cluster was carried out using ^{152}Eu source. The third degree of the equation (5.3) was used to calibrate the HPGe detectors.

$$E_i = \sum_n a_n c_i^n. \tag{5.3}$$

Figure 5.12 shows the calibrated ^{152}Eu energy histogram from EUROBALL. Figure 5.13 represents the resolution of the detector with 0.5 keV binning per channel for the low energy and high energy of the ^{152}Eu source. The full width at half maximum (FWHM) was calculated using FWHM = 2.35 x σ, where σ is the standard deviation of the peak obtained by fitting it with a Gaussian function.

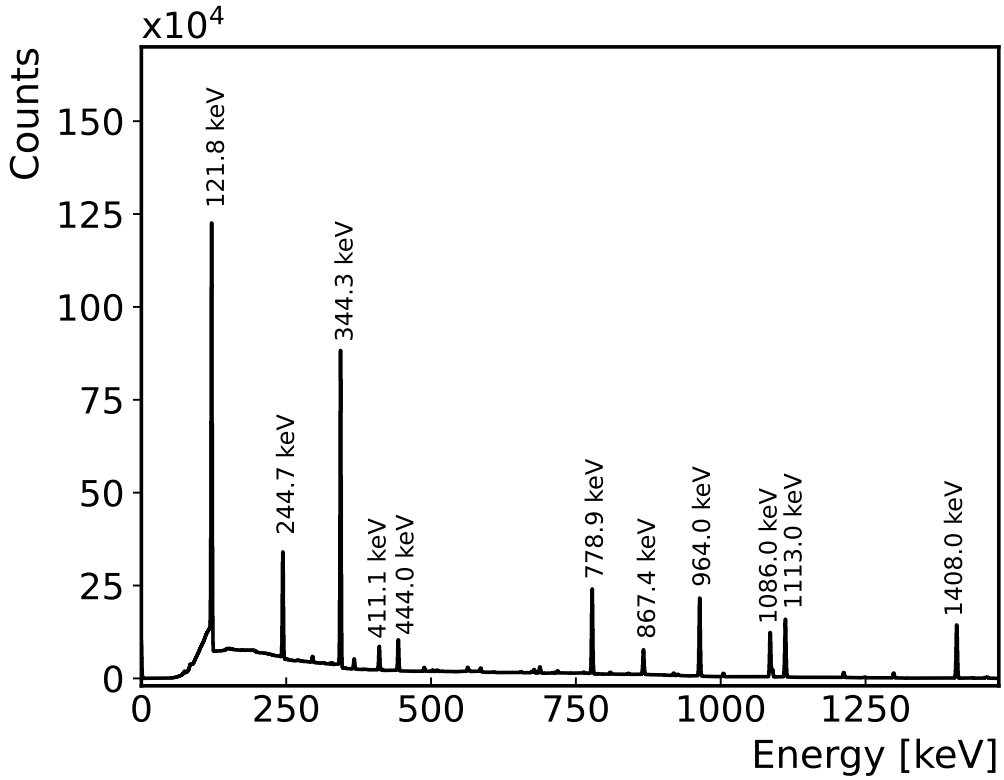

Figure 5.12: EUROBALL ^{152}Eu energy calibrated γ-ray histogram from one of the EUROBALL detectors.

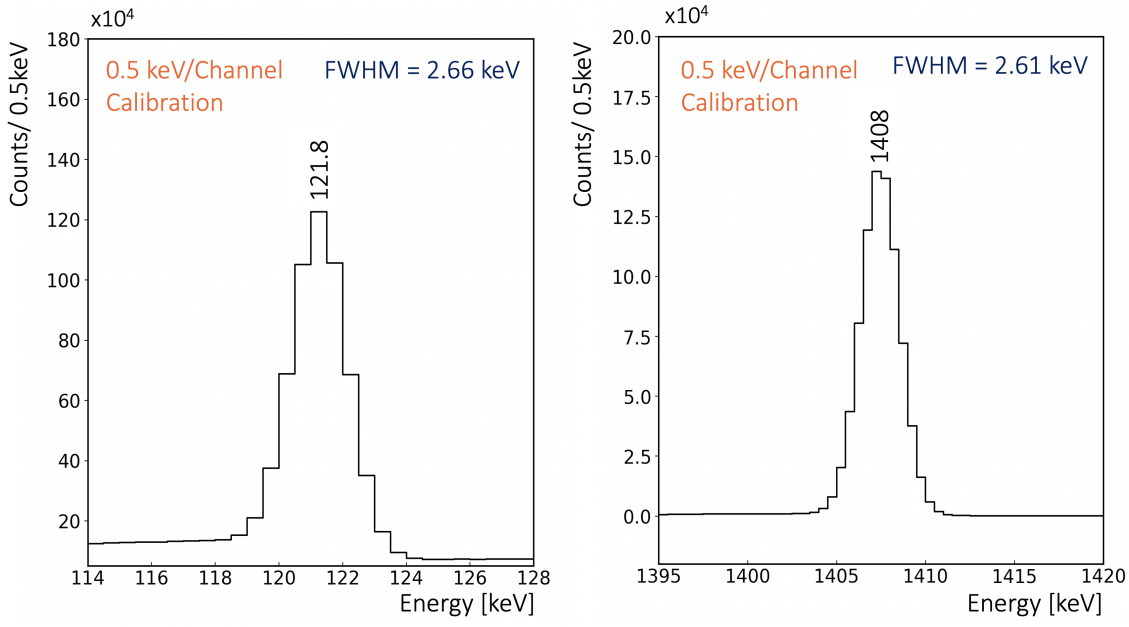

Figure 5.13: Calibrated energy spectrum of ^{152}Eu for lower energy 121.8 keV and higher energy 1408 keV 0.5 keV per channel calibration.

Time Alignment

Accurate time alignment is important to perform lifetime analysis, thus, the TDC signals from pairs of $LaBr_3(Ce)$ detectors were aligned using a ^{60}Co source. To perform time alignment, the maximum peak of the signals from $LaBr_3(Ce)$ detectors is shifted to 0. For instance, Figure 5.14 provides an example of how the time alignment was performed for four $LaBr_3(Ce)$ detectors, with a reference TDC time signal.

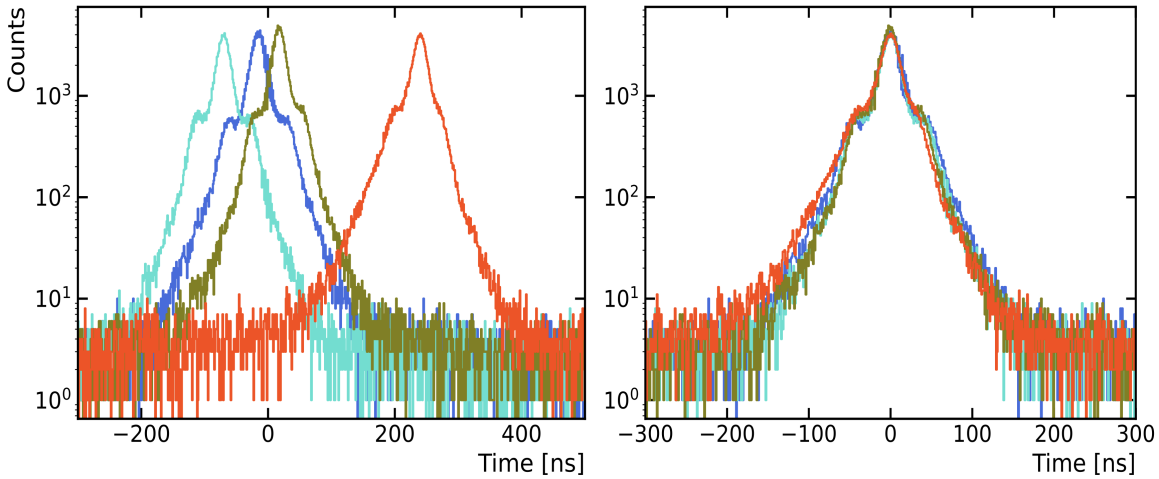

Figure 5.14: Representative time alignment for four $LaBr_3(Ce)$ detector pairs, with a reference detector. The right side shows the TDC signal before time alignment, while the left side shows the TDC signal after time alignment.

Time-walk calibration

As outlined in Chapter 3, the Prompt Response Difference (PRD) describes the linearly combined $\gamma - \gamma$ zero-time response of the two detector timing systems. The time walk refers to the energy-dependent time pick-off of a pulse in an acquisition system. When performing a lifetime measurement using fast-timing techniques, it is important to have accurate information about the energy dependence of the time walk.

The overall prompt time response as a function of energy is described with the prompt response difference curve. PRD curve is a useful method for eliminating the asymmetry between the delayed $C_d(P)(E_{feeder}, E_{decay)}$ and anti-delayed $C_a(P)(E_{decay}, E_{feeder})$ curves. This curve describes the time walk from both branches. To create a PRD curve for a fast-timing experiment, the first step is to establish a fixed gate for feeder and decay transitions in a specific state, while setting the conditions for the coincident transitions of different energies. This PRD was generated by using ^{152}Eu source in the energy range of 244 keV to 1.4 MeV in the current analysis. ^{152}Eu source has two decaying branches, one is to ^{152}Sm via the electron capture and the other one is to ^{152}Gd via β-decay [110].

Figure 5.15 shows the partial level scheme of ^{152}Gd and ^{152}Sm used to build the PRD curve with the most relevant γ-rays that are in coincidence with 344 keV ($2^+ \rightarrow 0^+$) transition in ^{152}Gd and 244 keV ($4^+ \rightarrow 2^+$) in ^{152}Sm. The reference transitions are shown in orange and the coincident γ-rays used to construct the PRD curve are shown in blue (Figure 5.15).

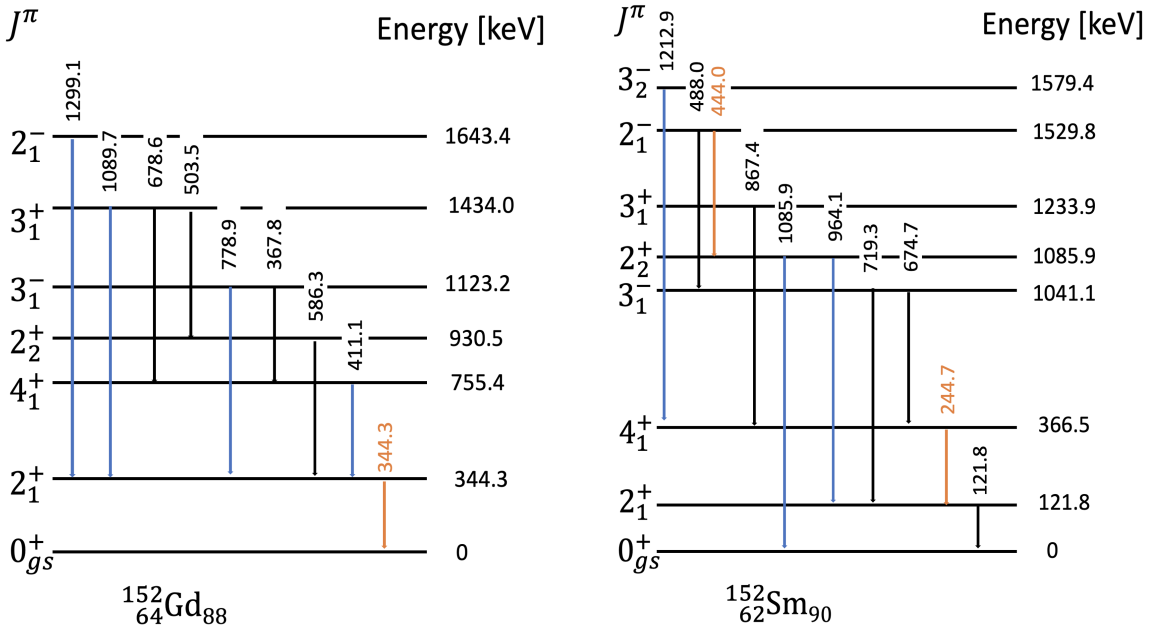

Figure 5.15: Partial level scheme of ^{152}Gd and ^{152}Sm

The coincident transitions of 444 and 488 keV do not directly feed the 366.5 keV state. Instead, they de-excite short-lived levels with lifetimes less than 1 ps, thus their contribution to the time distribution is negligible. The PRD fit residuum from the calibration with the fit function is given by Equation (3.10).

By using the PRD curve the time difference between delays of each detector combination was corrected by the lifetimes of the levels in ^{152}Sm and ^{152}Gd. Figure (a) shows the centroid time difference of the strong 779 keV - 344 keV cascade in ^{152}Eu and then shifting all distributions to a reference position. Consequently, the PRD data points were fitted using the function (3.10) as shown in Figure (b). The estimated uncertainty of the PRD calibration was measured 10 ps.

Energy Calibration

The $LaBr_3$(Ce) detectors have a higher degree of non-linearity in their energy response than the HPGe detectors, which means that their energy calibration needs to be performed in more steps. Firstly, a calibration source is used for an initial energy calibration, followed by a gain matching procedure using known γ-ray transitions of the calibration source. The energy calibration of 36 $LaBr_3$(Ce) detectors was performed using a ^{152}Eu source, and the calibrated gamma-ray transitions of ^{152}Eu are shown in Figure 5.17. The fourth degree of the equation (5.3) was used to calibrate the $LaBr_3$(Ce) detectors.

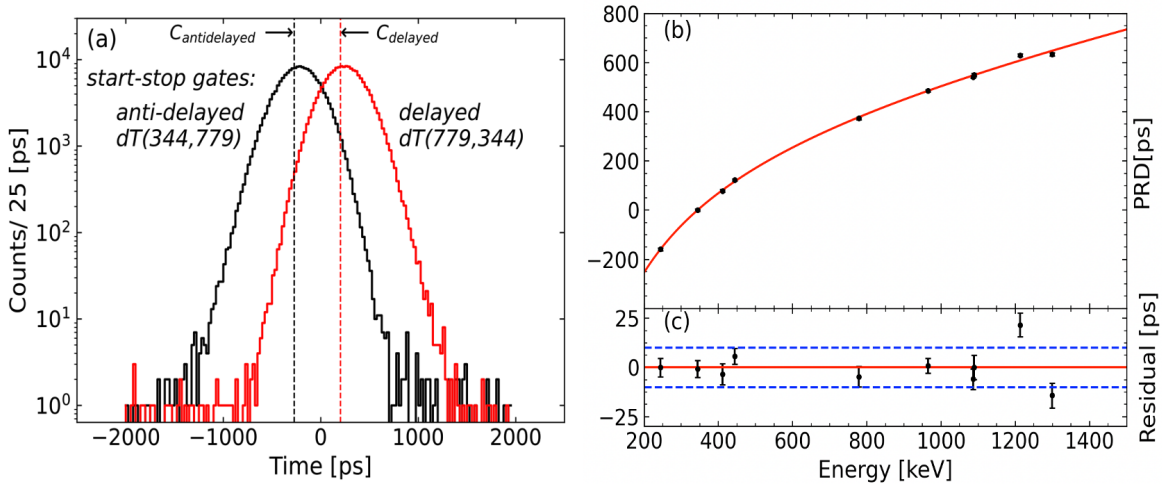

Figure 5.16: (a) The strong delayed and anti-delayed time difference spectra of the 779 $\rightarrow$ 344 keV cascade were obtained by using coincidences with the 344 keV decay transition in ^{152}Gd. (b) The centroid of the 1300 keV - 244 keV coincidence was obtained and corrected for the lifetime of the levels in ^{152}Sm and ^{152}Gd. The fit residual is displayed in the bottom panel (c), dashed lines represent 2σ error-band corresponding to an overall PRD uncertainty. Further details are provided in the text.

Drifts in energy are a common occurrence for $LaBr_3(Ce)$ detectors due to factors such as temperature changes, pulse rate, voltage fluctuations, and intrinsic drift. To address this, the sum peak 1468 keV from ^{138}La was used to perform energy drift calibration on a run-by-run basis. The energy resolution of an HPGe detector is better than that of a $LaBr_3(Ce)$ detector, therefore, the $LaBr_3(Ce)$ detector is not able to distinguish the 1408 keV γ-ray energy of ^{152}Eu from the sum peak of ^{138}La at 1468 keV. Figure 5.18 illustrates the energy drift over time during the experiment and the energy calibration drift.

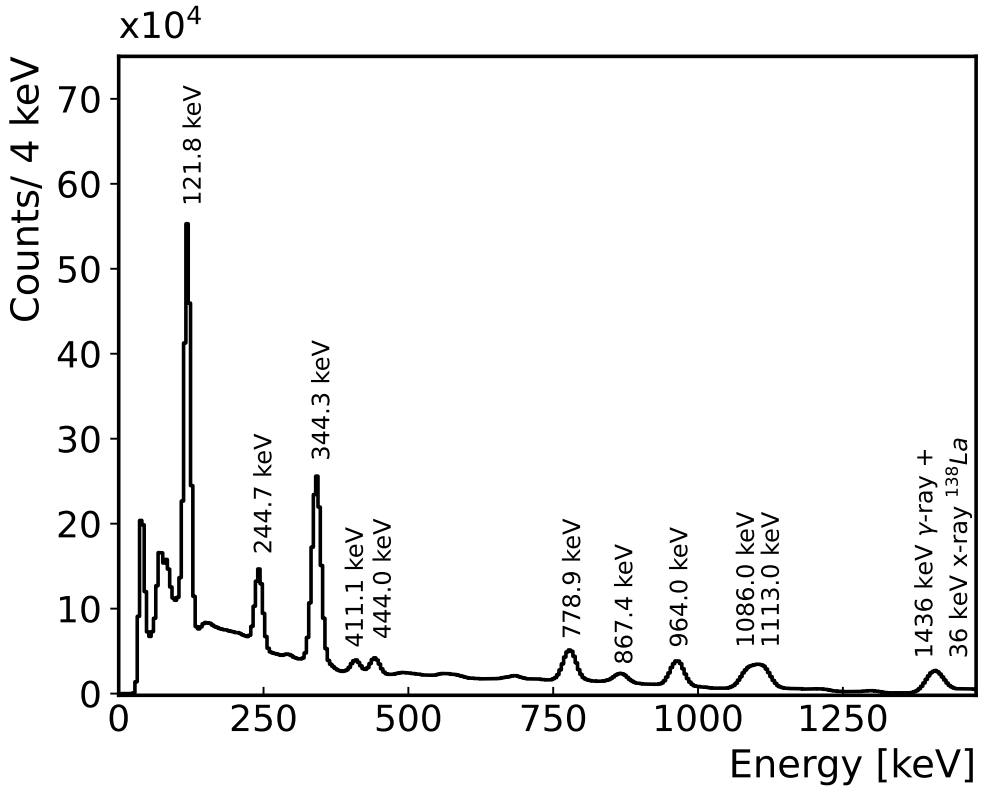

Figure 5.17: FATIMA ^{152}Eu energy calibrated γ-ray histogram from one of the $LaBr_3(Ce)$ detectors.

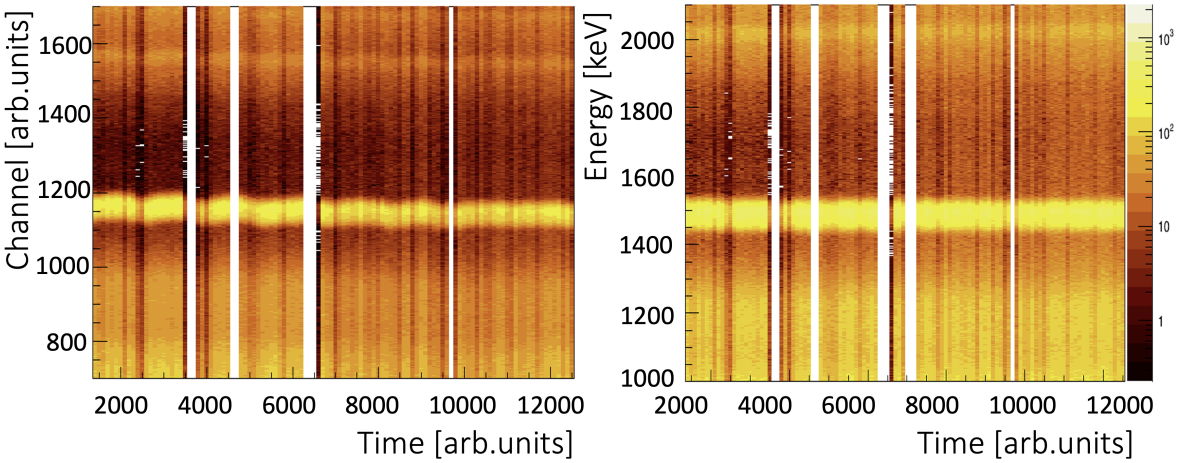

Figure 5.18: On the left is the uncorrected energy drift over time, and on the right is the same drift corrected for the FATIMA array using data from a ^{152}Eu source.

6 Data Analysis

As previously outlined in Chapter 5, a comprehensive calibration and correction process was undertaken following the data collection phase. Once the data was deemed ready for analysis, the appropriate steps were implemented for conducting a lifetime analysis. The purpose of this chapter is to provide a detailed examination of the confirmation of particle identification through the use of ^{188}Ta. This includes identifying the γ transitions and the discussing the isomeric lifetime of ^{190}W. The results of this analysis are presented in the following sections for further review and analysis.

6.1 Confirmation of the Particle IDentification (PID) in the FRS

As previously discussed in Chapter 5, the calibration of the FRS detectors enabled the identification of ions in the FRS. To ensure the accuracy of the particle identification in the experiment, isomeric γ-ray detection was carried out using ^{188}Ta, which was produced through a fragmentation reaction with the primary beam. By selecting the ^{188}Ta ions identified in the FRS, γ rays in coincidence could be identified from both the FATIMA array and the EUROBALL 7-fold germanium clusters (EB), allowing for the extraction of the isomer that depopulates via a 292 keV γ-ray transition. The energy of the 292 keV γ-ray transition of ^{188}Ta was identified in the study [113, 115].

EUROBALL

Figure 6.1 illustrates the gamma energy of ^{188}Ta nuclei in relation to the time difference measured between EUROBALL and the S4 scintillator in the FRS. The structure seen below 800 ns is referred to as the *"prompt flash peak"*. This peak is a result of stopping processes in the materials close to the detector (Bremsstrahlung) and also from light ions from the FRS. Therefore, this region was excluded and the region where the time distribution of the γ-ray of ^{188}Ta is clearly visible was selected. The projection of the energy axis is presented in Figure 6.2 for further analysis.

FATIMA

The energy versus time matrix between signals from the FATIMA and S4 scintillator was constructed for ^{188}Ta nuclei from the FATIMA array (see Figure 6.3). The projection of

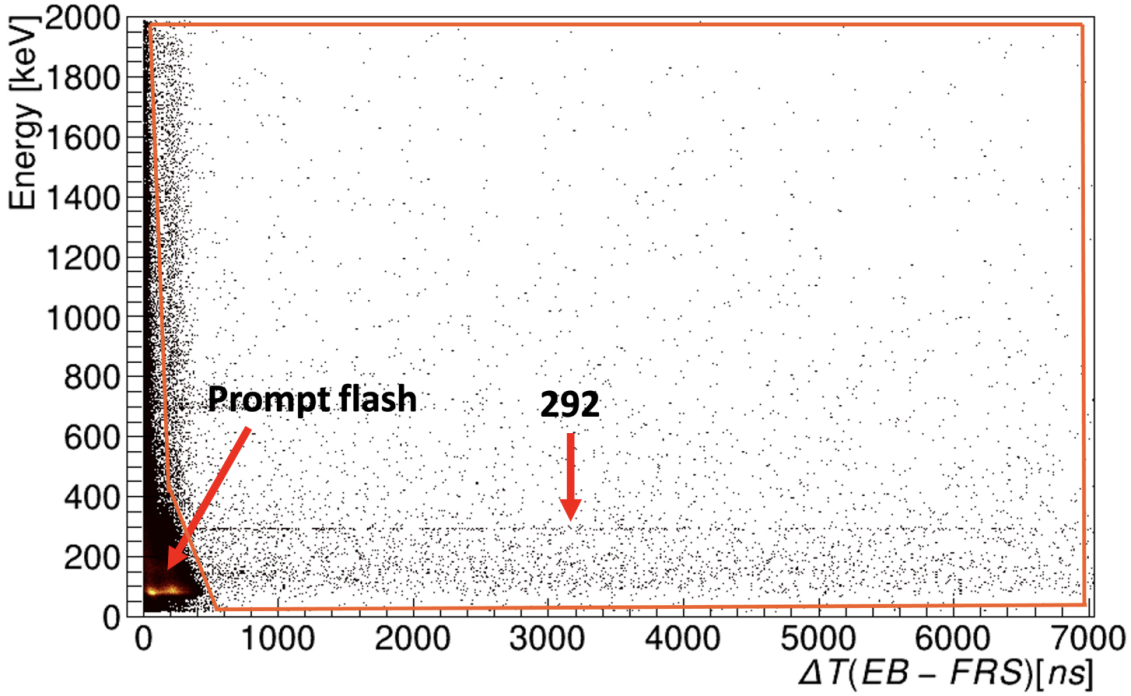

Figure 6.1: Gamma-ray energy versus time difference matrix for ^{188}Ta nuclei from the EUROBALL cluster. The prompt flash corresponds to the Bremsstrahlung events. Time difference between signals from the EUROBALL (EB) and from the S4 scintillator in the FRS.

the energy axis is depicted in Figure 6.4. The isomeric decay of ^{188}Ta nuclei from the FATIMA array was previously reported by Mistry et al. [2] with a measured half-life of $T_{1/2}$=3.1(1) μs, which is in agreement with the value that was cited in a previous study at GSI [115] ($T_{1/2}$=3.7(4) μs).

The study focused on the γ-ray spectroscopy of ^{188}Ta nuclei, with the use of coincidence gating in the FRS to identify its relevant gamma energy from the DESPEC setup. The study was conducted using data obtained from both the FATIMA array and the EUROBALL cluster, and aimed to confirm the final particle identification plot that was obtained from the FRS. The goal of this research was to gain a deeper understanding of the properties of these nuclei, and to verify the accuracy of the particle identification techniques used in the FRS. By combining data from multiple sources allow to increase the robustness of the results and gain a more comprehensive understanding of the γ-ray spectroscopy.

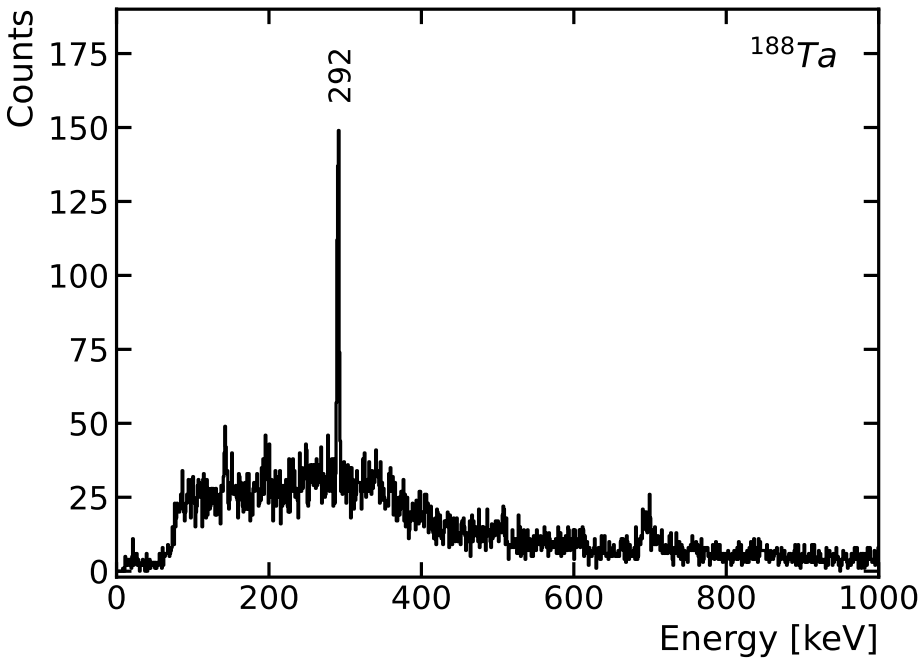

Figure 6.2: Gamma-ray energy projection within a time range of 0-7μs of ^{188}Ta nuclei from the EUROBALL cluster

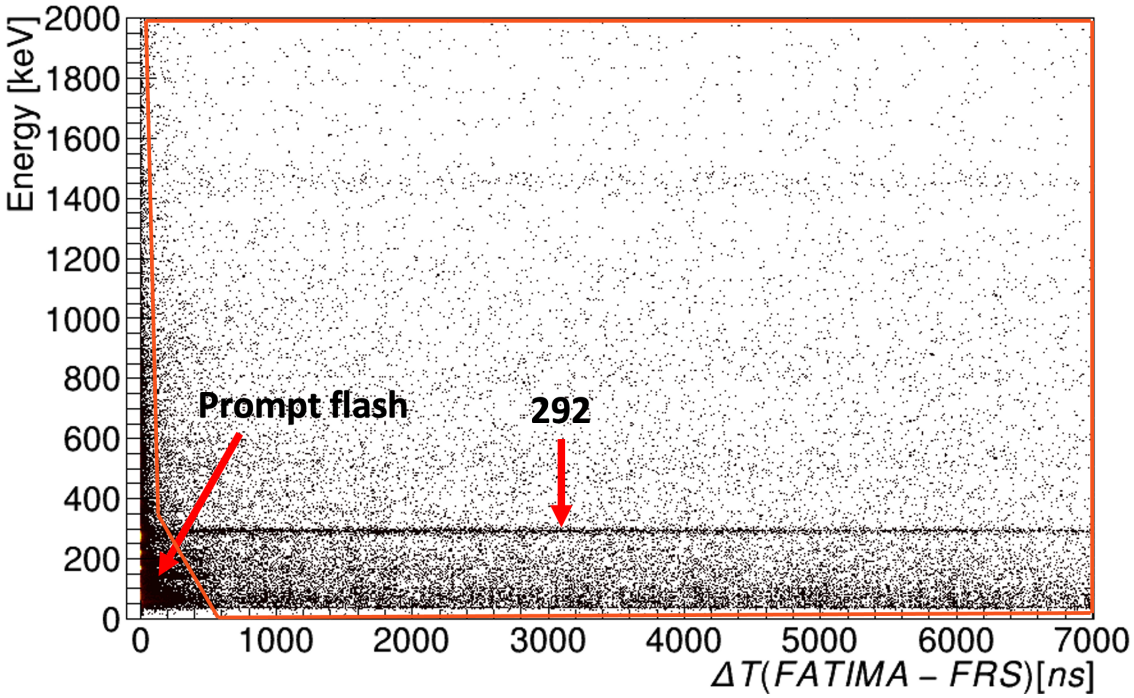

Figure 6.3: Time-γ-ray energy matrix for the isotope ^{188}Ta from the FATIMA array. The prompt flash corresponds to the Bremsstrahlung events.

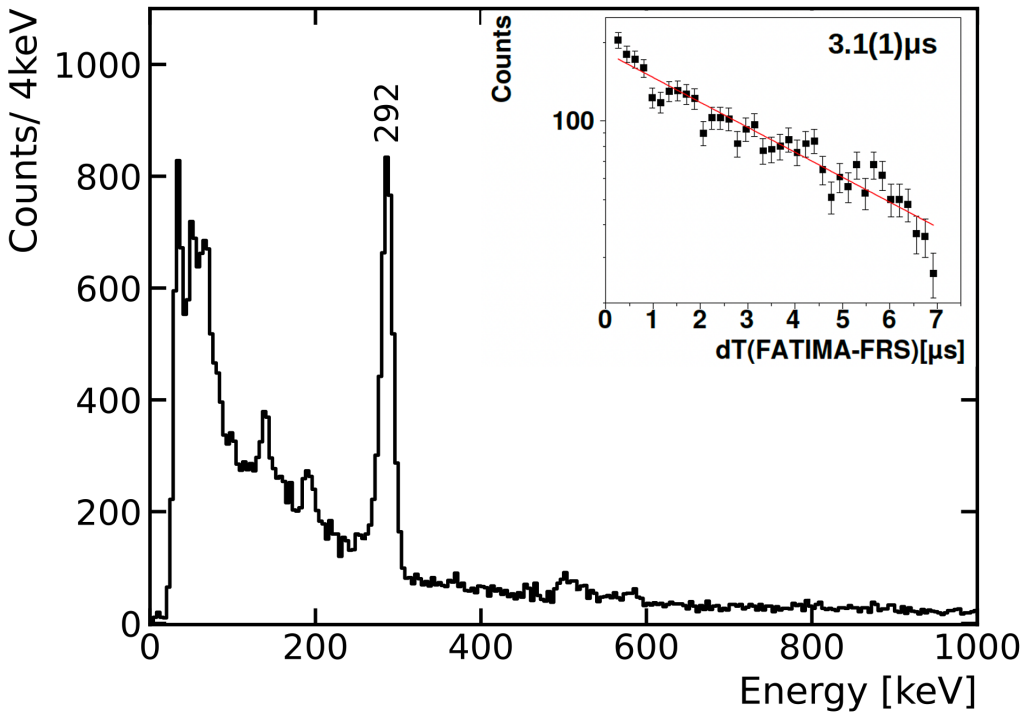

Figure 6.4: Gamma-ray energy projection within a time range of 0-7μs of ^{188}Ta nuclei from the FATIMA array [2].

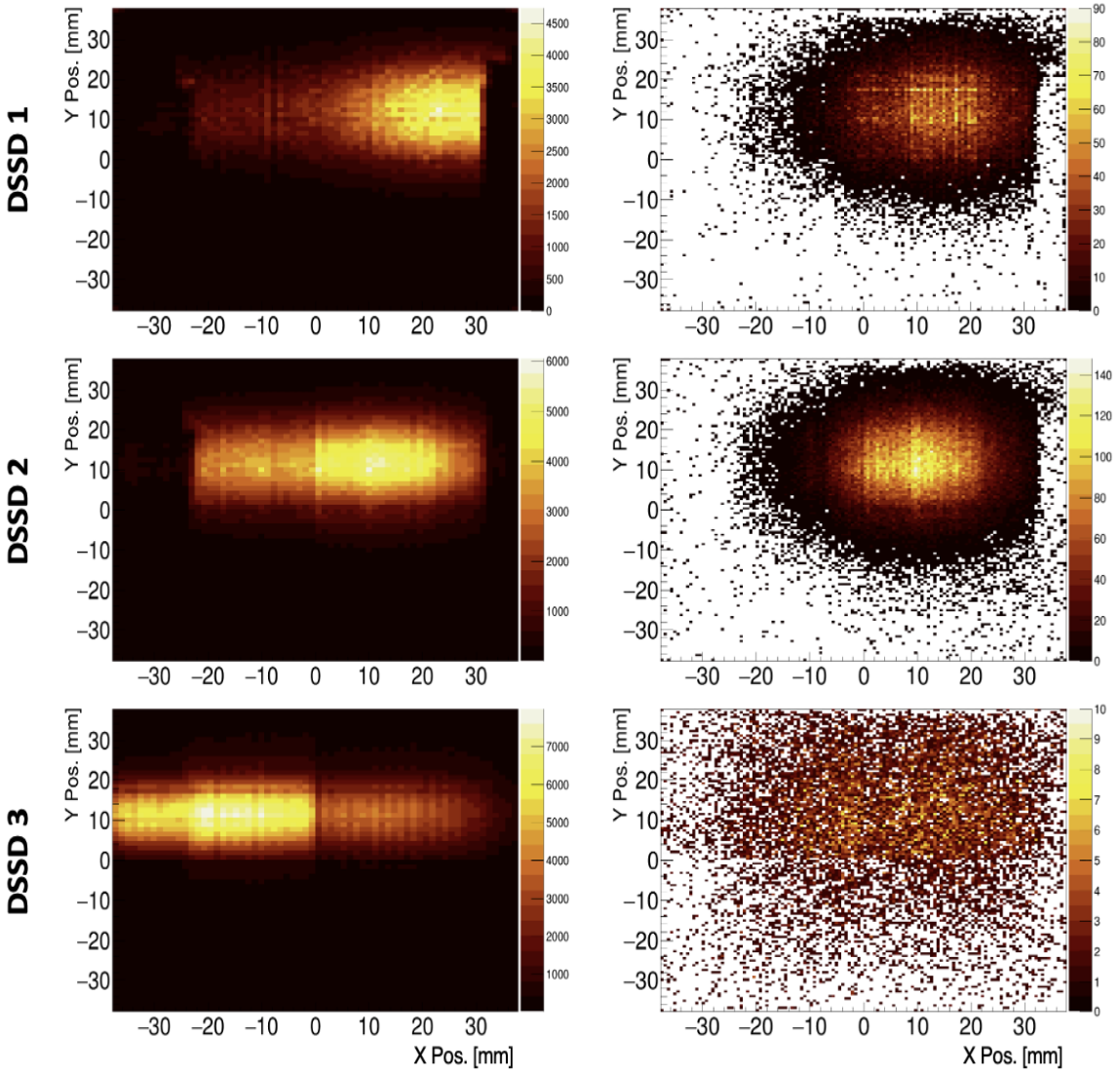

Figure 6.5: Left: All fragments from the FRS stopped in the AIDA DSSD(1-3). Right: show stopped ^{190}W ions in the AIDA DSSD(1-3), respectively.

The primary objective of the AIDA detector is to implant fragments into a single stack of three Double Sided Silicon-Strip Detector (DSSD) units. This is done in order to detect implantation events in a pixel. The aim of the AIDA detector is to identify the implantation event in a pixel, which is done by using a stack of three DSSD units. The use of a single stack of three DSSD units helps in the detection of implantation events in a pixel. An example of the correlation between FRS ions and the AIDA DSSDs from an experiment is illustrated in Figure 6.5. The left histograms in Figure 6.5 display the X and Y positions of the implant

of all the fragments of interest that were stopped in the AIDA DSSDs. The right histograms shows the coincidence between ^{190}W ions in the FRS and the AIDA DSSDs. It can be observed that the majority of the implantation is clearly on the second DSSD for ^{190}W. The conditions on all three DSSDs indicate that ^{190}W ions are correctly implanted into the expected position. This outcome confirms that the AIDA detector is functioning effectively in detecting implantation events in a pixel.

EUROBALL

The fragments that were produced in the FRS were identified on an ion-by-ion basis, which enables the study of excited states that are produced during fragmentation in isomeric states of long-lived excited nuclei. One of the nuclei that were studied in this experiment is $^{190}W_{116}$, which is a neutron-rich nucleus that is four mass units heavier than the most neutron-rich stable tungsten isotope. ^{190}W is known to have an I^{π}= 10^{-} isomer, which has been studied previously in references [116, 117, 115, 118, 113]. In order to investigate the isomeric half-life of ^{190}W, the γ rays that were produced in the reaction were detected using two EUROBALL (EB) HpGe detectors and 36 $LaBr_3$(Ce) detectors. By utilizing these detectors, it was possible to detect the γ rays that were emitted during the decay of the isomeric state in ^{190}W, which provided insight into the properties of this nucleus and the nature of its decay. This information can help to better understand the behaviour of neutron-rich nuclei and the processes that govern their behaviour.

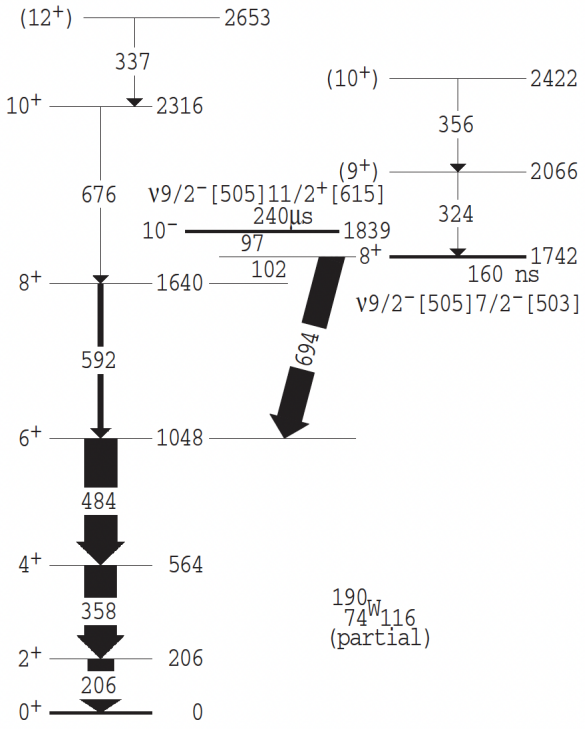

Figure 6.6: Partial level scheme for ^{190}W as reported in reference [116]

To measure the half-life of the isomeric state of ^{190}W from the data obtained by EUROBALL, a two-dimensional matrix was constructed using the energy versus the time dif-

ference (ΔT) between the signals from the EUROBALL detector and the S4 scintillator in the FRS. The data acquisition collection windows were set to be within a range of 0 μs to 2000 μs. To minimize the background noise, the background region was selected to be within a range of 1000 μs $\leq \Delta T \leq$ 2000 μs. The resulting EUROBALL γ-ray spectrum associated with ^{190}W is illustrated in Figure 6.7, while Figure 6.8 shows the background region. These matrices provided a visual representation of the energy versus time differences between the signals, which was used to determine the half-life of the isomeric state of ^{190}W. This approach allowed for the accurate determination of the half-life of the isomeric state of ^{190}W by minimizing the background noise, and thus it provided a more precise measurement of the half-life of the isomeric state of ^{190}W.

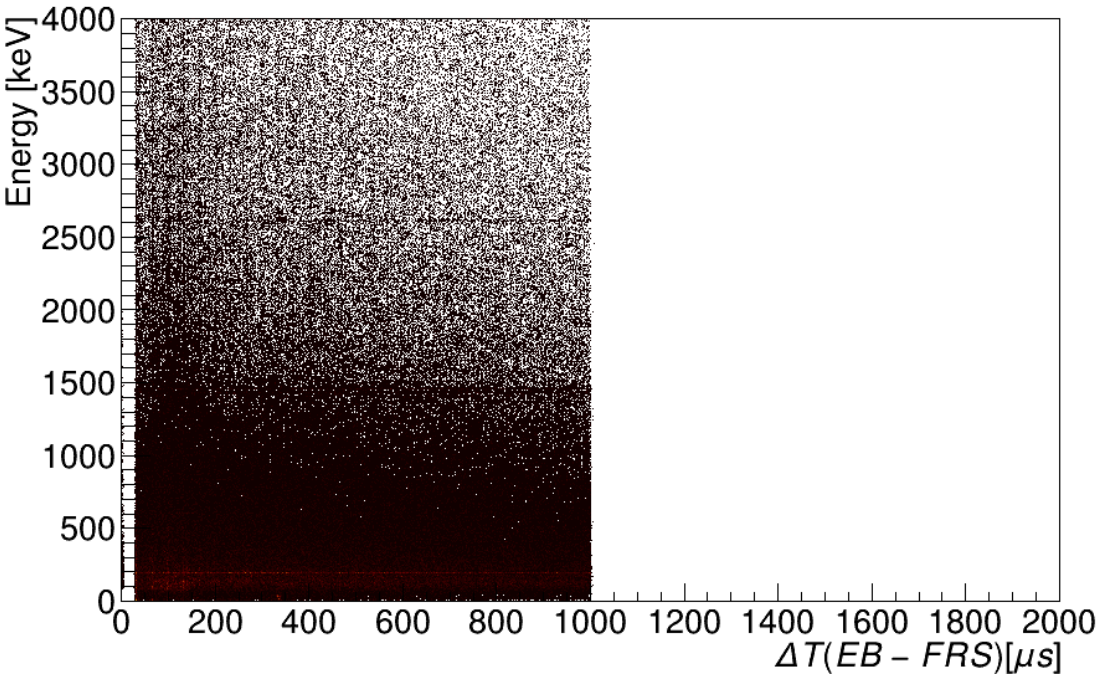

Figure 6.7: Energy vs. time difference between signals from the EB and from the S4 scintillator in the FRS (0 μs $\leq \Delta T \leq$ 1000 μs).

Figure 6.9 shows the histogram of the background subtracted energy versus time difference. It is clear that there is a negative count region between 7 μs $\leq \Delta T \leq$ 30 μs which is identified as the dead time of the MBS DAQ system for the EUROBALL detector. However, an unusual pattern was observed in the histogram. Every 33 μs, an unknown structure appears, which results in a high background, as can be seen in Figure 6.10. Additionally, an unknown structure was also observed around 350 μs. Therefore, in order to eliminate this problem, the lines that appeared every 33 μs (with a width of 1 μs) were removed. Figure 6.11 (c) illustrates the γ-ray background subtracted spectrum of ^{190}W. The isomeric half-

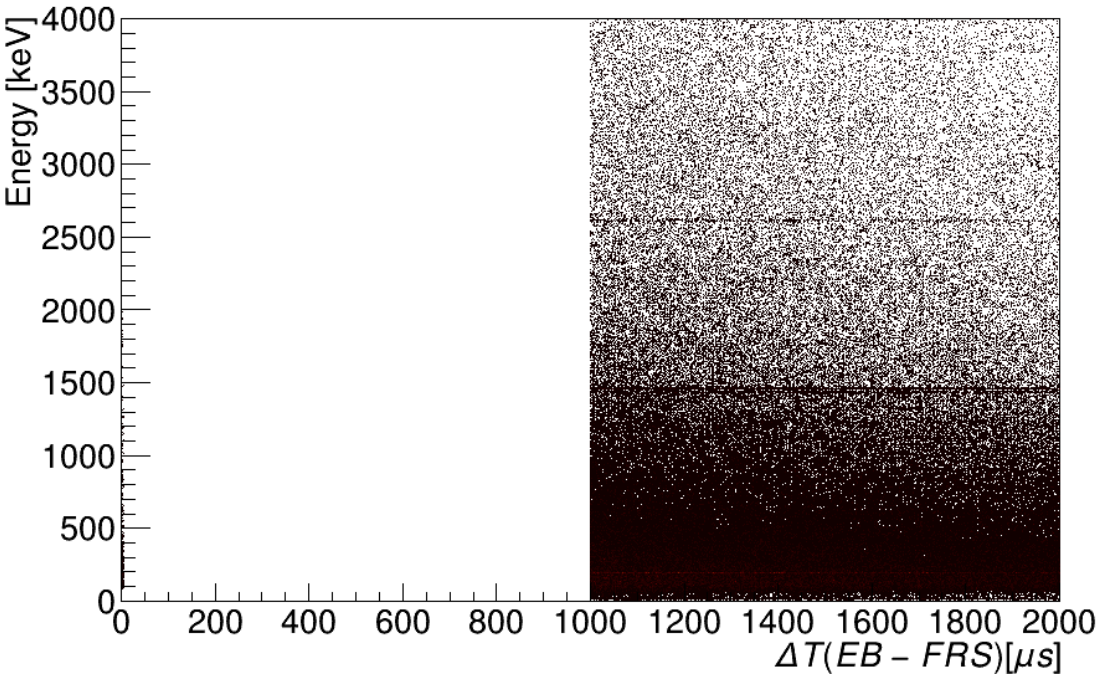

Figure 6.8: Energy vs. time difference between signals from the EB and from the S4 scintillator in the FRS for the background region (1000 μs $\leq \Delta T \leq$ 2000 μs)

life obtained from this measurement is $T_{1/2}$ = 227(83) μs, as extracted using EUROBALL. However, it should be noted that the error value for this measurement is quite high and the obtained value does not agree with the values reported in references [116, 117, 115, 118, 113].

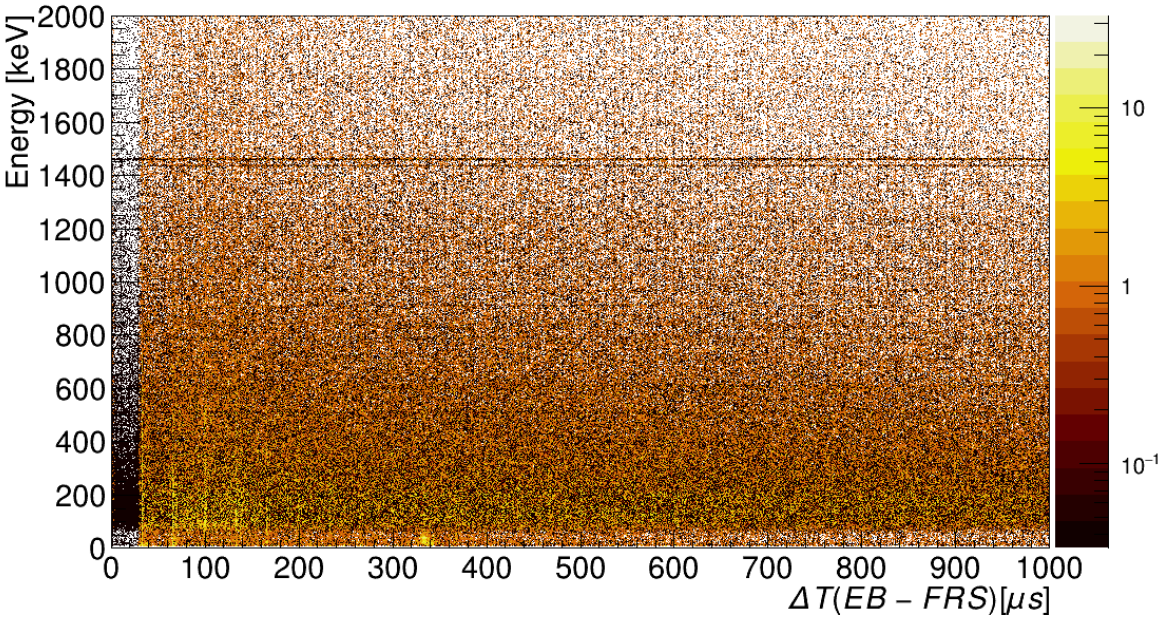

Figure 6.9: Background subtracted energy vs. time difference matrix of ^{190}W

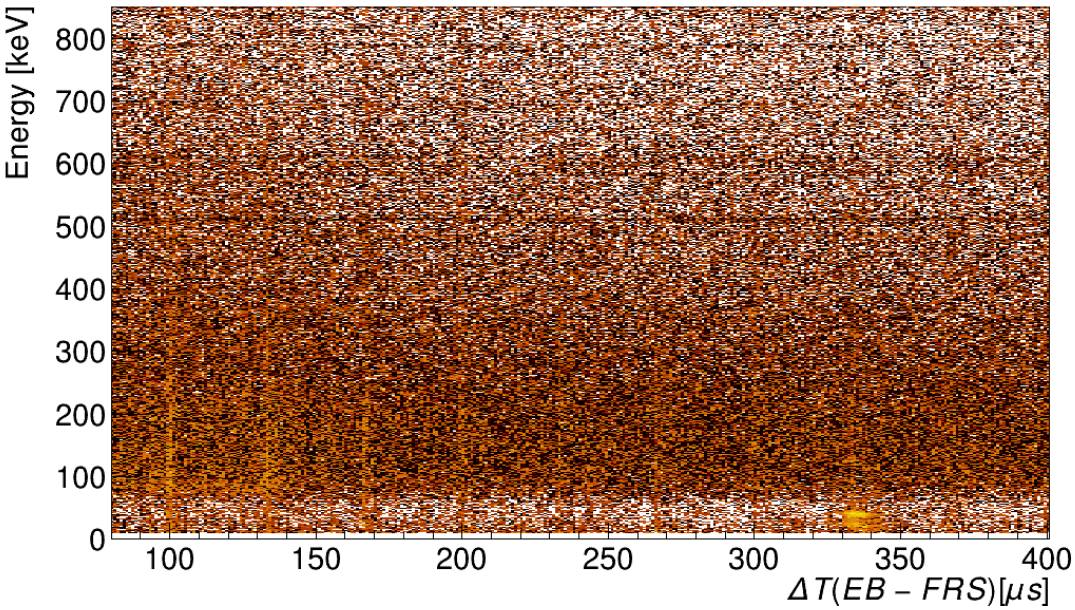

Figure 6.10: Background subtracted energy vs. time difference matrix region 80 μs $\leq \Delta T \leq$ 400 μs (>2 counts/bin for clarity). Every 33 μs unknown structure was observed.

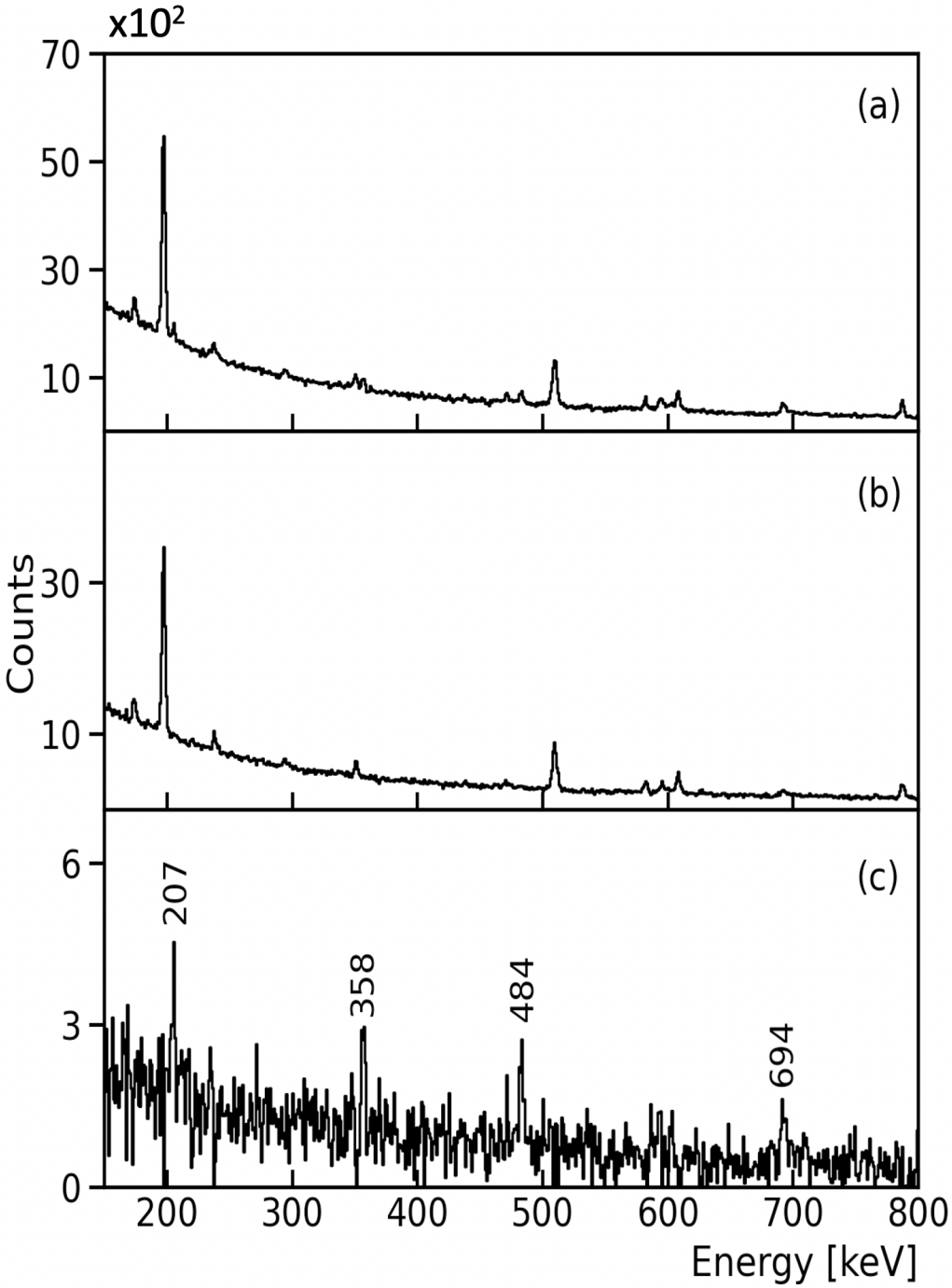

Figure 6.11: (a) EUROBALL γ-ray spectrum associated with ^{190}W in the FRS for a time period 0 μs $\leq \Delta T \leq$ 1000 μs. (b) The background spectrum for a time period 1000 μs $\leq \Delta T \leq$ 2000 μs. (c) γ-ray background subtracted spectrum in EUROBALL of ^{190}W.

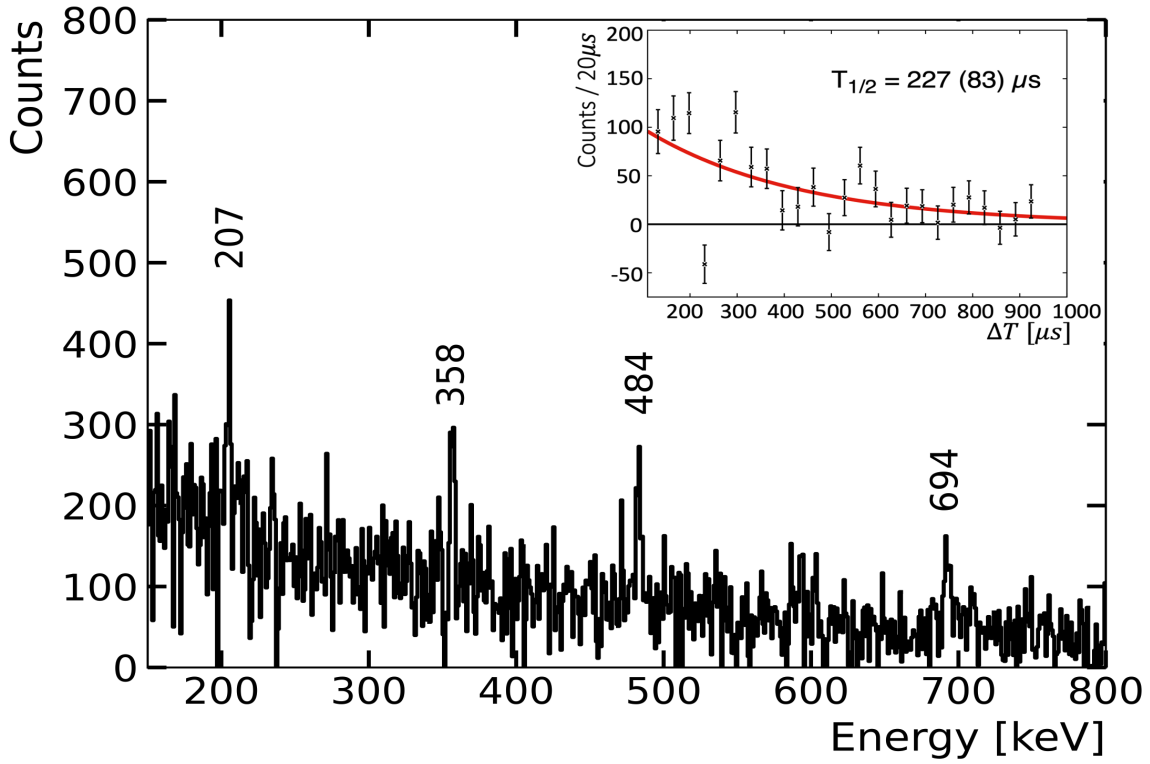

Figure 6.12: EUROBALL γ-ray energy within the time period ΔT(EUROBALL-FRS(^{190}W)) = 0 - 1000 μs, with a normalised background subtraction applied from the time region 1000 μs – 2000 μs. In the inset, the extracted isomeric half-life is 227(83) μs.

FATIMA

The process of determining the isomeric lifetime of ^{190}W was also carried out using the FATIMA detector array. Figure 6.13 presents a matrix displaying the energy versus time from the S4 scintillator in the FRS, with a range of 0 μs $\leq \Delta T \leq$ 1000 μs. Figure 6.14 illustrates the background region, which ranges from 1000 μs $\leq \Delta T \leq$ 2000 μs. Following the subtraction of the background from the FATIMA 2D matrix of the energy versus time, the result is presented in figure 6.15. It is noteworthy that the background subtraction process results in relatively clean and clearly visible transitions of interest. Additionally, it is worth mentioning that the 1431 keV line in FATIMA is a doublet, due to the electron capture decaying ^{138}La $\rightarrow$ ^{138}Ba, which populates an excited 2^+ state and subsequently decays via a 1436 keV γ-ray transition.

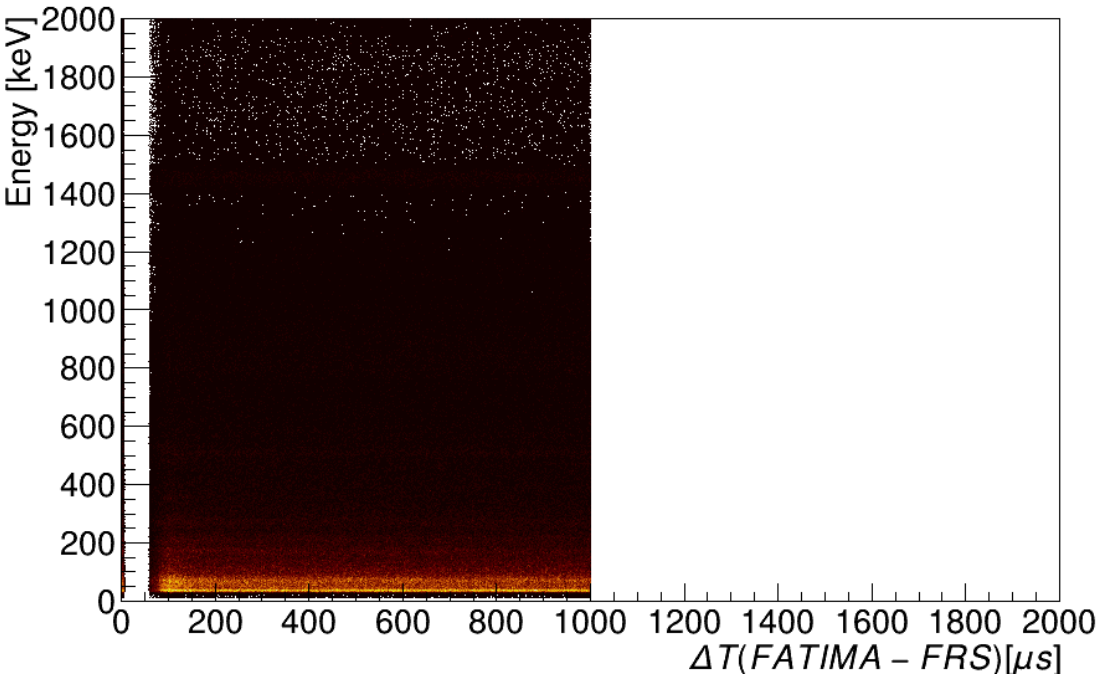

Figure 6.13: Energy vs. time difference between the FATIMA signals and the S4 scintillator in the FRS (0 μs $\leq \Delta T \leq$ 1000 μs).

Figure 6.16 illustrates the FATIMA γ-ray spectrum associated with ^{190}W, while (b) shows the background region. The γ-ray transitions that follow the decay of the 10^- isomeric state are clearly visible in the spectra, as shown in (c). This feature enables us to extract the isomeric half-life of ^{190}W from the data obtained using the FATIMA array. This data is useful for understanding the behaviour of the ^{190}W isomeric state and can aid in further research.

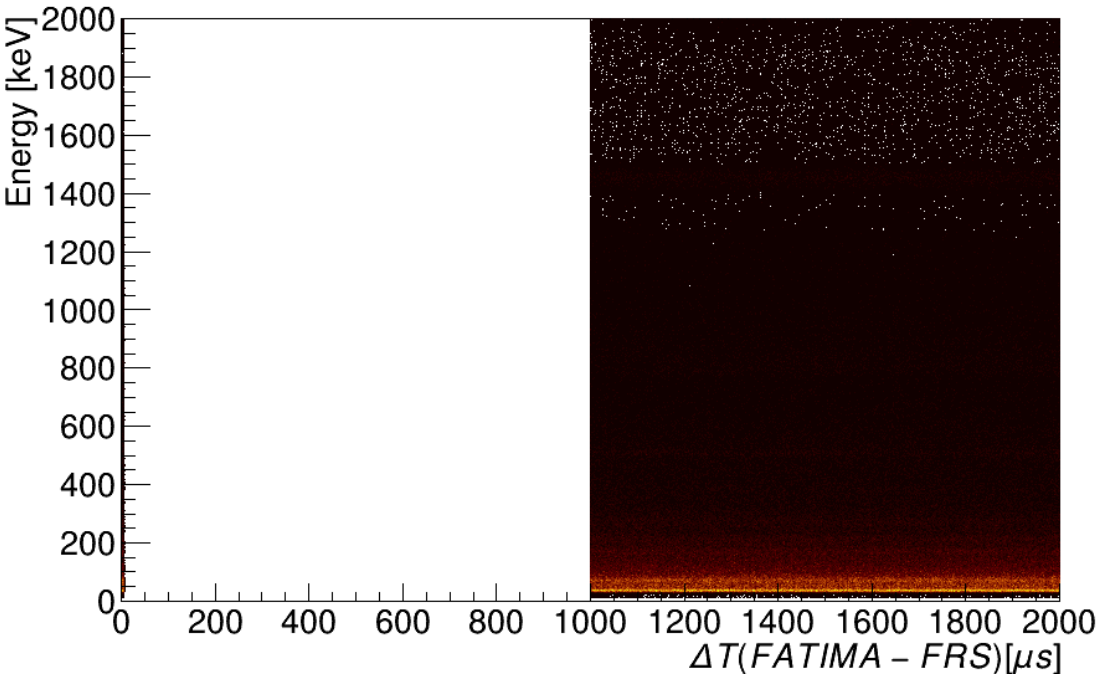

Figure 6.14: Energy vs. time difference between signals from FATIMA and from the S4 scintillator in the FRS for the background region (1000 μs $\leq \Delta T \leq$ 2000 μs)

Figure 6.17 presents the normalised background-subtracted energy projection of ^{190}W, and it is evident that the γ-ray lines corresponding to ^{190}W are clearly visible. It is important to mention that additional background subtraction was performed due to the Compton scattering of the numerous γ-rays produced. This results in the Full-Energy-Peaks (FEP) being obscured by a high Compton continuum of the same energy but a different origin. When energy gates are applied to the FEPs, events correlated with the underlying Compton scattering also appear in coincidence, making the coincident spectra less distinct due to the presence of "deceptive" counts. To eliminate this effect, it's important to correct for this contribution. An effective method to reduce this contribution is by subtracting the events that appear in coincidence with the background beneath the selected FEPs in $LaBr_3$(Ce). Since the background under the peaks cannot be directly measured, it is selected on the right and left side of the FEP by choosing a region with the same number of channels and only contains a background, in order to make the best analysis conditions. The half-life of the decaying isomer was determined by using coincidence gates on the 358 keV, and 484 keV transitions for a time window of 110 μs $\leq \Delta T \leq$ 1000 μs. This time window was deemed optimal based on considerations of both background and the limitations imposed by the deadtime of the electronics system, which allowed us to extract the $T_{1/2}$=127(12) μs half-life from the $LaBr_3$(Ce) array.

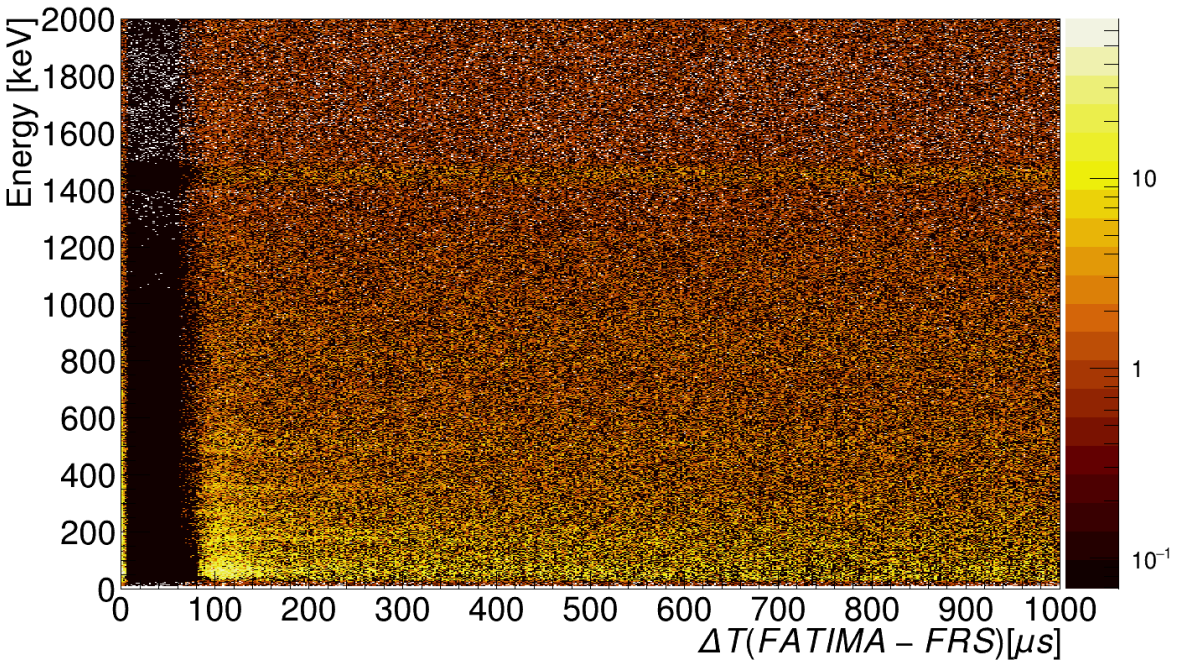

Figure 6.15: Background subtracted energy vs. time difference matrix of ^{190}W

A previous high-resolution γ-ray study performed at GSI found that the $I^{\pi} = 10^{-}$ isomer in ^{190}W [114], originating from a neutron $K^{\pi} = 10^{-}$ $9/2^{-}[505]11/2^{+}[615]$ configuration, had a half-life of $T_{1/2} = 106(18)$ μs [115] at GSI. This half-life value was statistically compatible with the one of $T_{1/2} = 105(22)$ μs from an earlier experiment [118], however, at variance with the value of $T_{1/2} = 167(6)$ μs Ref. [116]. That work revealed that the 10^{-} isomer would not decay via the yrast 8^{+} state, but a longer-lived 160 ns 8^{+} isomeric state only 97 keV below the 10^{-} isomer.

The present isomer lifetime of 127(12) μs rather supports the previous values derived at GSI than the value of Ref. [116]. The latter, however, used a different production mechanism which may have led to different populations of initial states. We further note that due to the long correlation time window of 2 μs and the subtraction of random background in the present lifetime measurement the decay curve shown in Fig. 6.17 clearly approaches zero, which has not been the case in the previous studies, which were limited to a range of few hundred microseconds.

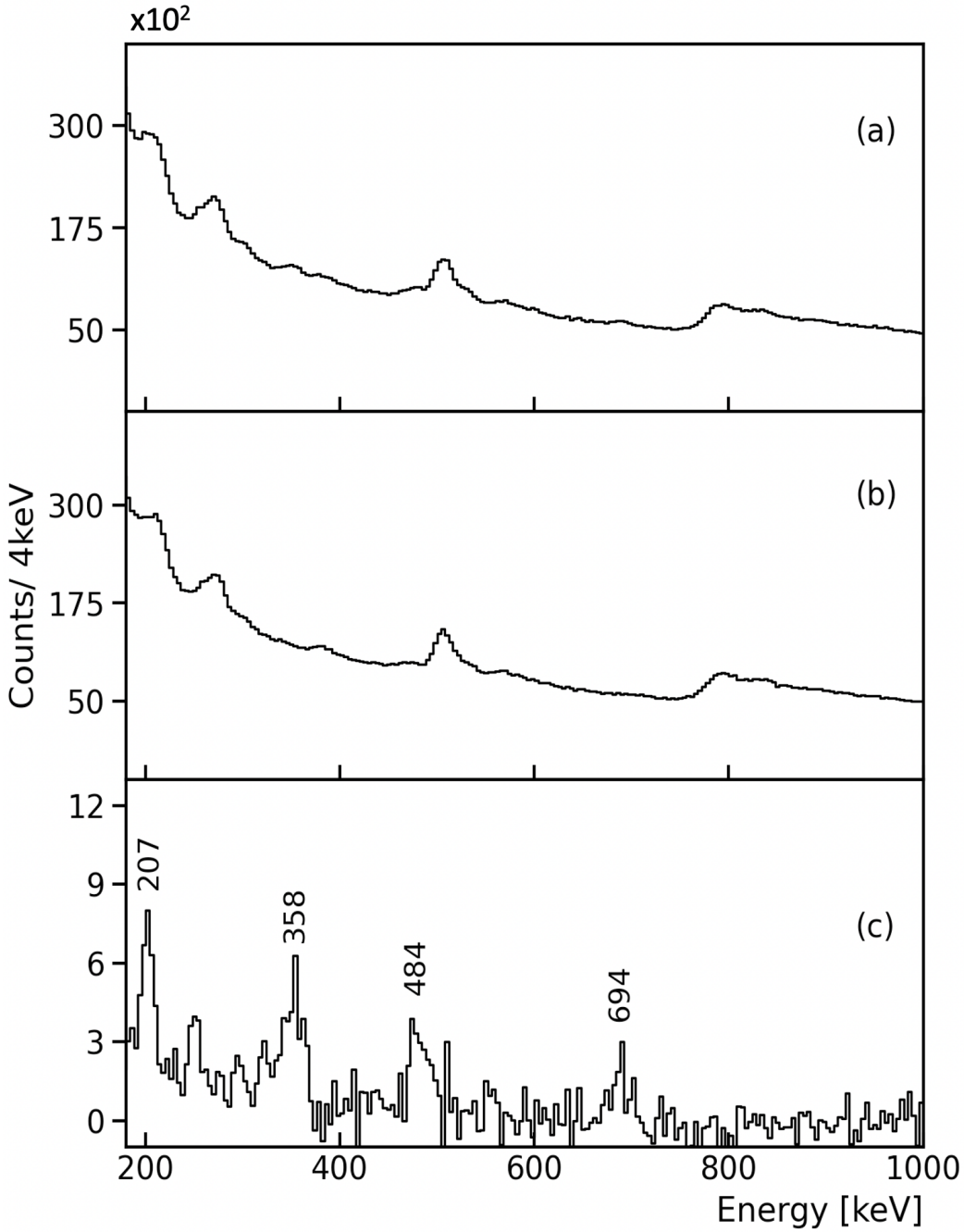

Figure 6.16: (a) FATIMA γ-ray spectrum associated with ^{190}W in the FRS for a time period 0 μs $\leq \Delta T \leq$ 1000 μs. (b) The background spectrum for a time period 1000 μs $\leq \Delta T \leq$ 2000 μs. (c) γ-ray background subtracted spectrum in FATIMA of ^{190}W.

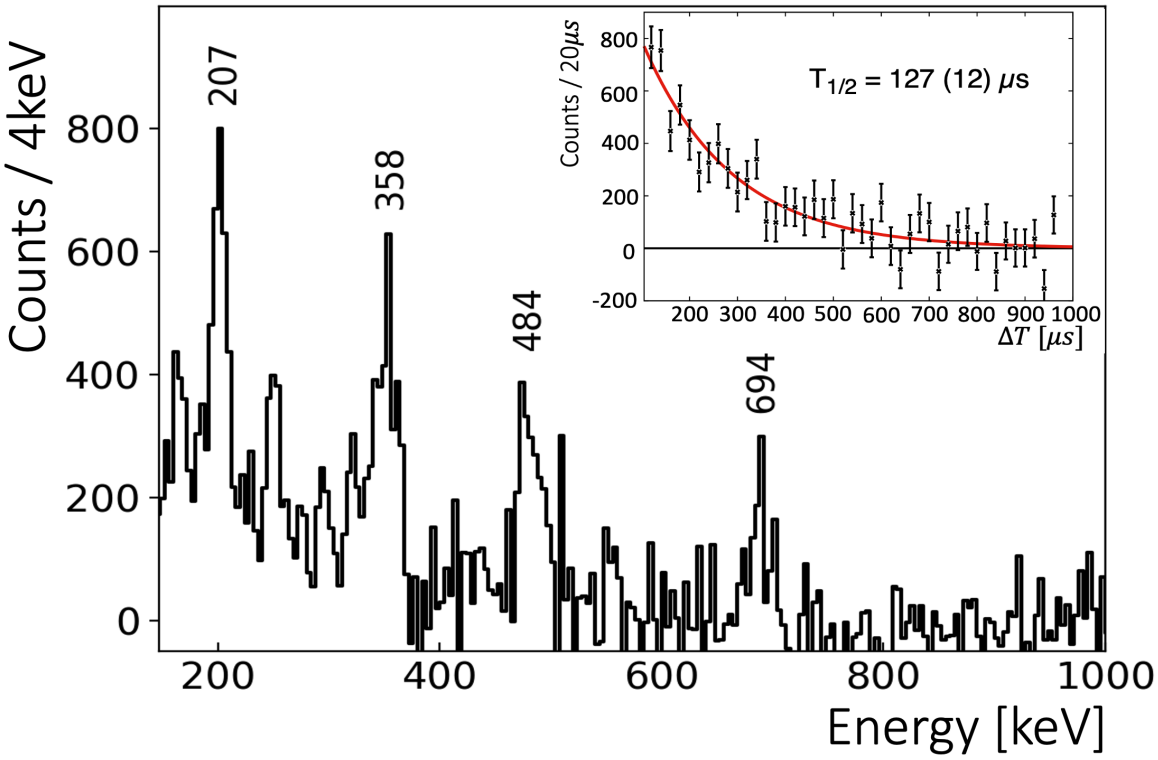

Figure 6.17: FATIMA γ-ray energy within the time period ΔT(FATIMA-FRS(^{190}W)) = 0 - 1000 μs, with a normalised background subtraction applied from the time region 1000 μs – 2000 μs. In the inset, the extracted isomeric half-life is 127(12) μs.

7 Lifetime Determination

The precision of the fast-timing technique used in this work depends on the time resolution of the FATIMA setup. To improve the accuracy of the technique, the time distributions of $LaBr_3$(Ce) detectors were aligned using gamma-ray transitions from a ^{60}Co source, before applying a time walk correction and the subsequent lifetime analysis (details in chapter 5). This chapter presents the lifetime measured in this work using the technique described in the experimental technique chapter. The GCD method was used to extract the half-life of low-lying 2_1^+ state in ^{190}W. The time-walk calibration of the experimental setup for the $LaBr_3$(Ce) array was performed using PRD calculation. For the lifetime analysis, a three-dimensional $E_{\gamma 1} - E_{\gamma 2} - \Delta T$ was built and energy gates were applied to extract the relevant data for the analysis.

7.1 Lifetime of 2_1^+ state of ^{190}W

One of the aims of the experiment is to measure the lifetime of 2_1^+ state for the first time of ^{190}W. After completing all the necessary procedures, including energy calibration, efficiency calibration, time-walk calibration, detector time alignment, and background subtraction, the energy spectra and matrices can be extracted from the data. As mentioned in Chapter 3 the generalised centroid shift method is known as the method of determining the lifetimes of short-lived excited states, which typically last only a few tens of picoseconds. A crucial aspect of the lifetime analysis is the creation of fast-timing matrices. These are three-dimensional objects that store energy information about the $LaBr_3$(Ce) coincidences events. This information includes the γ-ray energies of the transitions that both populate and de-excite a level, as well as the associated time differences in the third axis. To this end, the background-subtracted three-dimensional $E_{\gamma 1} - E_{\gamma 2} - \Delta T$ matrix is used to perform the GCD method. The background region was selected from 1000 μs $\leq \Delta T \leq$ 2000 μs. Additionally, an energy coincidence was applied on the feeder-decay cascade ($E_{\gamma 1}$ - $E_{\gamma 2}$) corresponding to a given state of interest to the $E_{\gamma 1} - E_{\gamma 2} - \Delta T$ matrix. As a result of these steps, the delayed and anti-delayed time difference spectra were generated between a Start and a Stop detector, which were then used for the lifetime analysis.

In experiments like the DESPEC campaign, which involved a substantial number of gamma rays and detectors arranged in close geometry, the chance of a gamma ray un-

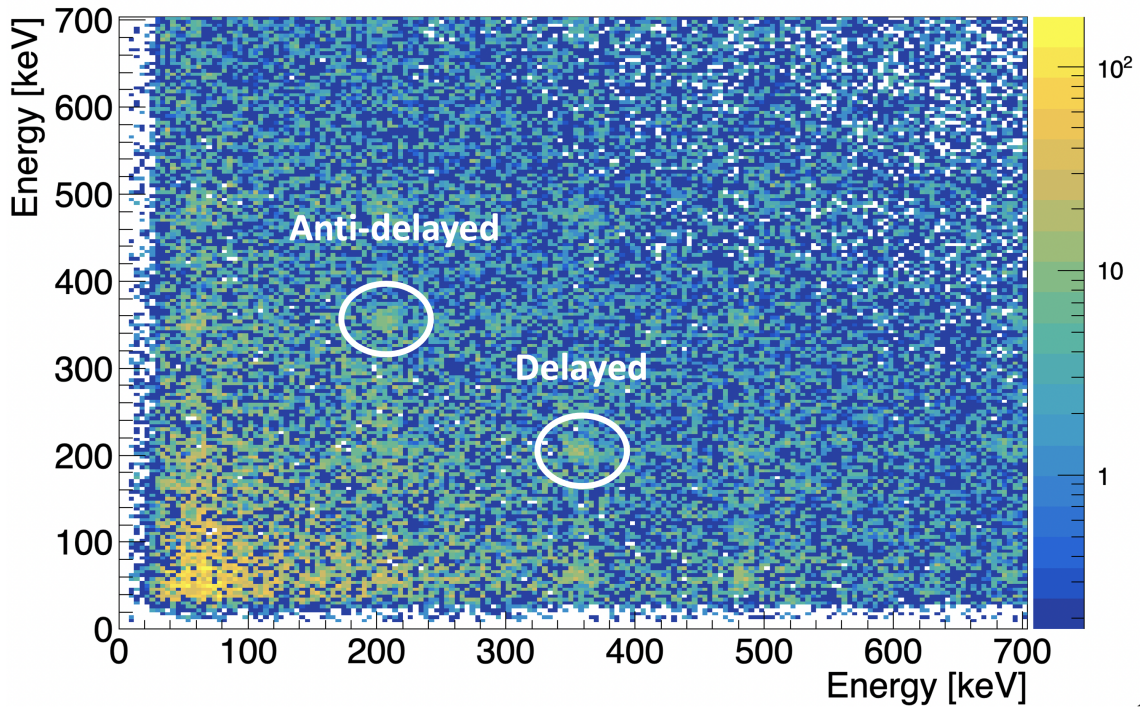

Figure 7.1: Background subtracted $E_{\gamma 1} - E_{\gamma 2}$ projection of the $E_{\gamma 1} - E_{\gamma 2} - \Delta T$ cube. The white encircled areas represent delayed and anti-delayed coincidences. The delayed coincidence involves the detection of a feeding transition (Start) at an energy of $E_{feeder} = 358$ keV ($4_1^+ \rightarrow 2_1^+$), and a decay transition (Stop) energy of $E_{decay} = 207$ keV ($2_1^+ \rightarrow 0_1^+$).

dergoing multiple scattering and losing its full energy before reaching the detector is not insignificant. This results in inter-detector Compton scattering, which generates a substantial amount of background and complicates the proper identification of Full Energy Peaks (FEP). Furthermore, when energy gates are set to select events, the background events are also included, leading to significant alterations in the time distributions, sometimes even completely altering the results. Hence, background subtraction for cube was performed in order to clean the background. The lifetime analysis of the 2_1^+ state in ^{190}W involved the use of a background subtraction method that relied on the assumption that there were no significant time-correlated Compton-background events present under the peak of interest. We could confirm this assumption by observing there was no background during the analysis for underlying the peak of interest.

Figure 7.1 shows the background subtracted $E_{\gamma 1} - E_{\gamma 2}$ projection of the $E_{\gamma 1} - E_{\gamma 2} - \Delta T$ cube. The white circles in the figure indicate separate coincidence instances. The events in the top left circle, referred to as "Anti-delayed," are identified by the $4_1^+ \rightarrow 2_1^+$ transition (358 keV) as the Stop signal and the $2_1^+ \rightarrow 0_1^+$ transition (207 keV) as the Start. The events in

the bottom right circle, labelled as *"Delayed,"* follow a pattern that is the reverse of the *"Anti-delayed"* events. Figure 7.2 displays the three-dimensional representation of the "Delayed" and "Anti-delayed" gates in the $E_{\gamma 1} - E_{\gamma 2} - \Delta T$ cube. Energy gates were established using LaBr3(Ce) detectors on both energy axes for the $4_1^+ \rightarrow 2_1^+$ and $2_1^+ \rightarrow 0_1^+$ transitions, resulting in the creation of two time distributions.

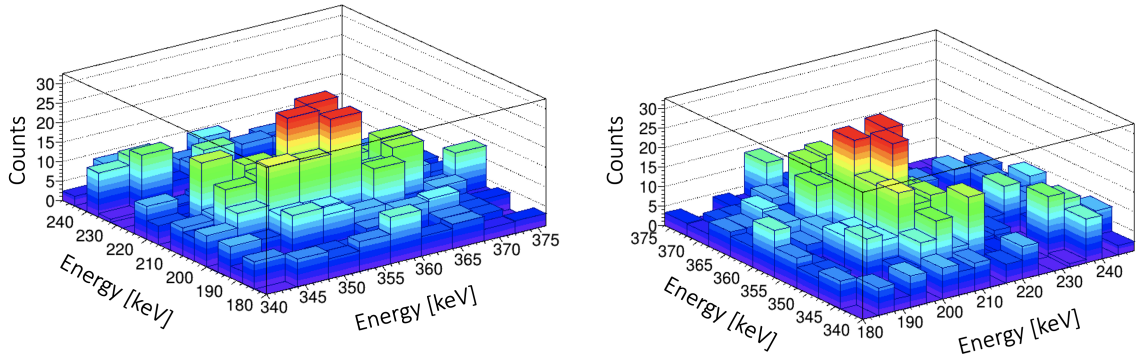

(a) Delayed (b) Anti-delayed

Figure 7.2: Projection on the $E_{\gamma 1} - E_{\gamma 2}$ plane of the experimental three-dimensional gates of the $E_{\gamma 1} - E_{\gamma 2} - \Delta T$ cube around the delayed (358,207) keV (a) and anti-delayed (207,358) keV (b) $4_1^+ \rightarrow 2_1^+ \rightarrow 0_1^+$ cascade in ^{190}W.

The results of the delayed and anti-delayed time distributions with the $(4_1^+ \rightarrow 2_1^+)$ (358 keV) feeding and the $(2_1^+ \rightarrow 0_1^+)$ (207 keV) decaying transition can be seen in Figure 7.3. By measuring the centroid or center of gravity of the delayed and anti-delayed time distributions, an experimental value of ΔC = 803(56) ps was obtained. The error calculation was performed using the standard deviation of the mean values of the delayed and anti-delayed time distributions. This value, along with a PRD correction of 255(5) ps, gives a lifetime value of τ = 274(28) ps for the 2_1^+ state in ^{190}W for the first time. This information was obtained using Equation (3.9) combined with the PRD correction shown in Chapter 5. (The fit parameters for the PRD are provided in the Appendix.)

The attempt was made to determine the lifetime of other excited yrast states such as 4_1^+ and 6_1^+ in ^{190}W. However, the task proved challenging as these states are prompt and there was limited data available, making it difficult to extract their lifetimes. For example, Figure 7.4 shows delayed and anti-delayed time distributions with the $(6_1^+ \rightarrow 4_1^+)$ (484 keV) feeding and the $(4_1^+ \rightarrow 2_1^+)$ (358 keV) decaying transition. The experimental value for the delayed and anti-delayed time distribution was obtained as $\Delta C = 75(42)$ ps, which gives a lifetime value of $\tau = -31(22)$ ps. In the present measurement, it was not possible to determine an

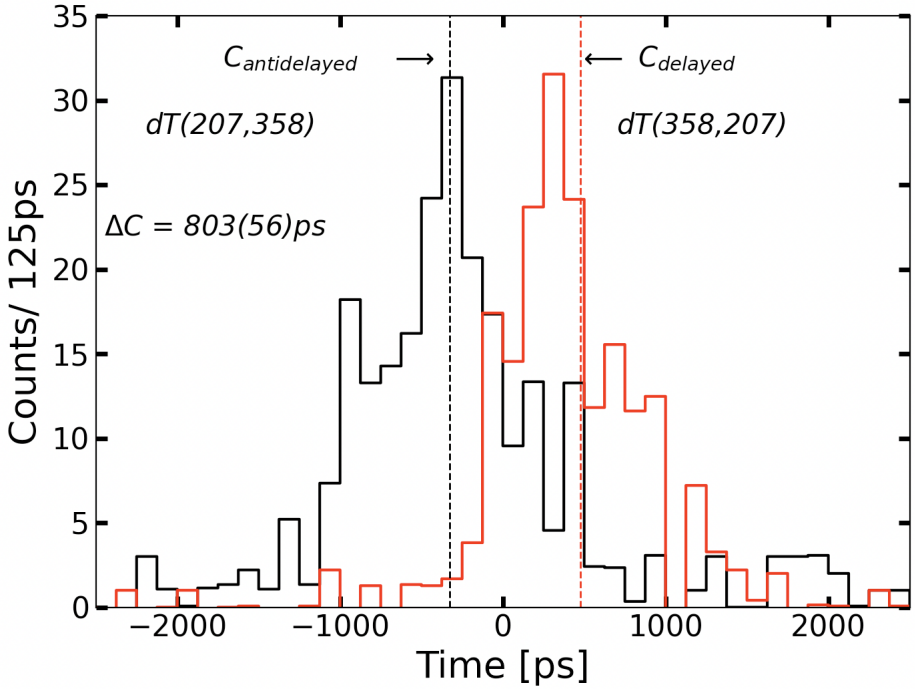

Figure 7.3: Delayed (red) and anti-delayed (black) time distributions generated from the $4_1^+ \rightarrow 2_1^+ \rightarrow 0_1^+$ cascade in ^{190}W for the lifetime measurement. The $LaBr_3$(Ce) gates were selected for the delayed distribution 358-207 keV and the anti-delayed distribution 207-358 keV.

accurate value of these excited states lifetimes. A negative value for the lifetime is unphysical (undefined), and the data indicates that the measurement is consistent with zero within a two sigma range. Therefore, the data was not sufficiently sensitive to accurately assess the presumed short lifetime. However, one can establish an upper limit for the lifetime based on the measurement. By applying a 5σ tolarance, the maximum lifetime can be calculated as follows: $\tau_{max} = -31 + 5 * \sigma = 79$ ps. This value corresponds to a lower limit for the B(E2) value, which is determined to be 18 W.u. To obtain information on the lifetime of these excited states, experiments using different techniques could be performed to obtain complementary information and build a more complete picture of the structure of the nuclei.

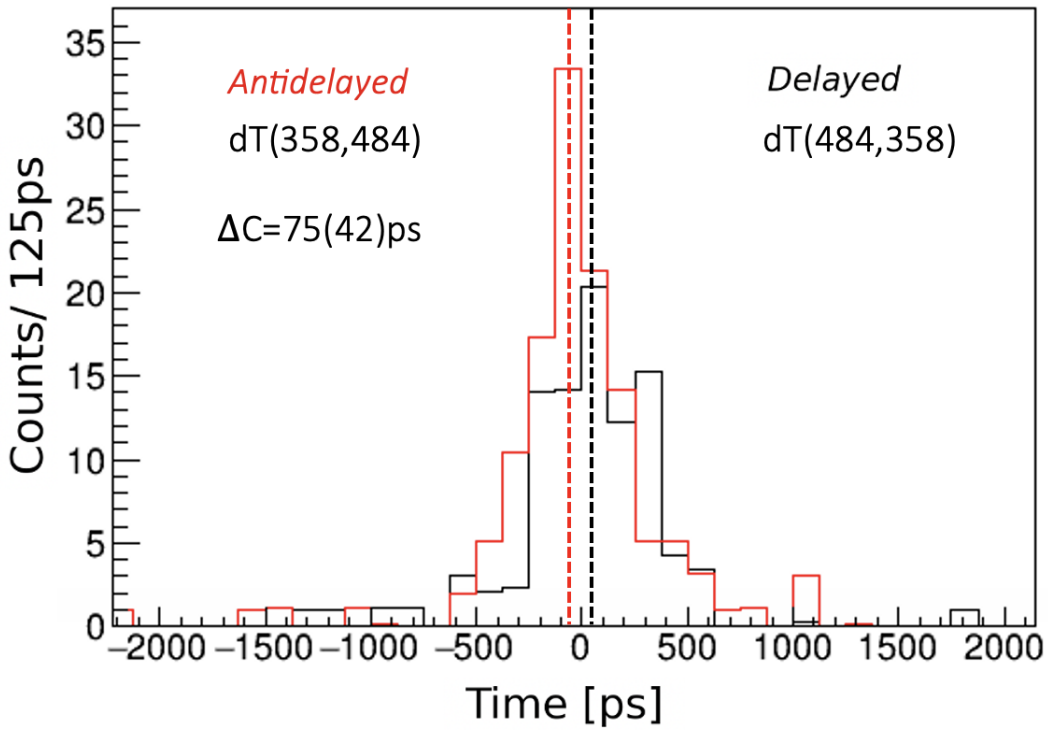

Figure 7.4: Delayed (red) and anti-delayed (black) time distributions generated from the $6_1^+ \rightarrow 4_1^+ \rightarrow 2_1^+$ cascade in ^{190}W for the lifetime measurement. The $LaBr_3(Ce)$ gates were selected for the delayed distribution 484-358 keV and the anti-delayed distribution 358-484 keV

8 Results

In this chapter, the results obtained after the data analysis are presented. The measurement of the lifetimes of excited states can directly determine the reduced electric quadrupole transition probability, $B(E2)$. Therefore, the value of the $B(E2)$ strength measured for the first 2^+ state of ^{190}W will be discussed in the following sections. The IBM-2 calculation will be introduced, followed by a comparison of experimental and theoretical results.

8.1 Even-even tungsten isotopes

As mentioned in Chapter 2, the energy ratio of the first 4^+ state to the first 2^+ state, $R_{4/2} = E(4_1^+)/E(2_1^+)$, in even-even nuclei is an experimentally accessible indicator of nuclear deformation [8]. A ratio of $R_{4/2} = 3.33$ represents an axially symmetric rotor described by SU(3) symmetry, $R_{4/2} = 2.0$ represents an harmonic vibrator U(5) symmetry, and $R_{4/2} = 2.5$ represents a triaxial rotor O(6) symmetry (γ-soft). Figure 8.1 shows the ratio of

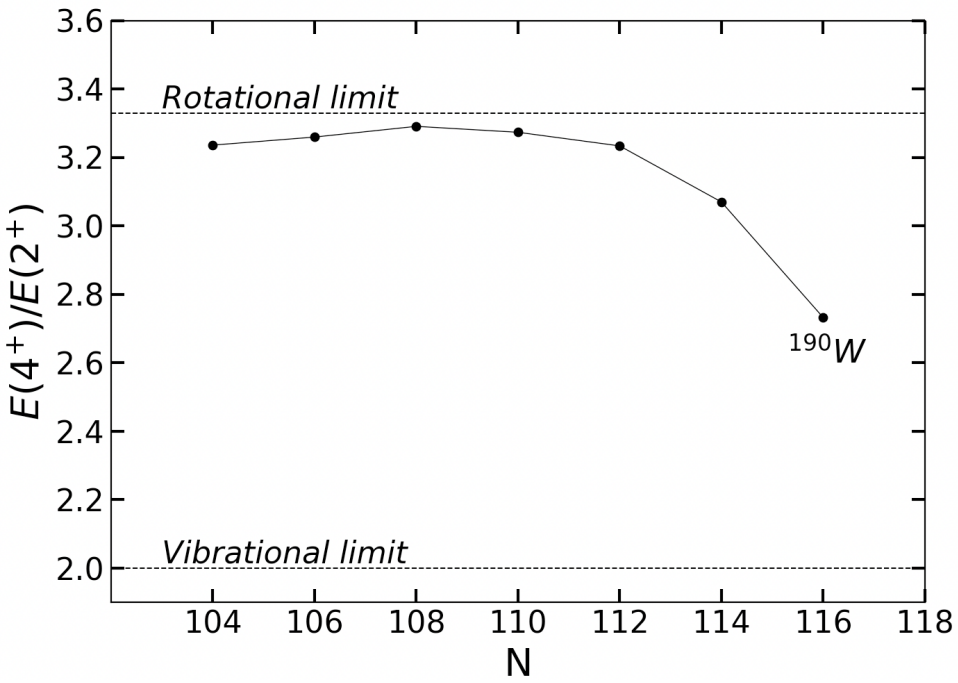

Figure 8.1: Experimental $E(4^+)/E(2^+)$ ratio from the yrast band for tungsten isotopes. The ratio for ^{190}W is 2.73 [13, 14, 15, 16, 17, 18, 19, 20, 21, 22, 23, 24, 25, 26, 27].

$R_{4/2} = E(4_1^+)/E(2_1^+)$ for even tungsten isotopes. The $R_{4/2}$ value shows a decrease in heavier even-even tungsten isotopes as more neutrons are added. This decrease could indicate γ softness, and potentially the beginning of the shape transition towards oblate-deformed ground states [10, 11, 12]. A potential reason for this drop in the energy ratio $R_{4/2}$ in ^{190}W in contrast to ^{188}W could be a proton sub-shell closure within this region. The difference in the energy ratio ($R_{4/2}$) between neighbouring even-even isotopes is given by

$$\delta R_{4/2} = R_{4/2}(Z,N) - R_{4/2}(Z,N+2). \tag{8.1}$$

Figure 8.2 shows this difference in energy ratio for neutron-rich tungsten isotopes. The differences in $\delta R_{4/2}$ away from the closed shells in the nuclear chart are observed between ^{188}W ($R_{4/2} = 3.07$) and ^{190}W ($R_{4/2} = 2.73$). The significant difference in the value of $\delta R_{4/2}$ between ^{188}W and ^{190}W, which is $\delta R_{4/2} > 0.3$, offers strong evidence of a dramatic alteration in the ground state structure of W isotopes as they transition from N= 114 to N= 116.

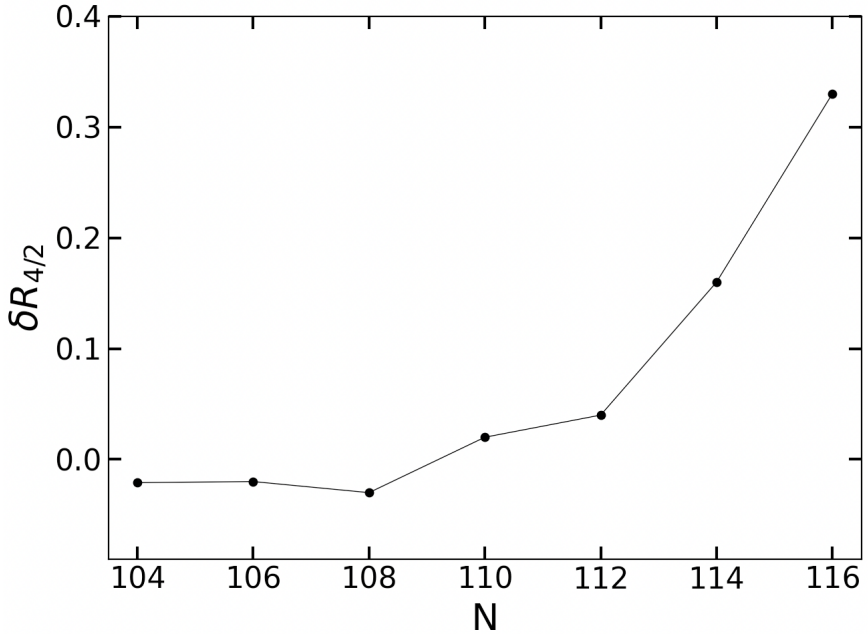

Figure 8.2: Systematics of the excitation energy difference between the energy ratio $\delta R_{4/2}$ for heavy even-even tungsten neutron rich nuclei [13, 14, 15, 16, 17, 18, 19, 20, 21, 22, 23, 24, 25, 26, 27].

The energy ratios of $E(2_2^+)/E(2_1^+)$ for even-even tungsten isotopes are presented in Figure 8.3. These ratios correspond to the susceptibility of the nuclear shape to changes in γ or β deformation, where the $E(2_2^+)$ and $E(0_2^+)$ levels are identified as the γ and β vibrational band heads, respectively. The excitation energy of these states reveals the degree of

γ or β softness. It is noteworthy that the most rigid nuclear shape among all W isotopes is found in ^{182}W (N = 108), as indicated by the maximum values of both ratios. Moreover, $E(4_1^+)/E(2_1^+)$ in Figure 8.1 also reaches its highest value in ^{182}W, nearly approaching the rigid-rotor limit of 3.3. On the other hand, $E(4_1^+)/E(2_1^+)$ decreases rapidly for W isotopes with N >108, which is consistent with an increasing γ softness as the nucleus approaches N = 116.

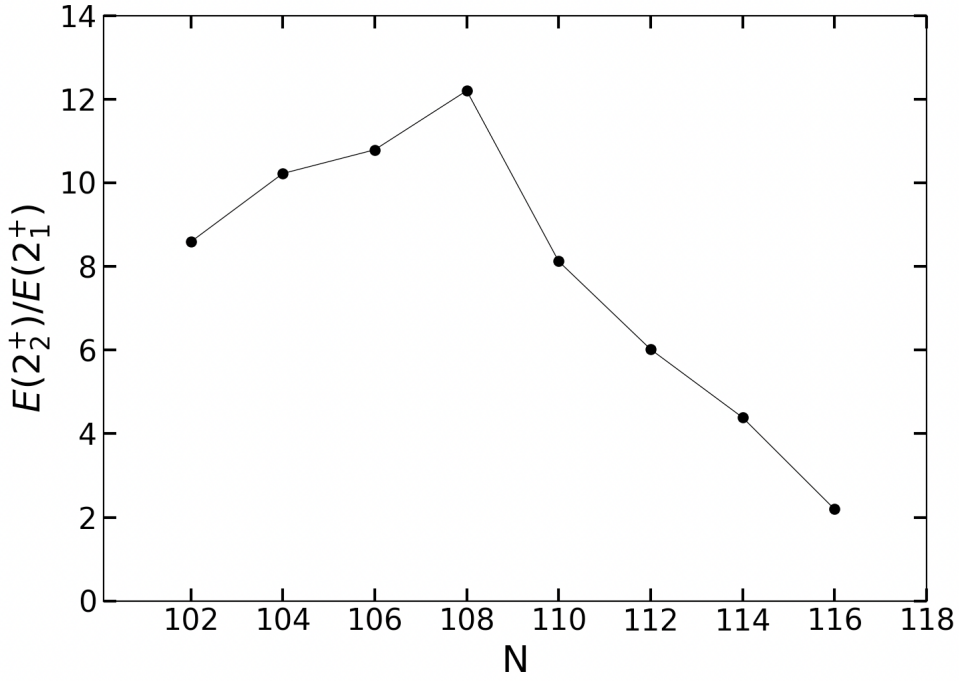

Figure 8.3: Experimental values of $E(2_2^+)/E(2_1^+)$ for even- even tungsten isotopes.

8.2 Reduced transition probability

As mentioned in the previous chapter, the lifetime of the 2_1^+ state was extracted using the GCD method. The value obtained in this work is $T_{1/2} = 190(19)$ ps, which represents the first measurement of the 2_1^+ state half-life in ^{190}W.

Table 8.1: Lifetime obtained in this work

Isotope	**Level**	E_γ **[keV]**	$T_{1/2}$ **[ps]**
^{190}W	2_1^+	207	190(19)

The shape of a nucleus is closely related to its reduced transition probability ($B(E2)$) and quadrupole moment (Q). The quadrupole moment measures the deviation of the nuclear charge distribution from spherical symmetry, while the reduced transition probability

measures the strength of the electric quadrupole transition between two nuclear states. For instance, a prolate nucleus (elongated along the symmetry axis) has a positive quadrupole moment, while an oblate nucleus (flattened along the symmetry axis) has a negative quadrupole moment. The reduced transition probability for electric quadrupole transitions depends on the magnitude and sign of the quadrupole moment, as well as the angular momentum of the transition. Larger values of the quadrupole moment correspond to stronger electric quadrupole transitions and smaller transition energies. Therefore, by measuring the reduced transition probability, information can be obtained regarding the shape and deformation of atomic nuclei.

The direct lifetime measurement of 2_1^+ state in ^{190}W, $B(E2;2_1^+ \rightarrow 0_{gs}^+)$ value can be measured. The relation between the lifetime and the reduced transition probability is given by the following equation [119].

$$B(E2;2_1^+ \rightarrow 0_{gs}^+) = \frac{8.161 \times 10^{13}}{E_\gamma^5 \cdot \tau \cdot (1+\alpha)}, \quad [e^2b^2]. \tag{8.2}$$

The $B(E2)$ value is expressed in units of e^2b^2, where E_γ is in keV, lifetime τ is in ps. The following equation shows the conversion of the unit e^2b^2 to Weisskopf single-particle transition (W.u) units:

$$B(E2)e^2b^2 = 5.94 \times 10^{-6} \cdot A^{4/3} \cdot B(E2)W.u \tag{8.3}$$

Table 8.2 presents the calculated $B(E2)$ value for ^{190}W using the measured lifetime of the 2_1^+ state.

Table 8.2: The $B(E2)$ strength of ^{190}W was determined by measuring the lifetime of the 2_1^+ state. The internal conversion coefficient α value used in the determination was taken from Ref. [120].

Isotope	$I_i \rightarrow I_f$	σL	τ [ps]	α	$B(E2)$ [W.u]
^{190}W	$2^+{}_1 \rightarrow 0_1^+$	E2	274(28)	0.275(4)	95(10)

Figure 8.4 shows the experimental $B(E2)$ values for even-even tungsten isotopes. The trend of decreasing $B(E2)$ values is observed until ^{186}W, with ^{188}W displaying a larger decrease compared to the systematic trend of lighter isotopes. However, the large uncertainty in ^{188}W and ^{190}W makes it difficult to interpret whether this deviation represents a change in shape or simply the continuation of decreasing collectivity as the closed neutron shell at $N = 126$ is approached. The observed trend is consistent with the expected minimum of $B(E2)$

strength in ^{190}W and the trend towards the shape transition. It remains unclear to what extent an increase beyond O(6) can be expected, or if it is suppressed by shell structure.

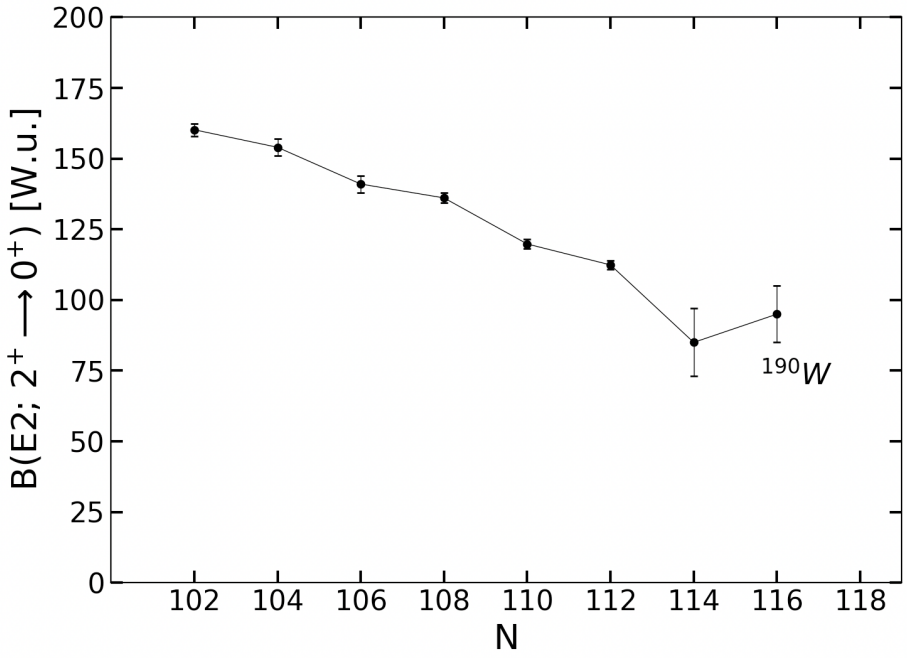

Figure 8.4: The experimental $B(E2;2_1^+ \rightarrow 0_1^+)$ values for tungsten isotopes [13, 14, 15, 16, 17, 18, 19, 20, 21, 22, 23, 24, 25, 26, 27]. The value for ^{190}W is from the current work.

Figure 8.5 shows literature values of $B(E2;2_1^+ \rightarrow 0_1^+)$ strengths for the Hf, W, Os and Pt isotopes, including the newly-derived value from the present work. All the available data systematically exhibit a downward trend from the mid-shell region toward the $N = 126$ shell closure. While the new data point for ^{190}W appears slightly higher, it is important to consider the larger error bars associated with the neutron-unstable isotopes ^{188}W and ^{190}W. Taking this into account, the data is in agreement with a systematic decrease in the $B(E2)$ values as well.

Moreover, the fact that the 2_2^+ state has a lower energy than the 4_1^+ state provides additional support for the interpretation within the γ-soft limit. Additionally, the ratio B_{22}, which represents the ratio of the transition probabilities $B(E2;2_2^+ \rightarrow 0_1^+)$ to $B(E2;2_2^+ \rightarrow 2_1^+)$, demonstrates a decreasing trend as neutron number increases, as depicted in Figure 8.6. This diminishing ratio towards ^{190}W indicates a near-forbidden decay of the 2_2^+ state to the ground state, which is typical for nuclei approaching the γ-soft limit.

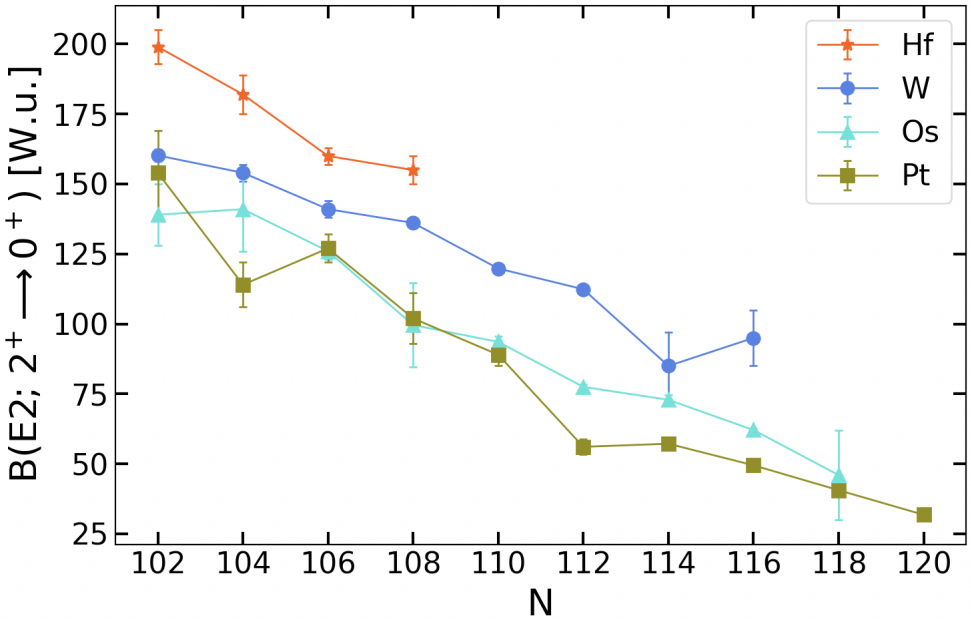

Figure 8.5: Experimental $B(E2; 2_1^+ \rightarrow 0_1^+)$ values in even-even Hf, W, Os, Pt isotopes. The data was taken from Nuclear Data Sheets and studies Ref [13, 14, 15, 16, 17, 18, 19, 20, 21, 22, 23, 24, 25, 26, 27].

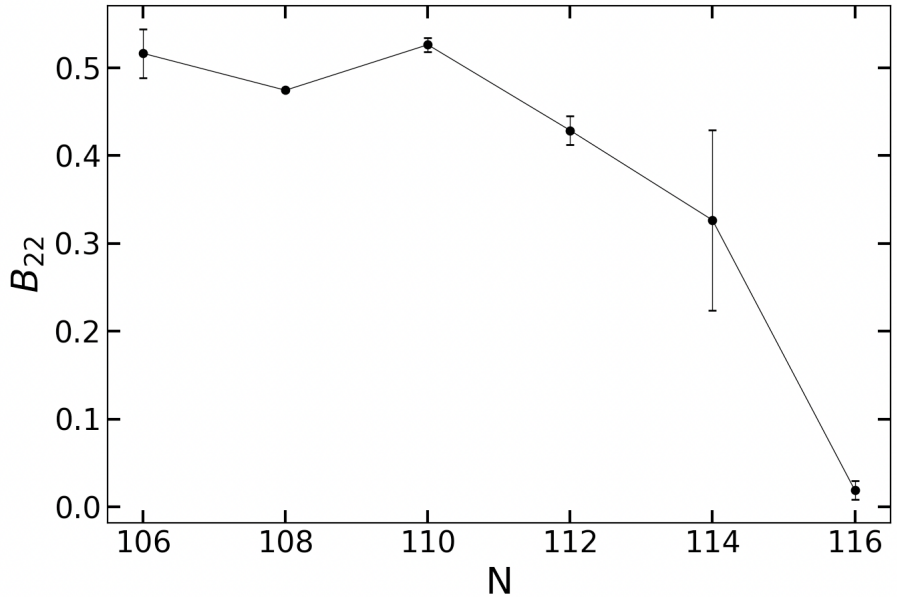

Figure 8.6: The B_{22} ratio is a function of neutron numbers for tungsten isotopic chains.

8.3 IBM-2 calculations

In the context of a shape (phase) transition from prolate to oblate nuclei, one might naively expect the minimum value of the $B(E2)$ transition probability to occur closest to the γ-soft

limit, with a subsequent increase upon entering the oblate-deformed region. This would correspond to a shift in the spectroscopic quadrupole moment of the 2_1^+ state, transitioning from negative to positive values and crossing zero at the γ-soft limit. Schematic IBM-1 calculations with constant boson numbers N demonstrate a mirror (point) symmetry of the $B(E2)$ (Q) values around $\chi = 0$, corresponding to $\gamma = 30°$, as illustrated in Ref. [5]. However, it is crucial to consider the shrinking valence space as the major shell closure at $N = 126$ approaches. This shrinking valence space has an impact on the level of collectivity and, therefore, alters the observed trend.

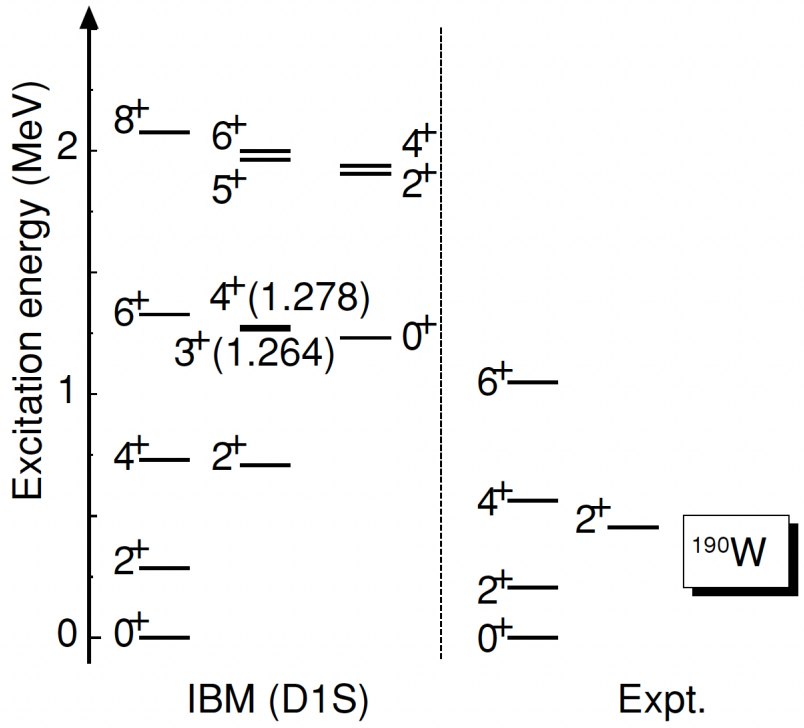

Figure 8.7: A comparison between the theoretical and experimental level schemes of ^{190}W [10]

To obtain more information about the calculation of spectroscopic properties of W isotopes, we suggest referring to the study conducted by Nomura et al. in References [10, 121]. Based on the Gogny-D1S energy density functional, a *Hartree-Fock-Boguliubov* (HFB) calculation yielded a *Potential Energy Surface* (PES) for each isotope. The calculated ground state band energies, the quasi-γ-bandhead and the quasi-β-bandhead energies for ^{190}W, sourced from Ref. [10], are depicted in Figure 8.7. The following IBM Hamiltonian, as shown in Equation (8.4), was used for the calculations using the parameters listed in Table 8.3 [121].

$$\hat{H}_{IBM} = \varepsilon \hat{n}_d + \kappa \hat{Q}_\pi \cdot \hat{Q}_\nu + \alpha \hat{L} \cdot \hat{L}. \tag{8.4}$$

Table 8.3: The parameters for the IBM Hamiltonian $\hat{H}_{IBM}$ [121]

Isotope	ε (keV)	$-\kappa$ (keV)	χ_π x10^3	χ_ν x10^3	α (keV)	C_β
^{190}W	71.3	275	572	-419	-2.72	5.60

The form of the $\hat{H}_{IBM}$ in Equation (8.4) is not the most general, but it encompasses all the essential features of the low-lying quadrupole collective states. The first term of the Hamiltonian is $\hat{n}_d = \hat{n}_{d\pi} + \hat{n}_{d\nu}$ where $\hat{n}_{d\rho} = d^\dagger_\rho \cdot \tilde{d}\rho$ and $\rho = \pi$ or ν. The second term is the quadrupole-quadrupole interaction between proton and neutron systems given in Chapter 2, Table 2.1. The third term is relevant to the moment of inertia of the rotational band and is defined as $\hat{L} = \hat{L}_\pi + \hat{L}_\nu$. This angular momentum operator for the boson system is $\hat{L}_\rho = \sqrt{10}[d^\dagger_\rho \tilde{d}\rho]$. Figure 8.8 shows the evolution of the derived IBM parameters for the Os, W and Pt nuclei as functions of the neutron number N.

Similarly, the potential energy surface (PES) can be calculated using the IBM-2, where there is a distinction between protons and neutrons. The parameters of the IBM-2 model are adjusted to maximize the overlap of both the HFB and the IBM-2 PES. Subsequently, the IBM-2 calculations provide the low-energy spectrum for each respective isotope, as well as the $E2$ matrix elements. The $E2$ transition operator $\hat{T}(E2)$ is given by Equation (2.44) in Chapter 2. However, it should be noted that this procedure does not allow for the fitting of effective charges on an isotope-by-isotope basis. In the study by Nomura et al. [10], a constant value was employed instead.

In Figure 8.9, a comparison was made between the $B(E2)$ data for W isotopes up to ^{190}W and the calculated values obtained using the parameters described in Ref. [10] (referred to as EDF-IBM2) and modified effective charges. It is evident that the previous prediction made in Ref. [10] systematically underestimates all the $B(E2)$ values, including the slope towards larger N. Although adjusting the effective boson charge in the model allows for scaling the absolute values of $B(E2)$, addressing the overly steep slope observed in the calculations from Ref. [10] poses a more challenging task. In an attempt to resolve this situation, we have pursued two alternative approaches.

The first approach is inspired by the work of Casten and Wolf [122], which introduces boson-number dependent effective charges. In the original "EDF-IBM2" formulation [10], a common effective charge of $e_B = e_\nu = e_\pi = 0.13$ eb was utilized. Then, the effective boson charge rescaled by $\tilde{e}_B = 0.5\,(1 + 0.15\,\chi)\,((N+1)/N)\,e_B$ with $\chi = \frac{1}{2}\,(\chi_\pi + \chi_\nu)$ and $e_B = 0.27$ b. The resulting values are shown in Figure 8.9 labelled as "EDF-IBM2-N", reproducing the known data well, however, it yields a $B(E2)$ value of nearly 60 W.u. for the heaviest calculated isotope, ^{196}W. It should be noted that this approach involves two parameters: an input charge e_B and a slope for the χ dependence.

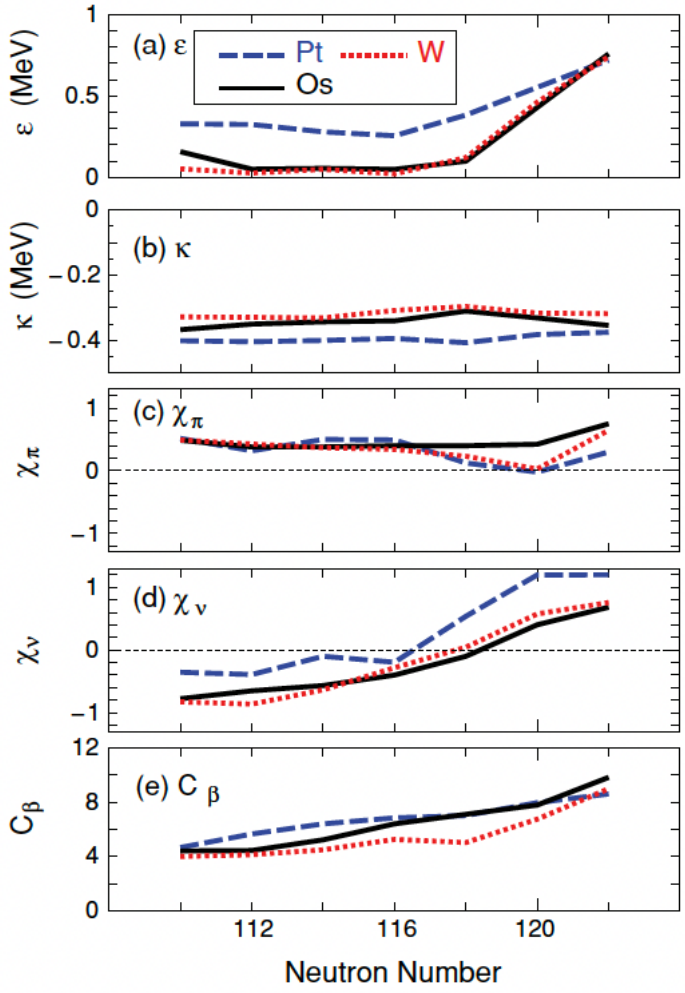

Figure 8.8: Derived IBM parameter values for the considered Pt, Os and W nuclei, represented by solid and dotted curves, respectively, as functions of N [10].

A simpler approach, involving only one parameter, is the use of different effective charges for protons and neutrons. In order to describe the available data satisfactorily, we have utilized $e_\nu = 0.122$ eb and determined $e_\pi = 0.183$ eb by requiring a typical ratio of $e_\pi/e_\nu = 1.5$. The resulting $B(E2)$ values obtained from this calculation are also presented in Figure 8.9, labelled as "EDF-IBM2-$\pi\nu$". With this approach, the number of free parameters remains unchanged compared to the original calculation, as only one boson charge is optimized to match the data. However, the systematic trend is significantly improved, similar to the EDF-IBM2-N method. Notably, apart from the absolute scale, the slope of the calculated $B(E2)$ values exhibits a change in the vicinity of the known data but exhibits a somewhat faster decrease towards the $N = 126$ shell closure compared to the boson-number dependent approach.

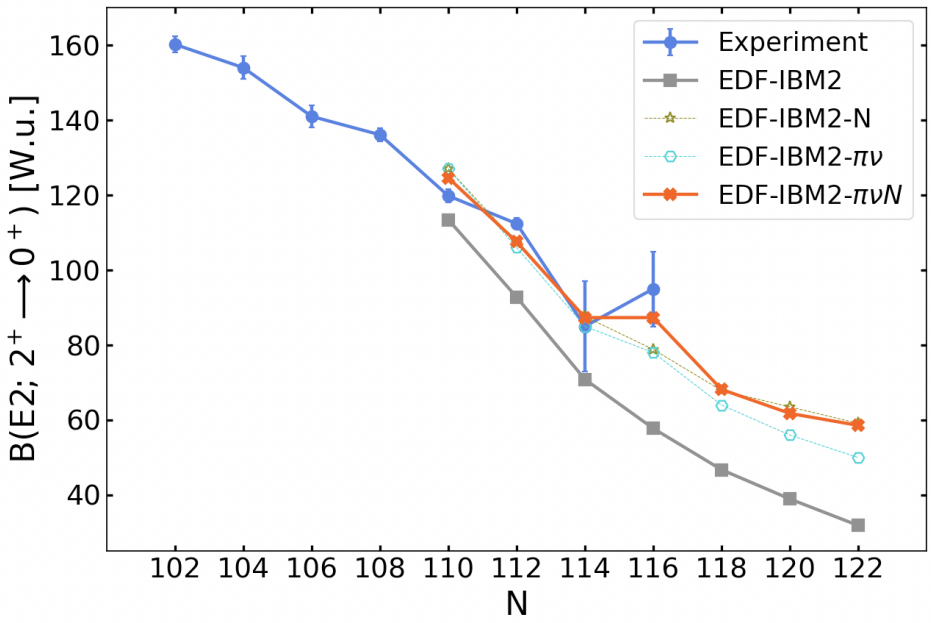

Figure 8.9: Comparison of the experimental and theoretical $B(E2;2_1^+ \rightarrow 0_1^+)$ calculations are performed for even-even tungsten isotopes. EDF-IBM2 refers to the calculation from Ref [10], while EDF-IBM2-N, EDF-IBM2-$\pi\nu$ and EDF-IBM2-$\pi\nu N$ refer to the calculation using the modified effective charges.

Finally, in order to describe the experimental data, the effective boson charges for the proton and neutron are increased. In the case of EDF-IBM2-$\pi\nu N$ in Figure 8.9, the effective boson charges $e_\nu = 0.145$ eb and $e_\pi = 0.2175$ eb are used, resulting in a ratio of 1.5. Furthermore, the effective boson charge are rescaled as $\tilde{e}_\nu = 0.5(1-0.3\chi_\nu)((N_\nu+1)/N_\nu)e_\nu$, which provides the best overall agreement with data up to ^{190}W.

It is noteworthy the flat behavior of $B(E2)$ values between ^{188}W and ^{190}W in the calculation, which arises from the change of sign in χ_ν due to the transition from prolate to oblate deformation. While this trend is only tentatively indicated by the W data because of the large uncertainties at neutron numbers 114 and 116, a similar systematic trend of $B(E2)$ values can be observed in Fig. 8.5 for the Pt isotopes at $N = 112, 114$. The Pt isotopes have been found to be soft triaxial, closely approaching the $O(6)$ symmetry between prolate and oblate structures.

Extending the EDF-IBM2-$\pi\nu$N model would be highly interesting, but it necessitates extended EDF-IBM2 calculations for lower neutron numbers. Additionally, this extension would greatly benefit from more precise measurements of the ^{188}W and ^{190}W $B(E2)$ values.

The revised $B(E2)$ values give an improved description of the available data. Furthermore, the recently obtained data point for ^{190}W with a value of 95(10) W.u. is less than two sigmas

from the newly calculated value of 78 W.u. To achieve a comprehensive description of the entire isotopic chain, further adjustments to the effective charges might be necessary. A combined approach of using different proton and neutron charges, but varying the neutron charge in a manner as described above would be promising, but requires extended EDF-IBM2 calculations toward lower neutron numbers, and would strongly benefit from more precise measurements of the ^{188}W and ^{190}W $B(E2)$ values.

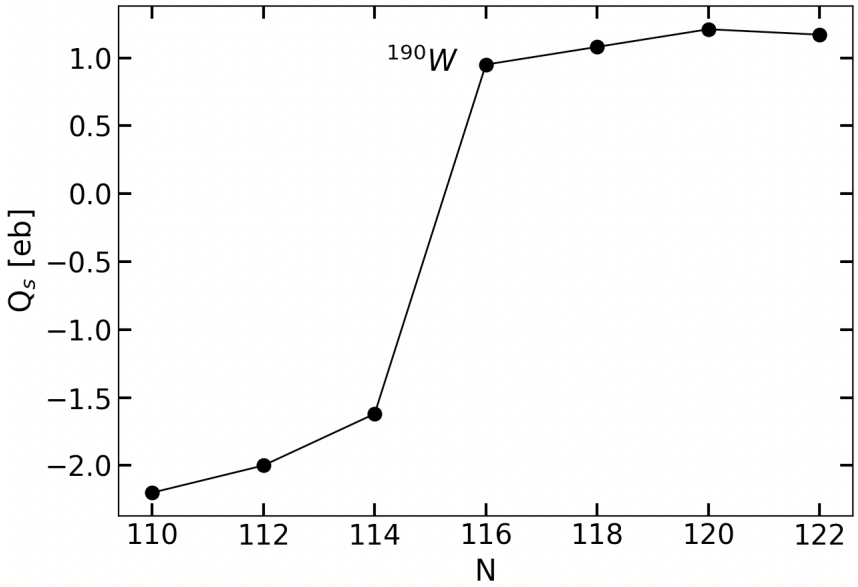

Figure 8.10: The spectroscopic quadrupole moments $Q_s(2_1^+)$ of even-even tungsten isotopes calculated with IBM-2 model.

However, the observed continuous decrease in $B(E2)$ values contradicts the expected schematic pattern of an increase from the γ-soft limit to oblate isotopes. Therefore, we also present the spectroscopic quadrupole moments, $Q_s(2_1^+)$ in Figure 8.10. As expected, a flip from negative to positive values from $N = 114$ to $N = 116$ is observed. However, it is important to note that the absolute values on the prolate side are smaller. This behaviour is due to the approach of the $N = 126$ shell closure. In the IBM-2, this is reflected in the decrease of the number of (neutron) bosons, which directly affects the calculation of $E2$ matrix elements. Therefore, despite the switch from prolate to oblate deformation at ^{190}W, a continuous drop in $B(E2)$ values are expected, consistent with the observed trend in experiments.

From these considerations, in view of the systematics of the $R_{4/2}$, B_{22} and $B(E2)$ values, the known spectroscopic data on ^{190}W matches the predictions for the most γ-soft, O(6)-like, isotope in the W isotopic chain, approaching the $N = 126$ shell closure.

9 Summary and Outlook

The measurement of lifetimes of excited states is a powerful method for investigating the atomic nucleus because it allows for a direct and independent evaluation of reduced transition probabilities. By studying transition rates, one can obtain valuable insights into single-particle configurations and nuclear collectivity, as well as the ability to verify theoretical models. In the nuclear chart, the mass region around $A \sim 190$, particularly ^{190}W, draws particular attention due to the collective behaviour that arises.

The generalised centroid difference method is the most appropriate experimental technique for measuring lifetimes ranging from a few nanoseconds down to tens of picoseconds, which is the focus of this PhD thesis. This technique relies on coincidences between the radiation that populates a nuclear level and the radiation that de-excites it, detected by fast scintillators such as $LaBr_3$(Ce) detectors. In order to achieve high performance in a $LaBr_3$(Ce) array, good time and energy resolution and a modular and efficient geometry are necessary. Therefore, the FATIMA array, consisting of 36 $LaBr_3$(Ce) detectors, in the DESPEC setup provides the optimal geometry and high performance.

In this experiment, we measured the lifetime of the first excited state in ^{190}W for the first time, which provides crucial information on nuclear deformation. To achieve this, it is necessary to reduce background noise. This was accomplished by using background subtraction for the $LaBr_3$(Ce) array, which improved the γ-γ coincidence technique based on the GCD method. As a result, the current measurement has determined the half-life of the 2^+ state in ^{190}W to be 190(19) ps, which corresponds to a $B(E2;2_1^+ \rightarrow 0_1^+)$ value of 95(10) W.u.

The $E(4_1^+)/E(2_1^+)$ energy ratio for the even-even tungsten isotopic chain shows that the shape of the tungsten isotopes changes from prolate to γ-soft with an increasing number of neutrons. The measured $B(E2)$, with large uncertainty, behaves differently from the trend. However, the result follows the trend towards the shape transition, with an expected minimum of $B(E2)$ strength in ^{190}W. It is also possible to interpret this deviation as the continuation of decreasing collectivity as the closed neutron shell at $N = 126$ is approached.

The theoretical calculation of the results is based on the Interacting Boson Model (EDF-IBM-2), using different effective boson charges for protons and neutrons. The theoretical values were taken from K. Nomura's work [10] and were calculated using the code NPBOS. The existence of non-zero spectroscopic quadrupole moments indicates the breaking of spherical symmetry. The theoretical calculation of Q_s for tungsten isotopes shows that

the sign of Q_s changes from ^{188}W to ^{190}W, indicating a shape transition in ^{190}W. From these considerations, in view of the systematical behaviour of the $R_{4/2}$, B_{22} and $B(E2)$ values, the known spectroscopic data on ^{190}W matches the predictions for the most γ-soft, $O(6)$-like, isotope in the W isotopic chain, approaching the $N = 126$ shell closure.

Theoretical models predict a transition from prolate to oblate shapes as the isotopes become heavier, however, the current data couldn't provide the lifetime information for the first 4^+ state since there was no sufficient data for this state. Therefore, further measurements in heavier isotopes will be necessary to comprehend this structural evolution fully.

$e_\nu = 0.145$ eb and derived $e_\pi = 0.2175$ eb

Appendix

Prompt curve determination in $\gamma-\gamma$ timing experiments

The PRD curve was generated and its calibration was carried out by following the procedures mentioned in Chapter 5. The gated spectra that are relevant to this study are presented in Figure 9.2, which were obtained from both ^{152}Eu source.

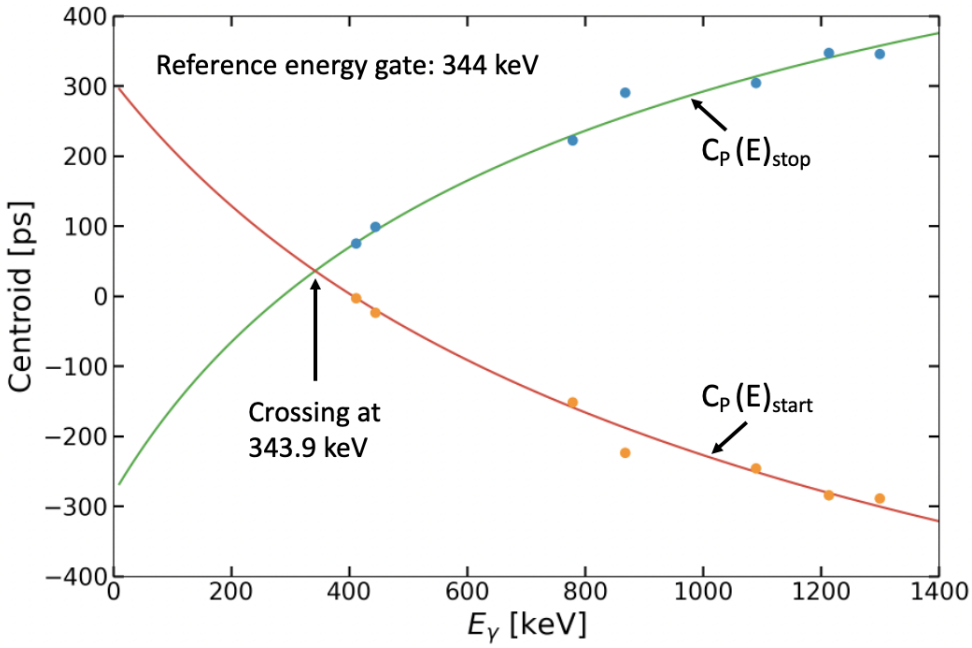

Figure 9.1: The prompt curves obtained the 344 keV energy gated for the two-timing branches by fitting the lifetime-corrected full energy centroids using the formula $C(E_\gamma) = \frac{a}{E_\gamma+b} + c$. To indicate the reference energy gated on the start and stop detectors, we use the notation $C_P(E)_{start}$ and $C_P(E)_{stop}$

The final PRD curve was calibrated using Equation (3.10)

$$a = -14835.7$$
$$b = 29.4279$$
$$c = 0.298588$$
$$d = 668.614$$

where a, b, c, and d are free fit parameters obtained from a chi-squared minimization fit, the PRD correction for the transition is obtained using $E_\gamma = 358$ keV for feeding energy and $E_\gamma = 207$ keV for decaying energy. Therefore, using Equation (3.10), we calculated $PRD(E_{feeder}) = 21.7841$ ps and $PRD(E_{decay}) = -234.43$ ps.

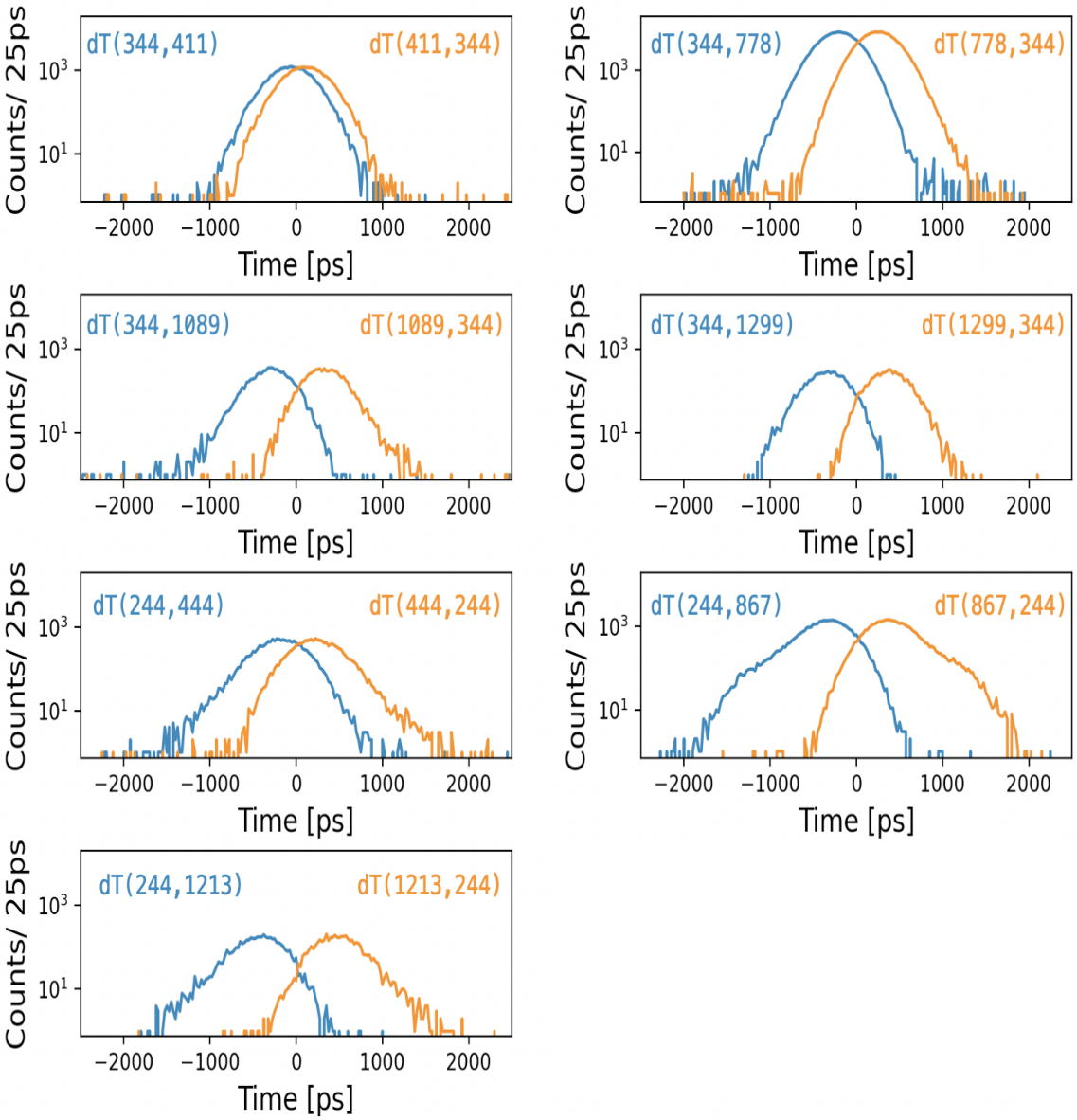

Figure 9.2: The delayed and anti-delayed time spectra were obtained using the $LaBr_3(Ce)$ detector with cascades of ^{152}Gd and ^{152}Sm. Time spectra were acquired by gating the detectors in both ways. The delayed time distributions are represented by the blue line, while the anti-delayed time distributions are represented by the orange line.

Definition of the Euler angles

The set of Euler angles comprises three angles that define the position and orientation of a solid object in a three-dimensional Euclidean space $\mathbb{R}^3$ relative to a fixed coordinate system. These angles are typically represented by α, β, and γ, and correspond to rotations around the x, y, and z axes of the fixed system, respectively.

The coordinate system used to define the orientation is typically denoted as (x, y, z), while the frame of the rigid object is represented as (X, Y, Z). The relative orientation between these two coordinate systems can be determined by three consecutive rotations, each one around a different axis of the fixed system.Figure 9.3 shows the orientation of a rigid body using the Euler angles.

- α: roll angle (around the x-axis),
- β: pitch angle (around the y-axis),
- γ: yaw or heading angle (around the z-axis).

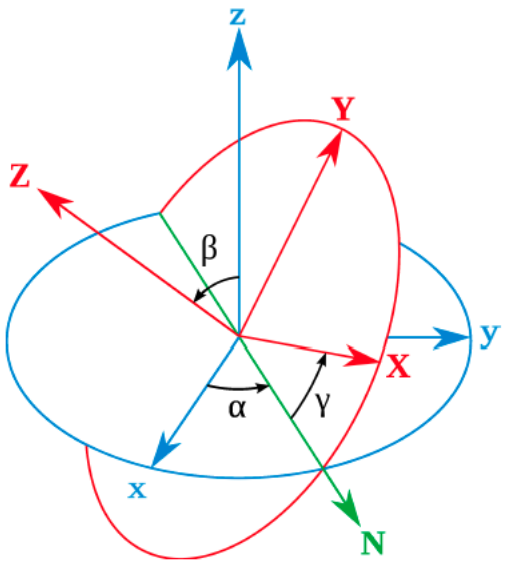

Figure 9.3: The orientation of a rigid body using the Euler angles. The figure is taken from Ref [123]

A spherical harmonic $Y_m^l(\theta,\phi)$ is a complex function of two real variables θ and ϕ that is continuous, bounded, and single-valued. The variables θ and ϕ have restrictions of $0 \leq \theta \leq \pi$ and $0 \leq \phi \leq 2\pi$, respectively. Two parameters, l and m, define the function, where l takes values of $0, 1, 2, ...$, and m ranges from $-l$ to l in increments of 1. Therefore, for each l value, there are $(2l+1)$ corresponding functions. The function and all of its derivatives are also single-valued, continuous, and finite.

In quantum mechanics, spherical harmonics are significant because they are the eigenfunctions of the operator of orbital angular momentum. These functions describe the distribution of angular momentum of particles that move in a spherically symmetric field with an orbital angular momentum of l and a projection of m. The value of $l(l+1)$ is the eigenvalue of the square of the orbital angular momentum operator, $\hat{L}^2$, while the projection of the orbital angular momentum operator on the quantization axis is represented by the eigenvalue m of $\hat{L}_x$. It is worth noting that l specifies the absolute value of the orbital angular momentum.

$Y_m^l(\theta,\phi)$	Formula
$Y_0^0(\theta,\phi)$	$\frac{1}{2}\sqrt{\frac{1}{\pi}}$
$Y_1^{-1}(\theta,\phi)$	$\sqrt{\frac{3}{8\pi}}\sin(\theta)e^{-i\phi}$
$Y_1^0(\theta,\phi)$	$\sqrt{\frac{3}{4\pi}}\cos(\theta)$
$Y_1^1(\theta,\phi)$	$-\sqrt{\frac{3}{8\pi}}\sin(\theta)e^{i\phi}$
$Y_2^{-2}(\theta,\phi)$	$\sqrt{\frac{15}{32\pi}}\sin^2(\theta)e^{-2i\phi}$
$Y_2^{-1}(\theta,\phi)$	$-\sqrt{\frac{15}{8\pi}}\sin(\theta)\cos(\theta)e^{-i\phi}$
$Y_2^0(\theta,\phi)$	$\sqrt{\frac{5}{16\pi}}(3\cos^2(\theta)-1)$
$Y_2^1(\theta,\phi)$	$\sqrt{\frac{15}{8\pi}}\sin(\theta)\cos(\theta)e^{i\phi}$
$Y_2^2(\theta,\phi)$	$\sqrt{\frac{15}{32\pi}}\sin^2(\theta)e^{2i\phi}$

Table 9.1: The first and second order of spherical harmonics

Bibliography

[1] W. Bothe and H. Becker, *Künstliche erregung von kern-γ-strahlen*. Zeitschrift für Physik **66**, 289-306 (1930).

[2] A. K. Mistry *et al.*, *The DESPEC setup for GSI and FAIR*. Nucl. Instrum. Methods A **1033**, 166662 (2022).

[3] W. Nazarewicz, M. A. Riley and J. D. Garrett, *Equilibrium deformations and excitation energies of single-quasiproton band heads of rare-earth nuclei.* Nucl. Phys. A **512**, 61-96 (1990).

[4] R. Bengtsson *et al.*, *Shape coexistence and shape transitions in even-even Pt and Hg isotopes.* Phys. Lett. B **183**, 1-6 (1987).

[5] J. Jolie and A. Linnemann, *Prolate-oblate phase transition in the Hf-Hg mass region.* Phys. Rev. C **68**, 031301 (2003).

[6] P. D. Stevenson *et al.*, *Shape evolution in the neutron-rich tungsten region.* Phys. Rev. C **72**, 047303 (2005).

[7] P. Sarriguren *et al.*, *Shape transitions in neutron-rich Yb, Hf, W, Os, and Pt isotopes within a Skyrme Hartree-Fock+ BCS approach.* Phys. Rev. C **77**, 064322 (2008).

[8] R. F. Casten, *Nuclear Structure form a Simple Prespective*. Oxford Science Publications (2000).

[9] R. F. Casten and B. M. Sherrill, *The study of exotic nuclei*. Progress in Particle and Nuclear Phys. **45**, S171-S233 (2000).

[10] K. Nomura , *et al., Collective structural evolution in neutron-rich Yb, Hf, W, Os, and Pt isotopes*. Phys. Rev. C **84(5)**, 054316 (2011).

[11] Z. Podolyák, *Prolate-oblate shape transition in heavy neutron-rich nuclei*. Journal of Phys. Conference Series **381**, 012052 (2012).

[12] P. J. R. Mason *et al.*, *Half-life of the yrast 2^+ state in ^{188}W: Evolution of deformation and collectivity in neutron-rich tungsten isotopes*. Phys. Rev. C. **88**, 044301 (2013).

[13] C. M. Baglin, *Nuclear Data Sheets for A = 186*. Nuclear Data Sheets **99**, 1-196 (2003).

[14] B. Singh, *Nuclear Data Sheets for A = 190*. Nuclear Data Sheets **99**, 275-481 (2003).

[15] E. Achterberg and O.A. Capurro and G.V. Marti, *Nuclear Data Sheets for A = 178*. Nuclear Data Sheets **110**, 1473-1688 (2009).

[16] S. -C. WU and H. NIU, *Nuclear Data Sheets for A = 180*. Nuclear Data Sheets **100**, 483-705 (2003).

[17] B. Singh and J. C. Roediger, *Nuclear Data Sheets for A = 182*. Nuclear Data Sheets **111**, 2081-2330 (2010).

[18] C. M. Baglin, *Nuclear Data Sheets for A = 184*. Nuclear Data Sheets **111**, 275-523 (2010).

[19] B. Singh and J. C. Roediger, *Nuclear Data Sheets for A = 188*. Nuclear Data Sheets **95**, 387-541 (2002).

[20] E. Browne and H. Junde, *Nuclear Data Sheets for A = 174*. Nuclear Data Sheets **87**, 15-176 (1999).

[21] M.S. Basunia, *Nuclear Data Sheets for A = 176*. Nuclear Data Sheets **107**, 791-1026 (2006).

[22] C. M. Baglin, *Nuclear Data Sheets for A = 192*. Nuclear Data Sheets **84**, 717-900 (1998).

[23] B. Singh and JC. Roediger, *Nuclear Data Sheets for A = 194*. Nuclear Data Sheets **107**, 1531-1746 (2006).

[24] B. Singh and JC. Roediger, *Nuclear Data Sheets for A = 196*. Nuclear Data Sheets **108**, 1093-1286 (2007).

[25] B. Singh and JC. Roediger, *Nuclear Data Sheets for A = 198*. Nuclear Data Sheets **110**, 2533-2688 (2009).

[26] J.-M. Régis *et al.*, *Sub-nanosecond lifetime measurements using the Double Orange Spectrometer at the cologne 10 MV Tandem accelerator*. EPJ Web of Conferences **606**, 466-474 (2009).

[27] M. Rudigier *et al.*, *Lifetime of the first excited 2^+ state in ^{172}W and ^{178}W*. Nucl. Instrum. Methods A. **847**, 89-100 (2010).

[28] Z. Bay, *Calculation of Decay Times from Coincidence Experiments*. Phys. Rev. **77**, 419 - 419 (1950).

[29] J.-M. Régis *et al.*, *The Generalized Centroid Difference method for lifetime measurements via γ-γ coincidences using large fast-timing arrays*. EPJ Web of Conferences **93**, 01013 (2015).

[30] M. Rudigier *et al.*, *FATIMA-FAst TIMing Array for DESPEC at FAIR*. Nucl. Instrum. Methods A **969**, 163967 (2020).

[31] E. M. Burbidge *et al.*, *Synthesis of the elements in stars*. Rev. of Modern Phys. **29(4)**, 547 (1957).

[32] F. Iachello, A. Arima, *The interacting boson model.* Springer US **13**, (1979).

[33] K. L. G. Heyde, *The Nuclear Shell Model*. Springer, Berlin (1994).

[34] R. D. Woods, D. S. David, *Diffuse Surface Optical Model for Nucleon-Nuclei Scattering.* Phys. Rev. **95**, 577–578 (1954).

[35] K. S. Krane, *Introductory nuclear physics*. Wiley, New York (1988).

[36] J. Lilley, *Nuclear Physics: Principles and Applications.* John Wiley & Sons (2013).

[37] M. G. Mayer, *On Closed Shells in Nuclei. II.* Phys. Rev. **75**, 1969 (1949).

[38] O. Haxel, J. H. D. Jensen, and H. E. Suess, *On the "Magic Numbers" in Nuclear Structure.* Phys. Rev. **75**, 1766 (1949).

[39] A. Bohr and B. R. Mottelson, *Nuclear Structure, Volume II, Nuclear Deformations (Book Review)*. Astrophysical Letters **19**, 103 (1973).

[40] M. Pi *et al.*, *Time-dependent Thomas-Fermi approach to nuclear monopole oscillations*. Phys. Lett. B **166(1)**, 1-4 (1986).

[41] J. M. Pearson, *The incompressibility of nuclear matter and the breathing mode*. Phys. Lett. B **271(1)**, 12-16 (1991).

[42] M. Goldhaber and E. Teller, *On Nuclear Dipole Vibrations*. Phys. Rev. **74(9)**, 1046 (1948).

[43] L. P. Gaffney *et al.*, *Studies of pear-shaped nuclei using accelerated radioactive beams.* Nature **497**, 199-204 (2013).

[44] A. Bohr, *The coupling of nuclear surface oscillations to the motion of individual nucleons*, (1952).

[45] D. L. Hill and J. A. Wheeler, *Nuclear Constitution and the Interpretation of Fission Phenomena.* Phys. Rev. **89(5)**, 1102 (1953).

[46] L. Wilets and M. Jean, *Surface Oscillations in Even-Even Nuclei.* Phys. Rev. **102(3)**, 788 (1956).

[47] T. Möller, *Aspects of nuclear collectivity studied in projectile Coulomb excitation experiments.* Ph.D. thesis (2014).

[48] A. Arima and F. Iachello, *Collective Nuclear States as Representations of a SU(6) Group*. Phys. Rev. Lett. **35(16)**, 1069 (1975).

[49] A. Arima and F. Iachello, *Interacting Boson Model of Collective States I. The Vibrational Limit*. Ann. Phys. **99(2)**, 253-317 (1976).

[50] A. Arima and F. Iachello, *Interacting boson model of collective nuclear states IV. The O(6) limit*. Ann. Phys. **123(2)**, 468-492 (1979).

[51] A. Arima and F. Iachello, *Interacting boson model of collective nuclear states II. The rotational limit*. Ann. Phys. **111(1)**, 201-238 (1978).

[52] A. Leviatan and N. Gavrielov, *Coexisting partial dynamical symmetries and multiple shapes.* Journal of Phys. Conference Series **1071(1)**, 012014 (2018).

[53] R. F. Casten and D. D. Warner, *The interacting boson approximation.* Rev. Mod. Phys. **60**, 389 (1988).

[54] J. N. Ginocchio and M. W. Kirson, *Relationship between the Bohr Collective Hamiltonian and the Interacting-Boson Model.* Phys. Rev. Lett. **44(26)**, 1744-1747 (1980).

[55] A. E. L. Dieperink, O. Scholten and F. Iachello, *CClassical Limit of the Interacting-Boson Model.* Phys. Rev. Lett. **44(26)**, 1747-1750 (1980).

[56] O. S. Roosmalen, *Algebraic descriptions of nuclear and molecular rotation-vibration spectra.* Ph.D. thesis (1982).

[57] F. Iachello, *Analytic Description of Critical Point Nuclei in a Spherical-Axially Deformed Shape Phase Transition*. Phys. Rev. Lett. **87**, 052502 (2001).

[58] F. Iachello, *Dynamic Symmetries at the Critical Point*. Phys. Rev. Lett. **85**, 3580 (2000).

[59] D. D. Warner and R. F. Casten, *Revised Formulation of the Phenomenological Interacting Boson Approximation.* Phys. Rev. Lett. **48(20)**, 1385 (1982).

[60] P. O. Lipas *et al.*, *IBA consistent-Q formalism extended to the vibrational region.* Phys. Lett. B **155**, 295–298 (1985).

[61] D. Bohle *et al.*, *New magnetic dipole excitation mode studied in the heavy deformed nucleus* ^{156}*Gd by inelastic electron scattering*. Phys. Rev. Lett. B **137**, 27–31 (1984).

[62] A. Richter, *Probing the nuclear magnetic dipole response with electrons, photons and hadrons*. Progress in Particle and Nuclear Phys. **34**, 261–284 (1995).

[63] K -H. Kim *et al.*, *IBM-2 calculations of even-even Pd nuclei*. Nucl. Phys. A **604(2)**, 163–182 (1996).

[64] A. Arima *et al.*, *Collective nuclear states as symmetric couplings of proton and neutron excitations*. Phys. Lett. B **66**, 205–208 (1977).

[65] N. Pietralla *et al.*, *Experiments on multiphonon states with proton–neutron mixed symmetry in vibrational nuclei*. Prog. in Part. and Nucl. Phys. **60**, 225–282 (2008).

[66] E. Majorana, *Teoria simmetrica dell'elettrone e del positrone*. Il Nuovo Cimento **14**, 171–184 (1937).

[67] T. Otsuka, A. Arima and F. Iachello, *Nuclear shell model and interacting bosons*. Nucl. Phys. A **309**, 1-33 (1978).

[68] N. A. Smirnova *et al.*, *Interrelation between the isoscalar octupole phonon and the proton-neutron mixed-symmetry quadrupole phonon in near-spherical nuclei*. Nucl. Phys. A **678**, 235 (2000).

[69] D. Warner, *A triple point in nuclei*. Nature **420**, 614 (2002).

[70] J. Jolie *et al.*, *Triple Point of Nuclear Deformations* Phys. Rev. Lett. **89**, 182502 (2002).

[71] E. López-Moreno and O. Castaños, *Shapes and stability within the interacting boson model: Dynamical symmetries*. Phys. Rev. C. **54**, 2374 (1996).

[72] E. López-Moreno and O. Castaños, *Shapes and stability within the interacting boson model: effective Hamiltonians*. Rev. Mex. Fis. **44**, 48 (1998).

[73] D. Kusnezov, *Incompleteness of Representation Theory: Hidden Symmetries and Quantum Nonintegrability* Phys. Rev. Lett. **79**, 537 (1997).

[74] A. M. Shirokov *et al.*, *Parameter symmetry of the interacting boson model*. Phys. Lett. B **434**, 237 (1988).

[75] D. B. Fossan and E.K. Warburton, *Nuclear Spectroscopy and Reactions. Part C*. New York: Academic Press (1974).

[76] J.-M. Régis *et al.*, *The mirror symmetric centroid difference method for picosecond lifetime measurements via γ–γ coincidences using very fast $LaBr_3$(Ce) scintillator detectors*. Nucl. Instrum. Methods. A **622(1)**, 83-92 (2010).

[77] H. Mach *et al.*, *A method for picosecond lifetime measurements for neutron-rich nuclei:(1) Outline of the method*. Nucl. Instrum. Methods A **280(1)**, 49-72 (1989).

[78] L. Boström *et al.*, *Numerical analysis of the time spectrum of delayed coincidences, I*. Nucl. Instrum. Methods **44**, 61-64 (1966).

[79] B. Olsen and L. Boström, *Numerical analysis of the time spectrum of delayed coincidences, II*. Nucl. Instrum. Methods A **44**, 65-72 (1966).

[80] M. Moszyński and H. Mach, *A method for picosecond lifetime measurements for neutron-rich nuclei: (2) Timing study with scintillation counters*. Nucl. Instrum. Methods. A **277**, 407 (1989).

[81] J.-M. Régis *et al.*, *The generalized centroid difference method for picosecond sensitive determination of lifetimes of nuclear excited states using large fast-timing arrays*. Nucl. Instrum. Methods. A **726**, 1-12 (2013).

[82] J.-M. Régis *et al.*, *Germanium-gated γ-γ fast timing of excited states in fission fragments using the EXILL&FATIMA spectrometer*. Nucl. Instrum. Methods. A **763**, 210-220 (2014).

[83] J.-M. Régis *et al.*, *The time-walk of analog constant fraction discriminators using very fast scintillator detectors with linear and non-linear energy response*. Nucl. Instrum. Methods. A **684**, 36-45 (2012).

[84] H. Geissel *et al.*, *The GSI projectile fragment separator (FRS): a versatile magnetic system for relativistic heavy ions.* Nucl. Instrum. Methods. B **70**, 286-297 (1992).

[85] N. Angert and C. Schmelzer, *The UNILAC, a variable energy linear accelerator for atomic ions of any mass.* Kerntechnik . **11**, 690-695 (1969).

[86] M. Steiner *et al.*, *Preliminary measurements of SIS 18 beam parameters*. Nucl. Instrum. Methods A **312(3)**, 420-424 (1992).

[87] H. Geissel, G. Münzenberg and C. Scheidenberger, *25 Years of FRS Experiments and New Horizons.* New Horizons in Fundamental Phys., 55-79 (2017).

[88] R. Kumar *et al.*, *Testing of a DSSSD detector for the stopped RISING project*. Nucl. Instrum. Methods A **598(3)**, 754-758 (2009).

[89] The GSI Fragment Separator Website, http://web-docs.gsi.de/~nkuzminc/TOF_Update.html, 2022.

[90] R. Schneider and A. Stolz, *Technical Manual Ionization Chamber MUSIC80*. Technical Manual, Technische Universität München, (2000).

[91] H. A. Bethe and J. Ashkin, *Experimental Nuclear Physics.* Wiley, New York, (1953).

[92] R. Janik *et al.*, *Time Projection Chambers with C-pads for heavy ion tracking*. Nucl. Instrum. Methods A **640(1)**, 54-57 (2011).

[93] J. Simpson *et al.*, *The Euroball Spectrometer*. Zeitschrift für Physik A Hadrons and Nuclei **358(2)**, 139-143 (1997).

[94] T. Davinson *et al.*, Technical Report For the Design, Construction and Commissioning of the Advanced Implantation Detector Array (AIDA), https://fair-center.de/user/experiments/nustar/documents/technical-design-reports, 2008.

[95] O. Hall, *β-delayed neutron emission of r-process nuclei at the N= 82 shell closure.* Phys. Lett. B **816**, 136266 (2021).

[96] I. Lazarus *et al.*, *The GREAT triggerless total data readout method.* IEEE Transactions on Nucl. Sci. **48(3)**, 567-569 (2001).

[97] D. Braga *et al.*, *AIDA: A 16-Channel Amplifier ASIC to Read Out the Advanced Implantation Detector Array for Experiments in Nuclear Decay Spectroscopy.* IEEE Transactions on Nucl. Sci. 1924-1928 (2009).

[98] V. F. E. Pucknell, The MIDAS multi instance data acquisition system, http://npg.dl.ac.uk/MIDAS, Daresbury Laboratory, (1995).

[99] O. J. Roberts *et al.*, *A $LaBr_3$: Ce fast-timing array for DESPEC at FAIR*. Nucl. Instrum. Methods A **748**, 91-95 (2014).

[100] F. Gonnella *et al.*, *Time over threshold in the presence of noise*. Nucl. Instrum. Methods A **791**, 16-21 (2015).

[101] J. Adamczewski-Musch and N. Kurz, *The GosipGUI Framework for Control and Benchmarking of Readout Electronics Front-Ends.* IEEE Transactions on Nucl. Sci. **68(8)**,2074-2080 (2021).

[102] Sensl: C-Series datasheet, https://www.mouser.com/datasheet/2/308/DS-MicroCseries-1489568.pdf.

[103] J. Hoffmann *et al.*, *New TASCA data acquisition hardware development for the search of element 119 and 120.* GSI Scientific Report PHN-IS-EE-03 **253**, (2011).

[104] GSI Multi Branch System (MBS), https://www.gsi.de/en/work/research/experiment_electronics/data_processing/data_acquisition/mbs.html.

[105] General Machine Timing System at GSI and FAIR, https://www-acc.gsi.de/wiki/Timing/WebHome.

[106] J. Adamczewski-Musch and B. Bellenot and A. Linev, *Web interface for online ROOT and DAQ applications.* 2014 19^{th} IEEE-NPSS Real Time Conference, 1-5.

[107] J. Adamczewski-Musch and B. Bellenot and A. Linev, *Mass storage interface LTSM for FAIR Phase 0 data acquisition.* EPJ Web of Conferences **245**, 01018 (2020).

[108] ucesb - unpack and check every single bit, http://fy.chalmers.se/~f96hajo/ucesb/.

[109] R. Brun and F. Rademakers, *ROOT - An object oriented data analysis framework.* Nucl. Instrum. Methods A **389(1)**, 81-86 (1997).

[110] NNDC Chart of Nuclides, https://www.nndc.bnl.gov/. 107, 131, 162, 206, 207.

[111] C. Scheidenberger, *et al., Charge states of relativistic heavy ions in matter*. Nucl. Instrum. Methods B **142(4)**, 441-462 (1998).

[112] Programs to predict charge-state distributions of swift heavy ions, http://web-docs.gsi.de/~weick/charge_states/.

[113] M. Caamaño, *et al., Isomers in neutron-rich A≈190 nuclides from* ^{208}*Pb fragmentation* . Eur. Phys. J. A **23**, 201 (2005).

[114] Z. Podolyák, *et al., Isomer spectroscopy of neutron rich* $^{190}W_{116}$. Phys. Lett. B **491**, 225 (2000).

[115] N. Alkhomashi, *et al.,* β^-*-delayed spectroscopy of neutron-rich tantalum nuclei: Shape evolution in neutron-rich tungsten isotopes*. Phys. Rev. C **80**, 064308 (2009).

[116] G. J. Lane, *et al., Structure of neutron-rich tungsten nuclei and evidence for a 10^- isomer in ^{190}W*. Phys. Rev. C **82(5)**, 051304 (2010).

[117] S. J. Steer, *et al., Isomeric states observed in heavy neutron-rich nuclei populated in the fragmentation of a ^{208}Pb beam*. Phys. Rev. C **84(4)**, 044313 (2011).

[118] J. F. Farrelly, *et al., Revision of the K-Isomer in $^{190}W_{116}$*. Acta Phy. Polonica B **40(3)**, 885-888 (2009).

[119] D. J. Rowe and J. L. Wood, *Fundamentals of Nuclear Models: Foundational Models*. World Scientific (2010).

[120] Online Conversion Coefficient Calculator, consulted in 2022 http://bricc.anu.edu.au/.

[121] K. Nomura *et al.*, *Spectroscopic calculations of the low-lying structure in exotic Os and W isotopes*. Phys. Rev. C. **83**, 054303 (2011).

[122] R. F. Casten and A. Wolf, *Approximate analytic expression for $B(E2)$ values in the interacting boson model*. Phys. Rev. C **35(3)**, 1156 (1987).

[123] Euler angles, http://en.wikipedia.org/wiki/Euler_angles.

List of Acronyms

ADC Analogue-to-Digital Converter

AIDA Advanced Implantation Detector Array

ASIC Application Specific Integrated Circuit

DAQ Data AQuisition system

DESPEC DEcay SPECtroscopy

ECR Electron Cyclotron Resonance

EDF Energy Density Function

ESR Experimental Storage Ring

FAIR Facility for Antiproton and Ion Research

FATIMA FAst TIMing Array

FEBEX Front End Board with optical link EXtension

FEE Front End Electronics

FEP Full Energy Peaks

FPGA Field Programmable Gate Array

FRS FRagment Separator

FSS Fully-Symmetric States

FWHM Full Width at Half Maximum

GCD Deneralised Centroid Difference

GOSIP Gigabit Optical Serial Interface Protocol

GSI Gesellschaft für Schwerionenforschung

HFB Hartree-Fock-Boguliubov

HPGe High-Purity Germanium

IBM Interacting Boson Model

IC Internal Conversion coefficient

$LaBr_3$(Ce) Cerium doped lanthanum bromide

LTSM Lightweight Tivoli Storage Manager

MBS Multi-Branch-System

MHTDC MultiHit Time to Digital Converter

MIDAS Multi Instance Data Acquisition System

MSS Mixed-Symmetry States

MUSIC MUltiple Sampling Ionization Chamber

PES Potential Energy Surface

PID Particle IDentification

PRD Prompt Response Difference

PRF Prompt Response Function

RIB Radioactive Ion Beam

RISING Rare ISotope INvestigations at GSI

PMT PhotoMultiplier Tubes

SCI SCIntillator

TAC Time-to-Amplitude Converter

TDC Time-to-Digital Converter

ToF Time of Flight

ToT Time-over-Threshold

TP TwinPeaks

TPC Time Projection Chamber

Ucesb Unpack and check every single bit

UNILAC Universal Linear Accelerator

WR White Rabbit

List of publications

- Bozkurt, V. , Erturk, S. , Şahin, E. *Yeni Gelistirilen NUMEXO2 Dijital Elektronik ile EXOGAM2 Dedektorunun K-Parametresine Bagli Enerji Cozunurlugu.* Suleyman Demirel Universitesi Fen Edebiyat Fakultesi Fen Dergisi **15** (2020): 237-243.

- M. Polettini, S. Jazrawi, M. M. R. Chishti, A. Yaneva, B. Das, E. Şahin, *et al*. *DESPEC Phase-0 campaign at GSI.* Il Nuovo Cimento C **44 C** 67 (2021)

- B. Das, B. Cederwall, Chong Qi, M. Górska, P. H. Regan, Ö. Aktas, H. M. Albers, E. Şahin, *et al*. *Nature of seniority symmetry breaking in the semimagic nucleus Ru 94.* Physical Review C **105.3** (2022): L031304.

- A. K. Mistry, H. M. Albers, T. Arici, A. Banerjee, G. Benzoni, B. Cederwall, J. Gerl, E. Şahin, *et al*. *The DESPEC setup for GSI and FAIR.* Nuclear Instruments and Methods in Physics Research Section A: Accelerators, Spectrometers, Detectors and Associated Equipment **1033** (2022): 166662.

- S. Jazrawi,A. Yaneva, M. Polettini, B. Das, P. H. Regan, M. Górska, B. Cederwal, E. Şahin, *et al*. *Commissioning the FAst TIMing array (FATIMA) at FAIR Phase-0: Half-lives of excited states in the N= 50 isotones* ^{96}*Pd and* ^{94}*Ru.* Radiation Physics and Chemistry **200** (2022): 110234.

- A. Yaneva, S. Jazrawi, B. Das, M. Mikolajczuk, M. M. Górska, P.H. Regan, E. Şahin, *et al*. *Fast-timing Measurement in* ^{96}*Pd: Improved Accuracy for the Lifetime of the* 4_1^+ *State.* Acta Physica Polonica B Proceedings Supplement **16(4)** (2023)

Erklärung zur Dissertation

Hiermit versichere ich, die vorliegende Dissertation ohne Hilfe Dritter nur mit den angegebenen Quellen und Hilfsmitteln angefertigt zu haben. Alle Stellen, die aus Quellen entnommen wurden, sind als solche kenntlich gemacht. Diese Arbeit hat in gleicher oder ähnlicher Form noch keiner Prüfungsbehörde vorgelegen.

Darmstadt, den

(Elif Şahin)